DISSERTATION

UNDERSTANDING THE ABILITY OF THE SOUTHERN OCEAN TO INFLUENCE THE SOUTHEASTERN TROPICAL PACIFIC

Submitted by

Yiyu Zheng

Department of Atmospheric Science

In partial fulfillment of the requirements

For the Degree of Doctor of Philosophy

Colorado State University

Fort Collins, Colorado

Summer 2025

Doctoral Committee:

Advisor: Maria Rugenstein

Peter Jan van Leeuwen
James W. Hurrell
Daniel McGrath

ABSTRACT

UNDERSTANDING THE ABILITY OF THE SOUTHERN OCEAN TO INFLUENCE THE SOUTHEASTERN TROPICAL PACIFIC

The tropical Pacific plays a central role in the climate system and is linked to two major challenges in climate modeling: persistent biases in simulations and large inter-model spread in projections. Emerging studies show that the Southern Ocean has a remote influence on sea surface temperatures (SST) in the southeastern tropical Pacific through a teleconnection involving cloud feedbacks, oceanic upwelling, climatological winds, and wind-evaporation-SST feedback. This teleconnection has primarily been explored using perturbation experiments imposed on climate model simulations, leaving open questions about how it manifests in observations and fully coupled model outputs.

This dissertation investigates the relationship between SSTs in the Southern Ocean (SO) and the southeastern tropical Pacific (SEP) using Coupled Model Intercomparison Project phase 6 (CMIP6) coupled model outputs. In Chapter 2, I analyze this relationship using pre-industrial control simulations and abrupt-CO_2-forced simulations from 53 CMIP6 models. I find a robust positive SO–SEP relationship both within and across models, regardless of whether the climate system is forced by external CO_2 or not. The inter-model spread of the positive SO-SEP relationship is attributed to the strength of shortwave cloud feedback and ocean heat uptake off the west coast of South America.

In Chapter 3, I analyze 30-year SST trends over the historical period (1985–2014) using 42 CMIP6 models and multiple observational products. Most models simulate delayed warming trends in both the SO and SEP, failing to capture the observed cooling. These warming trends are positively related across models, even after removing the global-mean trend. Models underestimate both shortwave cloud feedback and ocean heat uptake variability off the west coast of

South America, leading to opposing constraint effects: if I strengthen cloud feedback in climate models, it would enhance the SO–SEP relationship; if I strengthen ocean heat uptake variability, it would weaken the SO–SEP relationship. Furthermore, the strength of the SO–SEP relationship is positively associated with equilibrium climate sensitivity, linking this teleconnection to the higher climate sensitivity in CMIP6 models—the "hot model" problem.

In Chapter 4, I assess the SO–SEP relationship on interannual timescales using 26 CMIP6 models and observations. Both models and observations show robust positive correlations, even after removing the effects of El Niño-Southern Oscillation (ENSO)-related variability, tropical decadal variability, and the forced response. The constraining effects of shortwave cloud feedback and ocean heat uptake variability remain consistent with the previous chapter. The observed SO–SEP correlation shows that the SO-SEP relationship is underestimated in models, pointing to a dominant role of cloud feedback over ocean heat uptake variability in affecting the strength of such a relationship.

Together, these findings demonstrate that the SO–SEP relationship is an intrinsic and robust feature of the climate system. They underscore the importance of accurately simulating both shortwave cloud feedback and ocean heat uptake variability to improve this relationship in climate models, with implications for reducing the SST trend biases in climate simulations and for a warmer climate in projections.

ACKNOWLEDGEMENTS

This journey feels like a dream. I entered in a summer, and awaken in this spring.

Revisiting the journey of doing a PhD, I am filled with gratefulness for the knowledge I've gained, the progress I've made, and the range of experiences that have shaped this journey. None of this would have been possible without the support, encouragement, inspiration, and love from the incredible people I've met along the way.

First and foremost, I give my deepest thanks to my advisor, Maria Rugenstein. I would not have started this PhD journey, and I certainly wouldn't have made it through without her. From our very first conversation in Hamburg, I knew that working with Maria would be the best thing in my research life; her creativity and insight have consistently inspired me. Over the past four years, she has not only sharpened my scientific thinking but has also played a caring and thoughtful role in my life beyond research. Thank you Maria!

Then to the Rugenstein group—Marc, Olivia, Killian, Leif, Aspen, Senne, Ben, Tristan, and Eva—thank you for the discussions, the laughter, the group retreats, and all the times we spent together. I will truly miss our meetings, celebrations, and the group vibe we built together.

I am also grateful to the Department of Atmospheric Science at CSU, which has provided a supportive and encouraging environment. Special thanks to Sarah, Nate, and Dinara for their invaluable help. I am deeply thankful to my committee members—Peter Jan van Leeuwen, Jim Hurrell, and Daniel McGrath—for their time, guidance, and thoughtful feedbacks that helped shape both my research and my thinking. Choosing CSU has been one of the best decisions I've made.

Finally, heartfelt thanks to my parents, whose support from across the Pacific has sustained me throughout this journey. My cat, Ekman, has been the sweetest companion every step of the way. To my friends in the U.S.—Yao, Hanxiao, Bingying, and Hermione—thank you for all the wonderful times we shared in the cities and the mountains. And to Siyue and Wei, our friendship has lasted more than ten years, and I look forward to many more years together.

DEDICATION

To my parents who gave me life.

To friends who shaped my soul.

To the experienced and the unexperienced.

To the ocean, the Sun, the snow.

TABLE OF CONTENTS

LIST OF TABLES

LIST OF FIGURES

CHAPTER 1 INTRODUCTION

If I drop an air parcel from a cliff one kilometer above the Earth's surface, how long will it take to reach the ground? I can solve this problem by constructing a model using kinematic equations, assuming that gravity is the only force acting on the parcel and that its properties do not change during the fall. Under these conditions, the answer is approximately 14 seconds. This is a simple example of building a model to simulate the motion of an object and determine a specific outcome. What if the problem is complicated by an upward wind from below exerting a constant force on the air parcel? Then I would need to include additional equations—specifically, Newton's second law and the equation for density. My model would also require new assumptions, e.g., no forces other than gravity and wind affect the air parcel and the parcel's temperature and pressure remain constant to maintain its density. What about further extending this problem to different heights in the atmosphere, considering a much larger air parcel in the Earth's large-scale circulation system, and accounting for changes in temperature and pressure as the air moves? Can I still determine the time it takes for the air to travel a certain distance? Or, can I determine how the motion and characteristics of the air change over a specific period? Questions like these have motivated the development of climate models of various complexities over the decades.

The first true climate model was constructed in 1969 by Manabe and Bryan, featuring a three-dimensional coupled ocean and atmosphere model with idealized topography (Manabe and Bryan, 1969). This pioneering model considered ocean-atmosphere interactions, one of the fundamental ingredients of the climate system, thereby marking a milestone in the development of climate models. Six years later, Manabe and Wetherald (1975) reported the first simulation of global warming with a three-dimensional climate model that showed responses of the climate system to a doubling of the CO_2 concentration. They provided predictions—including a warmer troposphere, a cooler stratosphere, polar amplification, and higher specific humidity—that have now been observed in the real world. These early models were built upon decades of theoretical basis and modeling efforts, using dynamical cores to solve physical equations and adopting parameterizations for un-

resolved processes. They have inspired subsequent advances in climate modeling, leading to inclusions of land, ice, and biogeochemical processes and the improvement of each component over time (Randall et al., 2019).

Applications of climate models typically aim to achieve two main goals: (1) simulating the climate system as closely as possible to observations, and (2) predicting future climate as reliably as possible. These two goals are not independent, according to the emergent constraint theory (Hall et al., 2019). The first goal is often addressed by perturbing climate models to identify their current limitations. For example, Kay et al. (2016) modified the shallow convection detrainment in an atmosphere-only model to match observed values, significantly reducing long-standing shortwave radiation biases over the Southern Ocean. The second goal generally involves conducting statistical analyses on climate model outputs under different forcing scenarios to assess uncertainties and interpret the range of projections. For example, Ceppi and Nowack (2021) demonstrated the key role of cloud feedbacks in explaining the intermodel spread in equilibrium climate sensitivity (ECS). They used observations and climate model simulations—including historical runs and future emission scenarios from phases 5 and 6 of the Coupled Model Intercomparison Project (CMIP)—and highlighted implications of cloud feedbacks for a likely warmer future climate.

Despite decades of development, climate models still have serious problems, raising concerns about the fidelity of their simulations and projections. On the one hand, climate models continue to suffer from large biases in their simulations, such as the double-Intertropical Convergence Zone (ITCZ) bias (e.g., Tian and Dong, 2020). This bias manifests itself as erroneously excessive precipitation in the Southern Hemisphere tropics and has recently been linked to sea surface temperature (SST) biases over the Southern Ocean (e.g., Hwang and Frierson, 2013; Kay et al., 2016; Kang et al., 2018a).

The connection between the biases over the Southern Ocean and the tropics was first shown in Hwang and Frierson (2013) using CMIP5 historical simulations, offering a new extratropical perspective on explaining the tropical biases. Successive studies have conducted perturbation experiments across models of various complexities to test the connection between the Southern Ocean

climate and the double-ITCZ bias. Robust improvements in the double-ITCZ bias are shown in models of different complexities after perturbing the Southern Ocean climate by reducing shortwave radiation influx (Mechoso et al., 2016), reducing cloud biases (Kay et al., 2016), increasing ocean heat uptake (Hwang et al., 2017), increasing albedo (Hawcroft et al., 2017; Haywood et al., 2016; Green and Marshall, 2017), applying thermal forcings (Kang et al., 2018b), and perturbing heat flux divergence (Liu et al., 2020).

On the other hand, in addition to the large biases in climate simulations, climate models have large model spreads in their projections, such as the uncertainty in ECS, which has recently been narrowed to a *likely* range of 2.5°C–4.0°C (Forster et al., 2023). ECS quantifies the degrees of equilibrium global warming in response to a doubling of atmospheric CO_2. Part of its uncertainty is linked to the spatial pattern of SST change under global warming—known as the pattern effect (e.g., Stevens et al., 2016).

The pattern effect describes how changes in the SST pattern affect the global radiative feedback of the climate system. It helps explain the increased (less-negative) global radiative feedback simulated in idealized warming scenarios driven by increased CO_2, which can lead to a higher ECS (e.g., Armour et al., 2013; Andrews et al., 2015; Ceppi and Gregory, 2017). In CMIP6 models, the increased global radiative feedback primarily originates in the eastern tropical Pacific (Dong et al., 2020). As the eastern tropical Pacific warms and becomes warmer than the western tropical Pacific, the tropical Pacific is expected to exhibit an "El Niño-like" warming pattern. This warming pattern is accompanied by a positive cloud feedback in the eastern tropical Pacific, leading to reduced shortwave reflectance due to reduced low clouds and resulting in a larger ECS as the climate system equilibrates (e.g., Ceppi and Gregory, 2017; Andrews and Webb, 2018). The intermodel spread of the pattern effect in CMIP6 models can be attributed to SST changes in the eastern tropical Pacific, suggesting an important role of this region in explaining the model spread of ECS (Dong et al., 2020).

The eastern tropical Pacific SST can be affected by the Southern Ocean, as expected given the relationship between the Southern Ocean climate and tropical precipitation discussed above.

In both slab-ocean and fully coupled climate models, perturbing the Southern Ocean to cool or warm results in robust decreases or increases in eastern tropical Pacific SST, respectively. (e.g., Mechoso et al., 2016; Hwang et al., 2017; Kang et al., 2018b; Xiang et al., 2018; Lin et al., 2021). In fully coupled models, Southern Ocean perturbations drive corresponding SST changes in the eastern tropical Pacific through multiple mechanisms, including stratocumulus cloud feedbacks, climatological winds, and oceanic upwelling along the west coast of South America, and the wind-evaporation-SST (WES) feedback in the subtropical Pacific (Kim et al., 2022; Mechoso et al., 2016; Kang et al., 2020; Zhang et al., 2021). This teleconnection between the Southern Ocean and the eastern tropical Pacific elevates the importance of the Southern Ocean in climate projections, implying a higher ECS as Southern Ocean warming accelerates with continued climate change (Kang et al., 2023a).

In this dissertation, I investigate the relationship between the Southern Ocean and the southeastern tropical Pacific using CMIP6 climate model outputs. Using coupled model outputs instead of applying perturbations on the simulated climate system avoids additional changes to the simulated climate. For example, Deser et al. (2020) isolated the effect of aerosol forcing, showing a negative SST trend in both global-mean temperature and the eastern tropical Pacific after the 1950s. This raises the question of whether the cooling signals over the eastern tropical Pacific in Southern Ocean perturbation experiments originate from the Southern Ocean or result from the overall cooling of the global climate system. While existing literature mostly focuses on the eastern tropical Pacific, this dissertation focuses on the southeastern tropical Pacific, specifically because that is where delayed warming appears in coupled model simulations, aligning with the delayed warming in the Southern Ocean (will be discussed in Chapters 2 and 3). Using either region in the analysis generally does not affect my conclusions.

In Chapter 2, I analyze the relationship between the Southern Ocean and the southeastern tropical Pacific SST measured by interannual correlations using pre-industrial control simulations and forced simulations with an abrupt quadrupling of CO_2 from CMIP6. I also investigate the effect of four physical processes—stratocumulus cloud feedbacks, total wind speed, ocean heat uptake

along the west coast of South America, and the WES feedback in the subtropical Pacific—on this relationship in coupled model outputs. My results align with previous studies in highlighting the key role of stratocumulus cloud feedbacks in controlling the strength of this relationship, while also revealing an important role for ocean heat uptake.

In Chapter 3, I shift focus to the cross-model relationship between 30-year SST trends in the Southern Ocean and the southeastern tropical Pacific using transient historical simulations from CMIP6. Compared to Chapter 2, which focuses on interannual variability in idealized experiments, this chapter examines the relationship between the Southern Ocean and the southeastern tropical Pacific using multi-decadal trends in a more realistic historical climate context. The influence of stratocumulus cloud feedback and ocean heat uptake is again assessed, revealing opposing constraints on this relationship: if I strengthen the cloud feedback in models to match observations, the Southern Ocean-southeastern tropical Pacific relationship would be strengthened; if I strengthen the ocean heat uptake variability in models, the relationship would be weakened.

In Chapter 4, I return to interannual correlations as in Chapter 2, but using the transient historical simulations as in Chapter 3, which allows a direct comparison between the simulated and the observed Southern Ocean–southeastern tropical Pacific relationship. The constraining effects of stratocumulus cloud feedback and ocean heat uptake remain consistent with those identified in Chapter 3. Including observed Southern Ocean–southeastern tropical Pacific correlations reveals the dominant role of the cloud feedback relative to the ocean heat uptake, though the latter is non-negligible. Improving the Southern Ocean-southeastern tropical Pacific relationship solely by enhancing the cloud feedback may lead to an overestimation of the relationship. Therefore, both the cloud feedback and the ocean heat uptake should be jointly considered when improving the Southern Ocean-southeastern tropical Pacific relationship in climate models.

CHAPTER 2 THE RELATIONSHIP BETWEEN THE SOUTHERN OCEAN AND THE SOUTHEASTERN SUBTROPICAL PACIFIC IN UNFORCED AND FORCED CLIMATE MODEL SIMULATIONS [1]

2.1 Introduction

The observed sea surface temperatures (SSTs) over the Southern Ocean and the eastern tropical Pacific have exhibited cooling trends since the 1970s, while climate models have struggled to reproduce such trends (e.g., Watanabe et al., 2024; Kostov et al., 2014; Rugenstein et al., 2023). In the eastern tropical Pacific, climate models have simulated a warming trend, which could be caused by incorrect internal variability, teleconnections, or responses to anthropogenic forcing (e.g., Watanabe et al., 2021a; Olonscheck et al., 2020; Seager et al., 2022; Wills et al., 2022). For example, the erroneously simulated SST trends could be related to model misrepresentation of the Pacific trade winds, the interbasin warming pattern, the cold tongue SST, or the equatorial cloud feedback (e.g., England et al., 2014; Kajtar et al., 2018; Zhang et al., 2019b; Seager et al., 2019; Luo et al., 2018). Similarly, climate models have simulated a warming trend in the Southern Ocean. The discrepancy between the modeled and observed SST trends in the Southern Ocean could be related to incorrect simulations of internal variability, biases in Antarctic meltwater, the Southern Annular Mode, and cloud-related shortwave radiation, or misrepresentations of modeled responses to ozone depletion and greenhouse gas forcing (e.g., Zhang et al., 2019a; Rye et al., 2020; Purich et al., 2016; Kostov et al., 2018; Hartmann, 2022; Yeager et al., 2023).

The warm bias over the Southern Ocean might be related to the tropical Pacific. Hwang and Frierson (2013) linked the Southern Ocean to the tropics in Coupled Model Intercomparison Project Phase 5 (CMIP5) models by demonstrating an inter-model relationship between stratocumulus cloud radiative forcing biases over the Southern Ocean and the double-Intertropical Convergence Zone biases. Successively, studies have analyzed models of various complexity to

[1] Zheng, Y., Rugenstein, M., and Alessi, M. J. The Relationship between the Southern Ocean and the Southeastern Subtropical Pacific in Unforced and Forced Climate Model Simulations. *Accepted by Journal of Climate*.

test how thermal changes in the Southern Ocean SST drive changes in the eastern tropical Pacific SST.

Imposed cooling on the Southern Ocean reduces the SST over the eastern tropical Pacific. In atmospheric models coupled with a slab ocean, a Southern Ocean cooling induced by various perturbations results in decreased SST over the eastern tropical Pacific (e.g., Hwang et al., 2017; Kang et al., 2018a,b). In addition, Dong et al. (2022) revealed a feedback loop between the two regions by applying a heat flux divergence from the Southern Ocean mixed layer in a slab-ocean model: the Southern Ocean cooling propagates equatorward by climatological wind advection which cools the eastern tropical Pacific, triggering a Rossby wave teleconnection that enhances the Southern Hemisphere subtropical high and trade winds and further amplifies the Southern Ocean cooling. Similarly, in fully coupled climate models, the emerged cooling over the eastern tropical Pacific has been attributed to perturbed Southern Ocean cooling through multiple mechanisms, including stratocumulus-SST feedbacks in the southern subtropics, climatological wind pattern and oceanic upwelling along the west coast of South America, and the wind-evaporation-SST (WES) feedback in the tropics (Kim et al., 2022; Mechoso et al., 2016; Kang et al., 2020; Zhang et al., 2021; Kang et al., 2023a). However, ocean dynamics might dampen some of the tropical response to a Southern Ocean perturbation (Kay et al., 2016; Hawcroft et al., 2017; Green and Marshall, 2017; Kang et al., 2018b). In short, studies show that the Southern Ocean *cooling* robustly triggers an SST response over the eastern tropical Pacific in models with or without a dynamical ocean, though the SST response in slab-ocean models is stronger than that in fully coupled models (e.g., Kang et al., 2020).

Imposed *warming* in the Southern Ocean increases the SST over the eastern tropical Pacific. This teleconnection is tangentially shown in several studies without being explicitly explained. For example, in a slab-ocean model, SSTs in the eastern tropical Pacific increased following an imposed weakening of the ocean heat uptake in the Southern Ocean (Fig. 3 in Lin et al., 2021). In fully coupled climate models, similarly, the eastern tropical Pacific warms in response to increased shortwave radiation over the Southern Ocean (Fig. 13a in Yu and Pritchard, 2019; Fig. 5a in

Xiang et al., 2018). Whether Southern Ocean warming affects the eastern tropical Pacific via the same pathway and efficiency as Southern Ocean cooling (as discussed in the previous paragraph) is unknown.

Given the robust relationship between the SSTs over the Southern Ocean and the eastern tropical Pacific in climate models, I hypothesize that: (1) This relationship holds in a pre-industrial climate without external forcing (hereinafter referred to as unforced climate), when both regions warm or cool; (2) This relationship holds in an externally forced climate by CO_2 increase, when both regions show *delayed warming*.

In my first hypothesis, I propose that the relationship between the Southern Ocean and the eastern tropical Pacific SSTs holds in a climate without external forcing when both regions warm or cool. I base this hypothesis on the presence of climatological wind advection that transports signals from the Southern Ocean equatorward and potentially induces a connection between these two regions, regardless of imposed warming or cooling on the Southern Ocean (e.g., Yu and Pritchard, 2019; Kim et al., 2022; Dong et al., 2022). This hypothesis is supported by a strong correlation between SST trends over the eastern tropical Pacific and the Southern Ocean using the Last Millennium Reanalysis dataset (Dong et al., 2022), suggesting a relationship between the two regions in a climate without external forcing.

In my second hypothesis, I argue that the delayed warming in the Southern Ocean and the eastern tropical Pacific, simulated in coupled climate models under increased CO_2, are linked. Unlike the observed cooling trends and the projected warming trends (e.g., Rugenstein et al., 2023; Cai et al., 2023), the delayed warming pattern over the eastern tropical Pacific and the Southern Ocean arises in response to an idealized, instantaneous forcing, e.g., an abrupt doubling or quadrupling of CO_2 at the start of simulations (e.g., Clement et al., 1996; Held et al., 2010; Heede and Fedorov, 2021). Under such abrupt external forcing, the climate system responds with widespread warming, while the eastern tropical Pacific and the Southern Ocean warm less than other regions, which I refer to as *delayed* warming (e.g., Senior and Mitchell, 2000; Armour et al., 2013). I would like to emphasize that the delayed warming used here does not refer to a temporal difference of warming

between an early and late period (e.g., Andrews et al., 2015). Rather, I use this term to describe the spatial pattern of warming differences, i.e., the Southern Ocean and the eastern tropical Pacific warm less than other regions (e.g., Bloch-Johnson et al., 2024; Armour et al., 2016). This delayed warming pattern over the Southern Ocean and the eastern tropical Pacific is due to climatological ocean circulation that induces circumpolar upwelling and transports surface water equatorward and the equatorial upwelling of cold waters, respectively (e.g., Armour et al., 2016; Clement et al., 1996; Held et al., 2010; Heede et al., 2020, 2021; Heede and Fedorov, 2021). Importantly, the SST pattern over the eastern tropical Pacific can influence global radiative feedbacks and global-mean temperature (e.g., Andrews and Webb, 2018; Dong et al., 2019; Alessi and Rugenstein, 2023). The exact pace and magnitude of the eastern tropical Pacific warming are also relevant for global-mean warming trends and regional climate trends such as in central American and Southwest U.S. precipitation (e.g., Kosaka and Xie, 2016; Seager et al., 2019; Deser et al., 2017; Alessi and Rugenstein, 2023; Dettinger et al., 1998).

I test the two hypotheses across models from the CMIP6 multi-model archive, i.e., no perturbations are applied to the Southern Ocean. I introduce the analyzed models and variables in Section 2.2. While I use lag-0 correlations and regressions to represent the relationships between the Southern Ocean and the eastern tropical Pacific, my main focus is on the teleconnections from the Southern Ocean to the tropics. In Section 2.3, I walk through the two hypotheses and test this directional relationship by removing dominant tropical variabilities. After analyzing the relationship between the Southern Ocean and eastern tropical Pacific SSTs, I investigate the impacts of stratocumulus cloud feedback, oceanic upwelling, WES feedback, and total wind speed on such a relationship in Section 2.4, following the Southern Ocean teleconnection pathway proposed in Kim et al. (2022). In Section 2.5, I discuss the implications of my findings and summarize the results.

2.2 Model Output

I analyze model output from unforced pre-industrial control simulations (piControl) and forced simulations with an abrupt quadrupling of CO_2 (abrupt-4xCO2) across 53 CMIP6 models (sum-

marized in Table 1). I use the abrupt-4xCO2 simulation because it has a better signal-to-noise ratio than a doubling of CO_2, and it shows only the SST response to CO_2 and not other forcing agents like aerosols (e.g., Heede and Fedorov, 2021; Hwang et al., 2024). I use annual data to remove the seasonal cycle. The selected models have varying spatial resolutions, so I re-grid all model output from their original spatial resolutions to 2.5° x 2.5° resolution. While all abrupt-4xCO2 simulations span 150 years, the length of piControl simulations differs among models, and I focus on the last 150 years of piControl simulations for models with longer lengths. My results are not sensitive to different 150-year periods selected from piControl simulations.

I analyze SST (*tos*; available in all selected models) in Section 3 to analyze the warming over the Southern Ocean and the eastern tropical Pacific and their relationship. Following the methodology of Kim et al. (2022), I calculate the stratocumulus cloud feedback from SST and the shortwave cloud radiative effect (calculated by *rsut-rsutcs*; available in 48 of the selected models). I use the net surface heat flux (calculated by *rlds-rlus+rsds-rsus-hfss-hfls*; available in 49 of the selected models) to quantify ocean heat uptake along the west coast of South America. I analyze the WES feedback based on SST, near-surface zonal wind, surface latent heat flux (*hfls*), and sea-level pressure (*psl*); WES feedback can be quantified for 35 of the selected models. I analyze wind by using near-surface total wind speed (*uas, vas*; available in 37 of the selected models). Detailed definitions and calculations of the analyzed physical processes are provided in Section 4.

I analyze the effect of the Southern Ocean teleconnection on the eastern tropical Pacific within a triangle in the southeastern subtropical Pacific region (SEP; 47°S-10°S, 180°E-71°W; shown as the black triangle in Fig. 2.1a). This SEP region is selected based on the emergence of delayed warming (see Section 3c), which differs from the eastern tropical Pacific regions examined in previous studies (e.g., Kim et al., 2022; Dong et al., 2022). Extending the SEP triangle northward to the equator does not qualitatively affect my results. The degree to which models allow the SST signals from the Southern Ocean to penetrate to the equatorial region is strongly model-dependent and not well understood yet. For the Southern Ocean, I focus on a sector in the South Pacific (SO; 60°S-45°S, 160°E-70°W; shown as the white box in Fig. 2.1a) due to its strongest relation with

tropical SSTs. Expanding the SO box across the longitudinal band reveals a weaker yet similar relationship between the SO and the SEP, consistent with the findings in Dong et al. (2022) that the Pacific sector of the Southern Ocean has the strongest relationship with the tropical Pacific.

Table 2.1: CMIP6 models used in this study.

Institution	Model	Reference	Institution	Model	Reference
CSIRO-ARCCSS	ACCESS-CM2	Dix et al. (2019)	NOAA-GFDL	GFDL-CM4	Guo et al. (2018)
CSIRO	ACCESS-ESM1-5	Ziehn et al. (2019)	NOAA-GFDL	GFDL-ESM4	Krasting et al. (2018)
AWI	AWI-CM-1-1-MR	Semmler et al. (2018)	NASA-GISS	GISS-E2-1-G	NASA/GISS (2018a)
BCC	BCC-CSM2-MR	Xin et al. (2018)	NASA-GISS	GISS-E2-1-H	NASA/GISS (2018b)
BCC	BCC-ESM1	Zhang et al. (2018)	NASA-GISS	GISS-E2-2-G	NASA/GISS (2019a)
CAMS	CAMS-CSM1-0	Rong (2019)	NASA-GISS	GISS-E2-2-H	NASA/GISS (2019b)
NCAR	CESM2-FV2	Danabasoglu (2019a)	MOHC	HadGEM3-GC31-LL	Ridley et al. (2018)
NCAR	CESM2-WACCM-FV2	Danabasoglu (2019c)	MOHC	HadGEM3-GC31-MM	Ridley et al. (2019)
NCAR	CESM2-WACCM	Danabasoglu (2019d)	MPI-M	ICON-ESM-LR	Lorenz et al. (2021)
NCAR	CESM2	Danabasoglu (2019b)	INM	INM-CM4-8	Volodin et al. (2019a)
THU	CIESM	Huang (2019)	INM	INM-CM5-0	Volodin et al. (2019b)
CMCC	CMCC-CM2-SR5	Lovato and Peano (2020)	IPSL	IPSL-CM6A-LR	Boucher et al. (2018)
CMCC	CMCC-ESM2	Lovato et al. (2021)	KIOST	KIOST-ESM	Kim et al. (2019)
CNRM-CERFACS	CNRM-CM6-1	Voldoire (2018)	UA	MCM-UA-1-0	Stouffer (2019)
CNRM-CERFACS	CNRM-ESM2-1	Seferian (2018)	MIROC	MIROC-ES2L	Hajima et al. (2019a)
CCCma	CanESM5-1	Swart et al. (2019b)	MIROC	MIROC6	Tatebe and Watanabe (2018)
CCCma	CanESM5	Swart et al. (2019a)	HAMMOZ-Consortium	MPI-ESM-1-2-HAM	Neubauer et al. (2019)
E3SM-Project	E3SM-1-0	Bader et al. (2019)	MPI-M	MPI-ESM1-2-HR	Jungclaus et al. (2019)
E3SM-Project	E3SM-2-0-NARRM	Bader et al. (2023)	MPI-M	MPI-ESM1-2-LR	Wieners et al. (2019)
E3SM-Project	E3SM-2-0	Bader et al. (2022)	MRI	MRI-ESM2-0	Yukimoto et al. (2019)
EC-Earth-Consortium	EC-Earth3-AerChem	EC-Earth (2020b)	NUIST	NESM3	Cao and Wang (2019)
EC-Earth-Consortium	EC-Earth3-CC	EC-Earth (2020a)	NCC	NorESM2-LM	Seland et al. (2019)
EC-Earth-Consortium	EC-Earth3-Veg-LR	EC-Earth (2020c)	NCC	NorESM2-MM	Bentsen et al. (2019)
EC-Earth-Consortium	EC-Earth3-Veg	EC-Earth (2019b)	SNU	SAM0-UNICON	Park and Shin (2019)
EC-Earth-Consortium	EC-Earth3	EC-Earth (2019a)	MOHC	UKESM1-0-LL	Tang et al. (2019)
CAS	FGOALS-f3-L	YU (2018)	MOHC	UKESM1-1-LL	Mulcahy et al. (2022)
FIO-QLNM	FIO-ESM-2-0	Song et al. (2019)			

I assess the relationship between the SO and the SEP in the: (1) unforced climate using piControl simulations; (2) forced climate with a strong CO_2 increase (abrupt-4xCO2 forcing); and (3) *pattern* of the forced response relative to the global-mean warming. The relationship between the

two regions is assessed in two ways. First, I measure the relationship within each model across time, which measures the covariation of the interannual variability of the SO and SEP SSTs over an analyzed period. Second, I measure the relationship across models averaged over an analyzed period, which quantifies the inter-model relationship between the long-term mean SO and SEP SSTs.

2.3 The Relationship Between the Southern Ocean and the Southeastern Subtropical Pacific

2.3.1 In an Unforced Climate

Within each model, the unforced SST over the SO and the SEP are positively correlated. Without external forcing, the SEP shows relatively cooler SSTs than the surrounding areas (Fig. 2.1a), which might be attributed to the land distribution (Philander et al., 1996; Takahashi and Battisti, 2007) and a combined effect of subtropical cloud feedback and the WES feedback. Disentangling the cause and effect of the highly coupled mechanisms—comprising wind, SST, subtropical cloud feedback, and evaporation—remains challenging and warrants further investigation. Correlating all grid points in the South Pacific to the SST averaged over the SEP triangle (Fig. 2.1b) and over the SO box (Fig. 2.1c) exhibits a clear horseshoe pattern of statistically significant correlations connecting the two regions, consistent with the correlation map shown in Dong et al. (2022). This correlation measures the instantaneous relationship between the SO and the SEP SSTs, and I recognize the effects of El Niño-Southern Oscillation (ENSO) teleconnections that could induce a positive correlation from the tropics to the SO (as reviewed in Li et al., 2021). I tested the effect of ENSO by regressing out the SSTs averaged over the Niño 3.4 region, which reduced the model-mean SO-SEP correlation by 25% (not shown). Hence, the relationship between the SO and the SEP (Fig. 2.1c) is affected by ENSO but not predominantly. Furthermore, I applied a 10-year high-pass filter to remove the effect of decadal variability in the tropical Pacific on the SO (e.g., Schneider and Deser, 2018), which showed no significant change in the model-mean SO-SEP correlation (not shown).

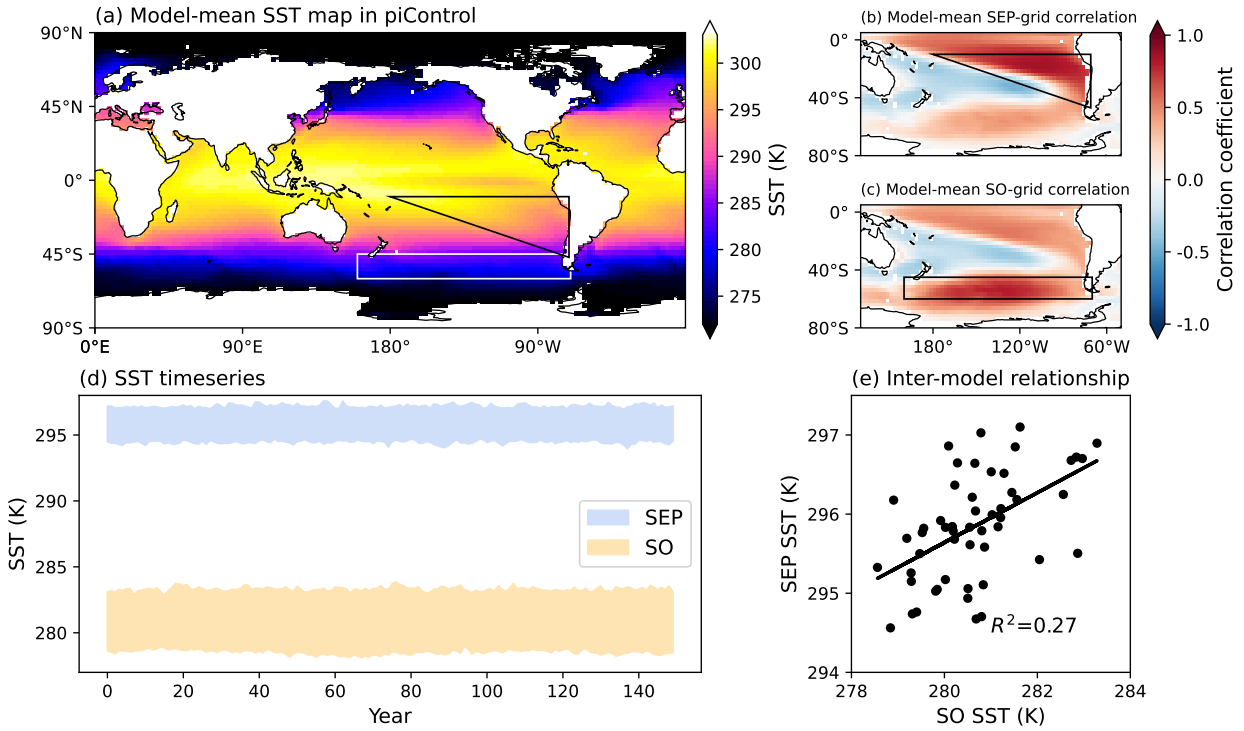

Figure 2.1: Overview of the unforced SSTs and the SO-SEP relationship in piControl. (a) Multi-model-mean SST map averaged over 150 years. The black and white boxes represent the SEP and SO regions, respectively. (b) Multi-model-mean correlations between unforced SSTs at each grid point and the area-weighted average of the SEP SST. A similar correlation map between each grid point and the SO SST is shown in (c). The correlations are calculated within each model's 150-year annual timeseries. (d) Model spread of the SEP and SO SST timeseries. (e) Relationship between SO and SEP SSTs across models. Each circle represents an individual model averaged over the 150 years shown in (d).

Across models, the unforced SSTs over the SO and the SEP are also positively related. The SO SST shows a larger model spread than the SEP SST (Fig. 2.1d), attributing to biases in ocean stratification, cloud cover, sea ice, and westerly wind, along with other unresolved complex physical processes within the SO (e.g., Meijers, 2014; Kajtar et al., 2021; Cai et al., 2023). Models with a warmer SO SST tend to have a warmer SEP SST, with the SO SST spread explaining 27% of the SEP SST spread (Fig. 2.1e). Despite a relatively low R^2 value, the regression slope is significantly different from zero according to a t-test ($p<0.05$), and the linear fit of the regression model is also significant according to an F-test ($p<0.05$), suggesting that the mean-state biases of SSTs in the two regions are robustly related. In summary, the SO and SEP SSTs in the unforced climate

are positively related both in single models across time (by internal variability) and across models averaged over time (by mean-state biases), supporting my first hypothesis.

2.3.2 In a Forced Climate to abrupt-4xCO2 Forcing

Under the abrupt-4xCO2 forcing, the SO and SEP warm less than surrounding areas. SST anomalies are calculated for each grid point by subtracting the linear regression fit of the time-series of piControl simulations from abrupt-4xCO2 simulations. In the first 50 years following a quadrupling of CO_2, both the SO and SEP show a model-mean SST warming approximately 1K less than that of the surrounding areas (Fig. 2.2a). This delayed warming over the SO and SEP forms a horseshoe pattern of SST anomalies (Fig. 2.2a). Changing the length of the 50-year period to 20-, 40- or 60-year does not affect the spatial distribution of SST anomalies and the results of the following analyses.

Within each model, correlations between SO and SEP SST anomalies are larger than those in piControl simulations, indicating that the relationship between the two regions is stronger due to radiative forcing. I calculate correlations between SO and SEP SST anomalies for a sliding window of 50 years (the silver lines in Fig. 2.2b), and I compare them to the ones calculated in piControl simulations over the entire 150 years (the red bar in Fig. 2.2b). The correlations between SO and SEP SST anomalies show temporal variations that peak in the first 50 years, implying a dominant role of forced trends. As the climate system moves towards equilibrium, the 50-year running correlations decrease until the model-mean correlation coefficient (the end value of the black line in Fig. 2.2b) approaches the piControl value (the red dot in Fig. 2.2b). Regressing out ENSO variability reduced the model-mean correlation by 13%, while the SO and SEP remained strongly correlated at 0.77 (not shown). Applying a 10-year high-pass filter not only removes tropical Pacific decadal variability but the global-mean warming trends, reducing the model-mean correlation by 25% (not shown).

Across models, the SST anomalies over the SO and the SEP are positively related. The inter-model spread of the SO SST anomaly is larger than that of the SEP, with both regions showing an increase in modeled SST spread over time until the end of the simulation (Fig. 2.2c). In the first

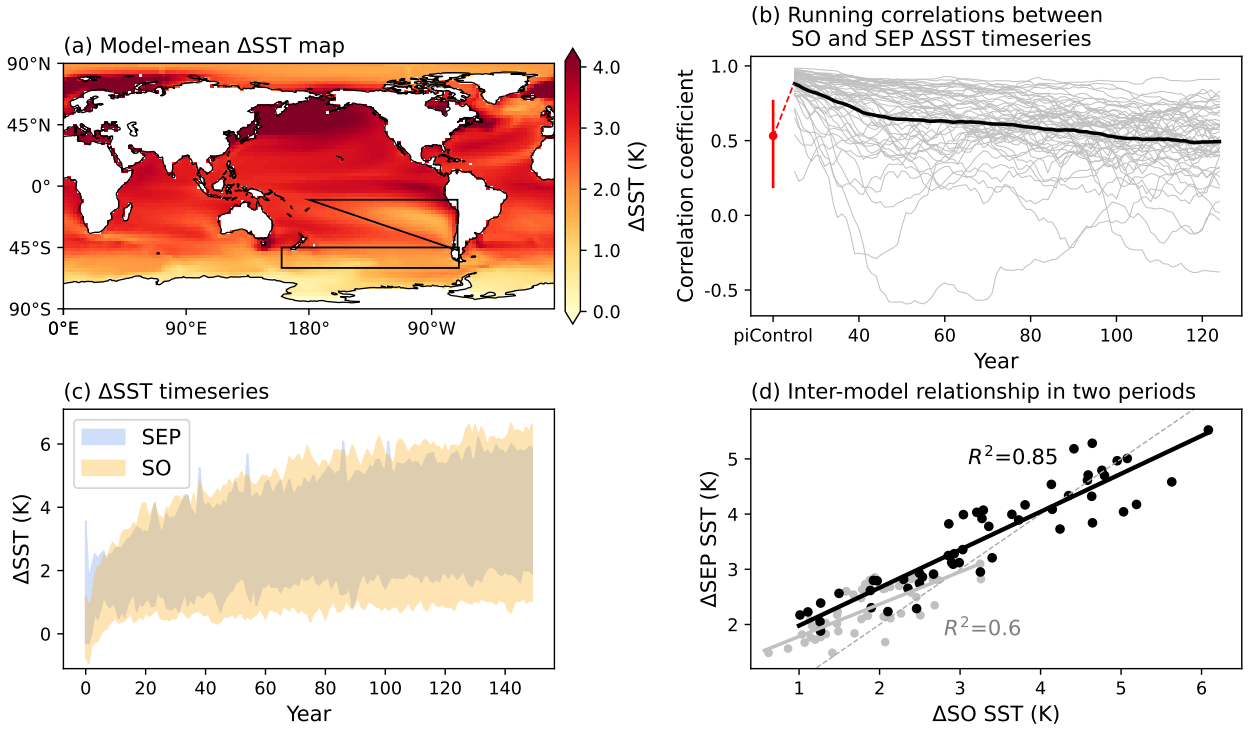

Figure 2.2: Overview of SST anomalies between piControl and abrupt-4xCO2 and the SO-SEP relationship in response to an abrupt-4xCO2 forcing. (a) Multi-model-mean SST anomalies averaged over years 1-50. (b) Temporal variations of correlations between SO and SEP SST anomalies within each model. The red circle and error bar show the model mean and spread of correlations between SO and SEP SST in piControl, similar to Fig. 2.1c. Lines show 50-year running correlations between SO and SEP SST anomalies in individual models (grey) and as the model-mean (black). (c) Model spread of the SEP and SO SST anomalies. (d) Relationships between SO and SEP SST anomalies averaged over years 1-50 (grey) and years 100-150 (black) across models. The dashed line is the 1-1 line. Each circle represents an individual model.

50 years, 87% of the models show greater warming in the SEP than in the SO (as indicated by the points above the dashed 1-1 line in Fig. 2.2d). Over time, the SEP SST warms more in models with stronger SO warming, as indicated by a slightly more positive regression slope in the last 50 years than that in the first 50 years (Fig. 2.2d). The strong positive relationships between SO and SEP SST anomalies can be explained by the global-mean temperature. Global-mean warming is used to calculate the equilibrium climate sensitivity, which quantifies the Earth system's response to increased CO_2 and has a large uncertainty range across models (e.g., Sherwood et al., 2020). A model with a higher climate sensitivity likely warms more in both regions (not shown), indicating a confounding role of the global-mean warming in connecting the SO and SEP. Therefore, in the next

section, I remove the effect of model-dependent global-mean warming and study the relationship between the *pattern* of the SO and SEP SST.

2.3.3 In the pattern of the forced response

Under external forcing, local SSTs respond with varying warming rates and magnitudes across different regions, creating a spatial pattern of SST anomalies. I isolate this SST pattern from the global-mean SST anomaly to analyze whether the SO and the SEP are related. I calculate the SST pattern in each model by dividing SST anomalies at each grid point by the global-mean SST anomaly at each timestep, implying the global-mean of the SST pattern at any given timestep equals one.

A delayed (relative to the global-mean) warming pattern emerges over the SO and the SEP (Fig. 2.3a). It is worth noting that, unlike many experiments of the *imposed* cooling or warming on the Southern Ocean that penetrates all the way into the equatorial Pacific (within 10°S-10°N; e.g., Mechoso et al., 2016; Hwang et al., 2017; Lin et al., 2021; Kim et al., 2022; Dong et al., 2022), the delayed warming pattern in all CMIP6 models stops at around 10°S. I choose the SEP region based on this multi-model-mean pattern shown in Fig. 2.3a, even if it does not lie inside of the tropical Pacific region. Extending the SEP triangle northward to the equator does not qualitatively affect my results. The reasons why such a delayed warming does not penetrate into the equator remain unknown and warrant further investigation.

The delayed warming pattern persists over time. SST pattern timeseries averaged over the SO and SEP equilibrate within 10 years (Fig. 2.3d), faster than the timeseries of SST anomalies shown in Fig. 2.2c. After reaching equilibrium, the SST pattern in the SO and SEP in most models stay below 1K/K, indicating a delayed warming over the SO and SEP relative to the global-mean temperature. This persistency of the delayed warming can also be seen in the scatter plot (Fig. 2.3e). In the first 50 years, all but two models (INM-CM4-8 and MCM-UA-1-0) show delayed warming over the SO (SST pattern in SO>1.0). In the last 50 years, more than 90% of the models still show a delayed warming over the SO and SEP. Changing the length of the 50-year period to

20-, 40- or 60-year does not affect the spatial distribution of the SST pattern and the results of the following analyses.

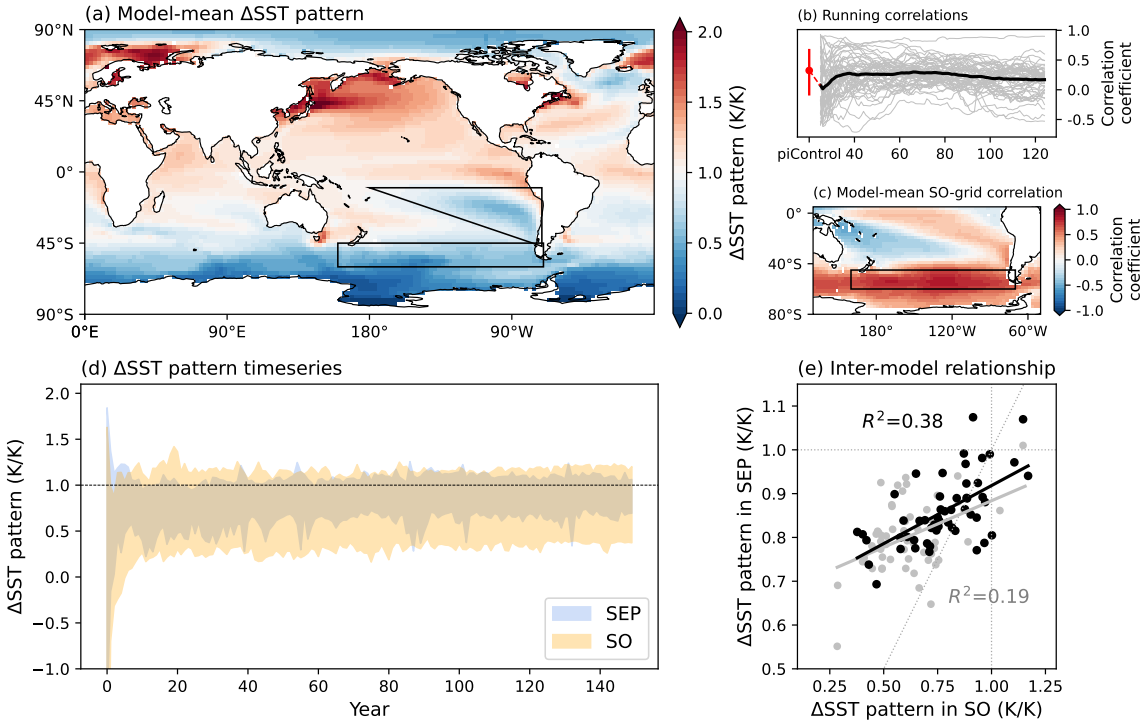

Figure 2.3: Overview of SST pattern and SO-SEP relationships. (a) Multi-model-mean SST pattern map averaged over years 1-50. (b) Temporal variations of correlations between the SO and SEP SSTs in each model, similar to Fig. 2.2b but with the global-mean temperature removed from the SSTs. The red circle and error bar show the model mean and spread of correlations between SO and SEP SSTs in piControl, from which the global-mean temperature is also removed by dividing the unforced SSTs on each point by the unforced global-mean SST. (c) Multi-model-mean correlations over the entire 150 years between the SST pattern at each grid point and the area-weighted average of the SST pattern over the SO. (d) Model spread of the SST pattern timeseries averaged over the SO and SEP. Six models show SST pattern in these two regions smaller than -1.0 at the first time step, which are cropped to zoom in on the remaining timeseries. (e) Relationships between the SO and SEP SSTs without global-mean temperature averaged over years 1-50 (grey) and years 100-150 (black) across models.

Within each model, the delayed warming in the SO and SEP are positively correlated. Unlike the correlations between the SO and SEP SST anomalies (Fig. 2.2b), the correlations in Fig. 2.3b do not peak in the first 50 years due to the removal of global-mean warming and the large model spread in the evolutions of the SST pattern in both regions in the first 10 years (Fig. 2.3d). The model discrepancies in the evolution of the SST pattern will be further discussed in Section 3c(1).

As the climate system approaches equilibrium, the running correlations increase, approaching the piControl level (Fig. 2.3b). This indicates that the correlation between the SST pattern in the SO and SEP is driven by the internal variability after global-mean warming is removed. The correlation map (Fig. 2.3c) resembles the one in the piControl simulation (Fig. 2.1c), but with weaker correlations in a more confined area. Regressing out ENSO variability reduces the model-mean SO-SEP correlation by 20%, leaving a weak correlation of 0.2. Filtering out tropical Pacific decadal variability has little effect (not shown), indicating SO and SEP are linked on a timescale of less than 10 years.

Across models, the delayed warming in the SO and the SEP are positively related. Models with stronger delayed warming in the SO—i.e. more relative cooling over the SO—also display stronger delayed warming in the SEP (Fig. 2.3d). The SST pattern timeseries in the SO exhibits a larger model spread than that over the SEP, with both regions showing a stabilized spread within the first 10 years (Fig. 2.3c). In the first 50 years, the spread of the SO SST accounts for only 19% of that in the SEP (Fig. 2.3d). This low R^2 value, similar to the low correlation in the first 50 years, is due to the large model spread in the SST in the first 10 years (Fig. 2.3a). Removing the first 10 years results in an R^2 value of 24%. As the model spreads decrease over time, the R^2 in the last 50 years increases to 38% (Fig. 2.3d). Using the entire timeseries, the relationship between the SO and SEP SST across models exhibits an R^2 value of 30% (not shown), higher than the R^2 value in Fig. 2.1e, indicating a stronger SO-SEP relationship in a forced climate than in the unforced climate even if the global-mean warming is removed. In summary, the delayed warming in the SO and SEP in the forced climate without global-mean warming signals are positively related in single models across time and across models averaged over time, supporting my second hypothesis.

Model discrepancies in SST pattern

Models differ in spatial variations and magnitude of the delayed warming pattern. I exemplify this model diversity by picking two models—CESM2 and EC-Earth-AerChem—based on their distinct correlations between the SO and SEP SST in the forced climate without global-mean warming. The model discrepancies in the SST pattern cannot be simply categorized into

two groups, and the aim of this section is to describe the model diversity in the SST pattern and encourage future research to explore these model discrepancies in depth.

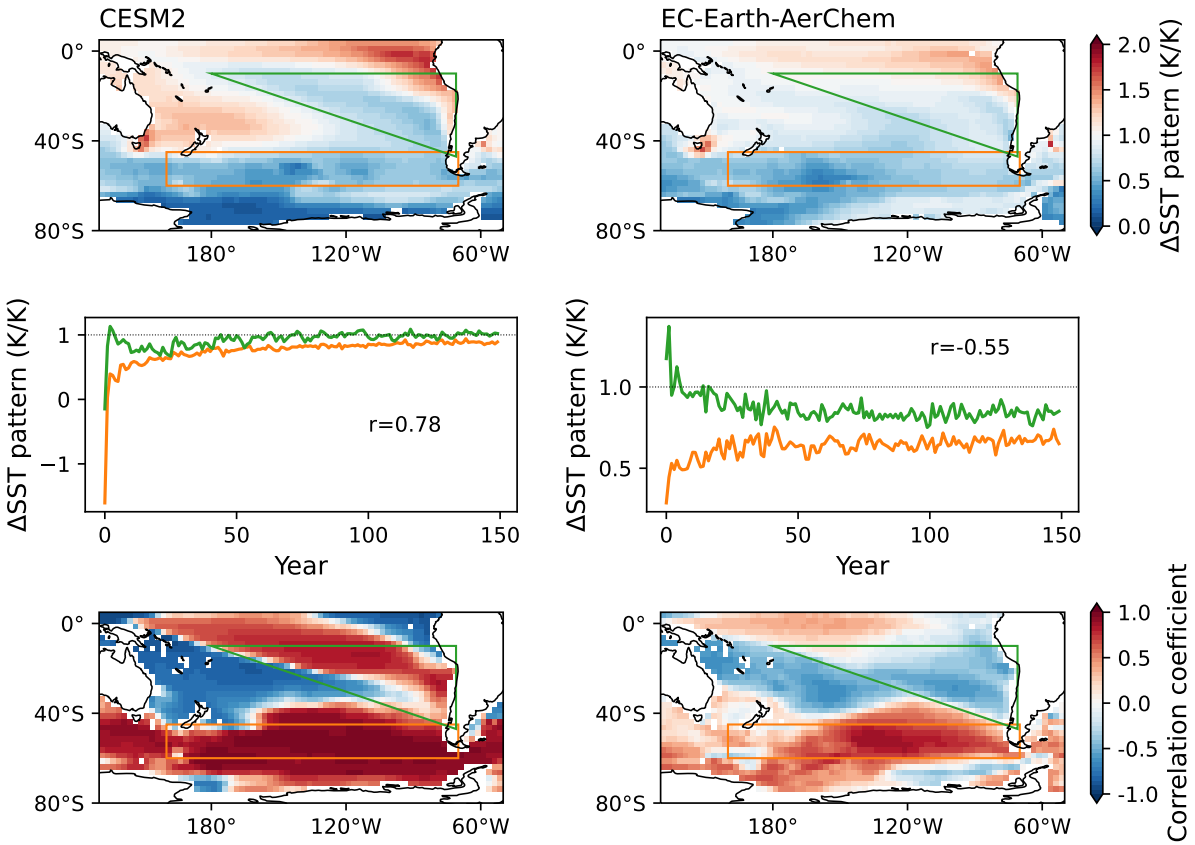

Figure 2.4: Examples of model discrepancy in the spatial distributions, magnitudes, and correlations of SST pattern. The top row shows the SST pattern averaged over years 1-50. The middle row shows the SST pattern timeseries averaged over the SO and SEP regions (note the different y-axis ranges), with the SO-SEP correlation coefficients shown in the figure. The bottom row shows the correlations over the entire 150 years between the SST pattern at each grid point and the area-weighted average of the SST pattern over the SO.

In the forced climate, there is a delayed warming pattern in EC-Earth-AerChem and CESM2 in the SO. In the SEP, CESM2 has a stronger delayed warming than EC-Earth-AerChem, with a clearer horseshoe shape in the South Pacific during the first 50 years (top row in Fig. 2.4). The relatively weak delayed warming in SEP in EC-Earth-AerChem can be attributed to SEP warming within the first 10 years, during which SEP SST warms more than the global-mean SST anomaly. The model-dependent temporal variations reflect different paces of SST responses to external forc-

ing: EC-Earth-AerChem has a sensitive SEP that warms more rapidly than the global-mean SST, while CESM2 has a SEP that warms slower than the global-mean SST under CO_2 forcing. This temporal divergence of the SST pattern timeseries contributes to the contrasting positive and negative SO-SEP correlations in CESM2 and EC-Earth-AerChem, respectively (middle row in Fig. 2.4). The correlation maps further illustrate the different spatial distributions of correlations with the SO, with CESM2 (EC-Earth-AerChem) showing positive (negative) correlations in SEP (bottom row in Fig. 2.4).

Different definitions of SST pattern

The delayed warming pattern over the SO and SEP is robust when using different methods to calculate the SST pattern. Studies have calculated the SST pattern by dividing local SST anomalies by the global-mean warming (hereinafter referred this method to as "division"; e.g., Armour et al., 2013), subtracting the global-mean warming from local SST anomalies (referred to as "subtraction"; e.g., Zhou et al., 2016), or regressing local SST anomalies onto the global-mean warming (referred to as "regression"; e.g., Andrews et al., 2015). Other studies have defined SST pattern by differencing SST anomalies between late and early periods (e.g., Dong et al., 2019), or applying a principal component analysis on SST anomalies (referred to as "PCA"; e.g., Xie et al., 2013). Throughout the paper, I use "division" to calculate the SST pattern because this pattern is easy to interpret and not sensitive to time period selection.

While the SST pattern calculated by subtraction and division exhibits similar spatial distributions of SST pattern and correlations (Fig. 2.5a and c with Fig. 2.3a and c), their SST pattern timeseries differ. In almost all models, the "subtraction" SST pattern timeseries over the SO shows a sharp decrease in the first 10 years, followed by a gradual increase until the end of the simulation, while the SST pattern timeseries over the SEP steadily decreases over time (not shown). The different evolutions of the SST pattern arise from different warming rates relative to the global-mean SST, i.e., the SO SST starts with a similarly small SST value as the global-mean SST, warms slower than the global-mean (denoted by the sharp decrease in the SST pattern timeseries), and later catches up (denoted by the gradual increase in the SST pattern timeseries). While the di-

vision method leads to a large spread in SST pattern timeseries during the first 10 years due to sensitivities of warming magnitude in the SO and SEP with respect to the global-mean, the subtraction method introduces additional temporal variations to almost all models and complicates the correlation results.

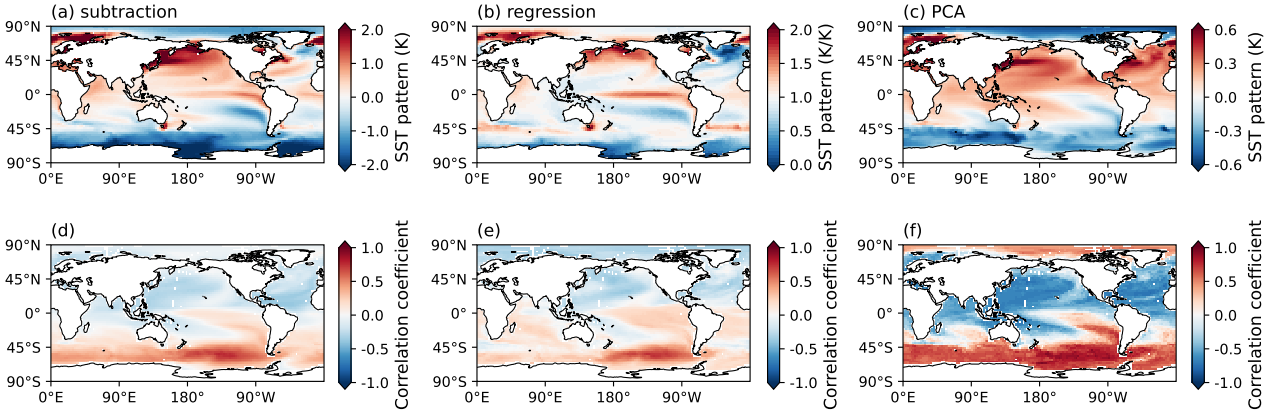

Figure 2.5: Robust SST pattern and correlations between the SO and every grid point using different methods. Multi-model-mean SST pattern maps averaged over years 1-50 (similar to Fig. 2.3a) calculated using subtraction (a), regression (b), and principle component analysis (c). See text for detailed definitions of these methods. (d-f) Multi-model-mean correlations between the SST pattern at each grid point and the area-weighted average of the SST pattern over the SO (similar to Fig. 2.3c), using the three methods to define pattern.

The "regression" SST pattern is very sensitive to the selected period, especially for the SO. The SO SST warms more slowly than the global-mean warming for less than 50 years, with this length being highly model-dependent. This explains the absence of delayed warming over the SO in Fig. 2.5b when calculating the "regression" SST pattern over the first 50 years for all models. The correlation for the "regression" SST pattern is derived from 50-year running regressions between local and global-mean SST anomalies (Fig. 2.5e), yielding a spatial distribution of correlations similar to that of the "division" SST pattern (Fig. 2.3c). While the correlation in the division method measures the inter-annual covariation between the SST pattern timeseries in the SO and SEP, the correlation in the regression method quantifies the covariation between the decadal variability of the SST pattern timeseries. Therefore, caution is needed when comparing results based on different methods to quantify SST pattern.

PCA categorizes different spatial patterns of SST warming based on explained variance. The first PC accounts for the largest variance explained (over 95% in all models), isolating a spatial pattern of uniform warming (not shown). The second PC accounts for the second largest variance explained (ranging from 0.3% to 1.6% across models), isolating a spatial pattern of cooling over the SO and the SEP regions (Fig. 2.5c), consistent with the delayed warming pattern identified by other methods. I do not use the "PCA" SST pattern further because it limits the ability to examine the SO-SEP relationship via correlation. Specifically, as I apply PCA to the spatial covariance matrix of SST anomalies, the second PC captures a spatial pattern where the time variations of grid points are the second most covarying with each other. This means that after reconstructing the original data using only the second PC and producing the "PCA" SST pattern, the temporal variabilities in different regions (e.g., the SO and the SEP) are inherently highly correlated. Consequently, correlating the "PCA" SST pattern timeseries between the SO and SEP would yield either 1 or -1, depending on whether there is a delayed warming or not in grid points. The resulting model-mean correlation at each grid point is thus a probability of models exhibiting delayed warming, rather than measuring the covariations between the SST pattern timeseries in the SO and SEP as denoted by correlations between the "division" SST patterns.

The delayed warming pattern emerging from different methods lies within the SO and SEP regions, indicating robustness in its spatial distribution. However, there is a slight difference in the spatial distribution between the SST pattern defined with respect to the global-mean temperature ("division", "subtraction", and "regression") and the "PCA" SST pattern. The delayed warming pattern calculated relative to global-mean temperature (regardless of which method is used) does not reach the tropics. The "PCA" delayed warming pattern penetrates into the tropics, which can be attributed to the statistical nature of PCA. PCA captures covariations between grid points, making the "PCA" SST pattern more comparable to the correlation maps from other methods (Fig. 2.3c and Fig. 2.5d-e), which show positive correlations from the SO reaching into the tropics, than to their SST pattern maps (Fig. 2.3a and Fig. 2.5a-b). Therefore, I highlight that these patterns are not comparable on a one-to-one basis, and caution has to be taken in their physical interpretation.

2.4 Physical drivers of the warming pattern and SO-SEP relationship

The previous sections demonstrate a robust relationship between the SO and the SEP SSTs in the unforced climate and in a forced climate with or without global-mean warming. In this section, I analyze the impacts of four physical drivers on the correlations between the SO and SEP SSTs across models: the stratocumulus cloud feedback, ocean heat uptake, WES feedback, and total wind speed. I test the pathway of the SO teleconnection proposed by Kim et al. (2022) when the SO is perturbed to cool: cold SST anomalies over the SO are advected equatorward by climatological wind, amplified by subtropical oceanic upwelling, the stratocumulus cloud feedback, and the WES feedback.

2.4.1 Stratocumulus cloud feedback in the unforced and forced climate

I calculate the shortwave cloud feedback by regressing the annual local shortwave cloud radiative flux at the top-of-atmosphere (downward positive) against the annual *local* SST across the entire timeseries (e.g., Kim et al., 2022; Hedemann et al., 2022). This shortwave cloud feedback serves as a proxy for the stratocumulus cloud feedback in stratocumulus-dominated regions, such as off the west coast of South America (black box in Fig. 2.6a, b). In an unforced climate, I refer to this feedback as "radiative restoration strength", i.e., the radiative response that restores the unforced climate back to its equilibrium (e.g., Rugenstein and Armour, 2021). In a forced climate, radiation moves the climate system to a new equilibrium, so I refer to the change of radiation with respect to the change of local SST as "cloud feedback".

Averaged over the designated box off the west coast of South America, the radiative restoration strength (RS_{wSA}) and the cloud feedback (CF_{wSA}) off the west coast of South America are positive and highly related across models ($R^2 = 72\%$; Fig. 2.6c). A positive shortwave cloud feedback indicates an amplifying effect of stratocumulus clouds on the underlying SSTs (Fig. 2.6a, b), i.e., increasing SST reduces the cloud cover, resulting in less reflection of solar radiation and further increasing the underlying SST. Expanding or shrinking the box by 5°in each direction for RS_{wSA} and CF_{wSA} does not affect my results.

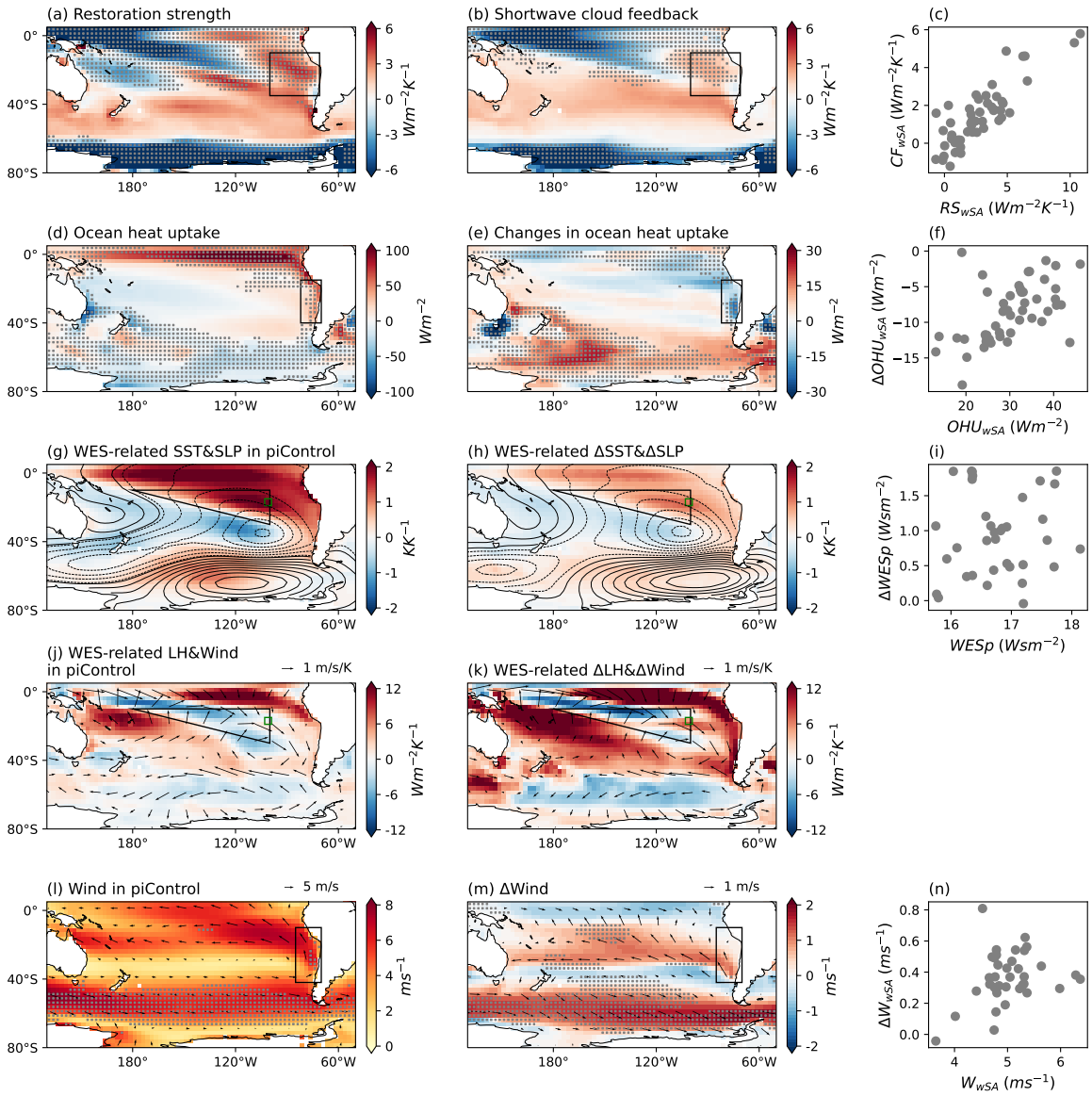

Figure 2.6: Overview of physical drivers in the unforced and forced climate over the 150-year period. See text for detailed definitions. (a) Model-mean restoration strength, with stippling indicating regions of large model spread as standard deviation (SD) $> 2.5\ Wm^{-2}K^{-1}$. (b) Model-mean shortwave cloud feedback, stippled where $SD > 2\ Wm^{-2}K^{-1}$. (c) Inter-model relationship between RS_{wSA} and CF_{wSA}. (d) Model-mean ocean heat uptake in piControl, stippled where $SD > 9\ Wm^{-2}$. (e) Model-mean changes in ocean heat uptake, stippled where $SD > 7\ Wm^{-2}$. (f) Inter-model relationship between OHU_{wSA} and ΔOHU_{wSA}. (g) Model-mean WES-related unforced SST (shading) and SLP (contours). Negative (positive) SLP contours are dashed (solid) with contour interval 60 Pa. (h) As in (g), but for anomalous SST and SLP. (i) Inter-model relationship between $WESp$ and $\Delta WESp$. (j) Model-mean WES-related unforced LH (shading) and wind (arrows). (k) As in (j), but for anomalous LH and wind. (l) Model-mean wind in piControl, stippled where $SD > 1.2\ m/s$. (m) Model-mean changes in wind, stippled where $SD > 0.5\ m/s$. (n) Relationship between W_{wSA} and ΔW_{wSA} across models. The thresholds of standard deviations are subjectively selected to highlight regions with large model spread.

2.4.2 *Oceanic upwelling strength in the unforced and forced climate*

Strong oceanic upwelling occurs off the west coast of South America, where the Humboldt current induces Ekman transport, bringing cold waters up to the surface (e.g., Kämpf and Chapman, 2016). I calculate the net downward surface heat flux to quantify the ocean heat uptake. I identify a region off the west coast of South America that absorbs heat in the unforced climate and experiences reductions in ocean heat uptake in response to the abrupt-4xCO2 forcing (black box Fig. 2.6d, e). Such a reduction in ocean heat uptake can be attributed to the warming caused by a weakened eastern boundary current in a warming climate, which can be explained by a poleward shift of the South Pacific subtropical high (Bograd et al., 2023). The reduction in ocean heat uptake ranges from 1% to 108% of the unforced heat flux across models, with a model mean of 33%, meaning the ocean still takes up heat in a warmer climate, but to a lesser extent.

Across models, the unforced ocean heat uptake in the designated box off the west coast of South America (OHU_{wSA}) is positively related to the anomalous ocean heat uptake within the same area (ΔOHU_{wSA}) ($R^2 = 28\%$; Fig. 2.6f). Models with stronger ocean heat uptake in the unforced climate have smaller reductions in response to the abrupt-4xCO2 forcing. Notably, inter-model relationships between the unforced ocean heat uptake and its changes under CO_2 forcing are negative, globally and in most regions (not shown), following the "capacity-for-change" theory (Kajtar et al., 2021). However, a positive relationship emerges in the OHU_{wSA} box, with $R^2 > 20\%$ in some grid points, indicating that this positive relationship does not appear by chance. The mechanisms underlying this positive relationship may be related to the coastal upwelling system, shortwave cloud feedback, wind, and ocean stratification. A detailed analysis is needed to identify the cause and interplay of the many actors at play. Expanding or shrinking the box by 5°in each direction for OHU_{wSA} and ΔOHU_{wSA} does not affect my results.

2.4.3 *WES feedback in the unforced and forced climate*

The positive WES feedback promotes interaction between tropical and extratropical regions (e.g., Xie and Philander, 1994; Zhang et al., 2014). In this section, I follow the methodology

of Zhang et al. (2014) to demonstrate the mechanisms of WES feedback in the South Pacific subtropical region, which enhances the SO-SEP relationship in the unforced and forced climate.

Within the SEP region, the WES feedback is positive. Following Zhang et al. (2014), I analyze WES-related variabilities of SST, sea-level air pressure (SLP), wind, and latent heat flux (LH) by regressing these variables onto the normalized unforced SST timeseries averaged over a small region in the southeast Pacific (19°S–15°S, 103°W–107°W; the green box in Fig. 2.6g-h, j-k) for each model. The model-mean regressions between these variables and normalized unforced SST using min-max scaling are shown in Fig. 2.6g, j. The model-mean regressions show that when the unforced SST in this region increases, the surrounding area (the small triangle in Fig. 2.6g) experiences an increased SST and a weakened subtropical high. This induces anomalous northwesterly winds that weaken the trade wind and reduce upward LH (Fig. 2.6j), increasing the downward surface heat flux and further warming the SST. These results align with Zhang et al. (2014), showing the mechanism of the positive WES feedback. Although not explicitly discussed in Zhang et al. (2014), the selected box in the southeast Pacific needs to be small enough to avoid averaging out spatial variations in the WES-related SST, SLP, LH, and wind, while its location does not qualitatively affect the interplay between these physical quantities. I use the same box as Zhang et al. (2014) to ensure comparability with their Fig. 1.

The above positive WES feedback mechanism is shown to be at work in an unforced climate. Similar feedback processes amplify SST warming in a forced climate through the same interplay between SST, SLP, LH, and wind. However, the global-mean warming can distort the WES feedback when regressing the LH anomalies onto normalized SST anomalies, which increases upward LH in the southeast Pacific due to its dampening effect on the dominant SST warming under CO_2 forcing. To address this distortion, I regress anomalies of SST, SLP, wind, and LH on the normalized SST *pattern*, which removes the effect of global-mean warming and allows the WES feedback mechanisms to emerge in the SEP region (Fig. 2.6h, k).

I use a simple metric—the WES parameter—to quantify the magnitude of this feedback in the small triangular region, where increased SSTs coincide with reduced upward LH. The WES

parameter measures the change in LH per unit change in zonal wind speed, following Vimont et al. (2009):

$$WESp = LH\frac{u}{\bar{w}^2}, \tag{2.1}$$

where LH is upward latent heat flux, u is zonal wind speed, and $\bar{w}^2 = \sqrt{U^2 + V^2 + \hat{w}^2}$, with $\hat{w}$ accounting for submonthly wind variance (Czaja et al., 2002) and being set to $\hat{w} = 4m/s$ as in Vimont et al. (2009). I calculate the WES parameter using unforced LH and wind speeds in piControl and average it over the small triangle region (referred to as $WESp$). The WES parameter under CO_2 forcing is calculated in the same manner, using LH and wind speeds from the abrupt-4xCO2 simulations (*not* anomalies). The difference between these two parameters, $\Delta WESp$, represents the change in WES feedback due to external forcing.

In response to CO_2 forcing, the positive WES feedback in the South Pacific subtropical region strengthens. In all models except GISS-E2-1-G, $WESp$ increases by up to $1.9Ws/m^2$ from piControl to abrupt-4xCO2 simulations, indicating that a reduced trade wind further decreases the upward LH, leading to more SST warming. There is no significant relationship between model spreads in $WESp$ and $\Delta WESp$ (Fig. 2.6i).

2.4.4 Total wind speed in the unforced and forced climate

I calculate the near-surface total wind speed using the zonal and meridional wind components ($W = \sqrt{U^2 + V^2}$). The total wind speed near the west coast of South America is dominated by meridional winds, transporting SST signals from the SO equatorward (e.g., Dong et al., 2022; Kim et al., 2022). I identify a region along the west coast of South America that shows a strong meridional wind in piControl (Fig. 2.6l), coinciding with the eastern boundary of the South Pacific subtropical high (SPSH) (e.g., Flores-Aqueveque et al., 2020). Under CO_2 forcing, the total wind speed increases at the southern edge of the analyzed region (Fig. 2.6m) due to the poleward displacement of the SPSH, which strengthens (weakens) coastal winds south (north) of 40°S (e.g., Rykaczewski et al., 2015). There is no correlation between total wind speed near the west coast of South America in piControl (W_{wSA}) and its changes under CO_2 forcing (ΔW_{wSA}). Note that

I use the total wind speed for the analyses rather than wind advection, which includes anomalous temperature advection (VT' as in Dong et al. (2022); Kim et al. (2022)). This choice is due to VT' being unsuitable for analyses of cross-model relationships for two reasons. First, T' is centered around zero, meaning the average of wind advection for each model would be zero. Second, using T' introduces additional model discrepancies, as discussed in section 3c.

2.4.5 The impacts of physical drivers in an unforced climate

In the unforced climate, models agree that the SSTs over the SEP region are positively correlated with the SO SST. Correlation coefficients in Fig. 2.7a replicate those shown in Fig. 2.1c. The small model spread over the SO region is expected, as the SSTs at each grid point in the SO region are highly correlated with the SST averaged over the SO box within each model.

To study the impacts of physical drivers on SO-SEP correlation across models, I regress the correlations between unforced SSTs at each grid point and the SO SST (Fig. 2.7a) onto RS_{wSA} (Fig. 2.6a), OHU_{wSA} (Fig. 2.6d), $WESp$, and W_{wSA} (Fig. 2.6l). The regression coefficients at each grid point are plotted in Fig. 2.7b-e, in which the stippling indicates relatively strong relationships (the coefficient of determination R^2 being larger than 20%). Positive regression coefficients in the SEP region, e.g., in Fig. 2.7b, indicate that models with larger RS_{wSA} tend to have stronger correlations between the SO SST and SSTs in this region. Conversely, negative regression coefficients in the SEP region, e.g., in Fig. 2.7c, indicate that models with smaller OHU_{wSA} tend to have stronger correlations between the SO SST and SSTs in this region. Based on Fig. 2.7b-e, relationships between the four physical drivers and SO-SEP correlations are discussed below.

SO-SEP correlations in the unforced climate are positively related to RS_{wSA} (Fig. 2.7b). The regression coefficients reveal a horseshoe pattern of positive relationships. Note that I do not expect high regression coefficients in the SO box since I do not anticipate RS_{wSA} contributing to the correlation between the SO SST and the SSTs at each grid point within the SO region. RS_{wSA} affects the SO-SEP correlation within the RS_{wSA} box where the stratocumulus occurs ($R^2 > 20\%$; Fig. 2.6a). Outside the stratocumulus region, RS_{wSA} does not contribute to correlations between the SO SST and the SSTs at each grid point (no stippling indicates $R^2 < 20\%$; Fig. 2.7b).

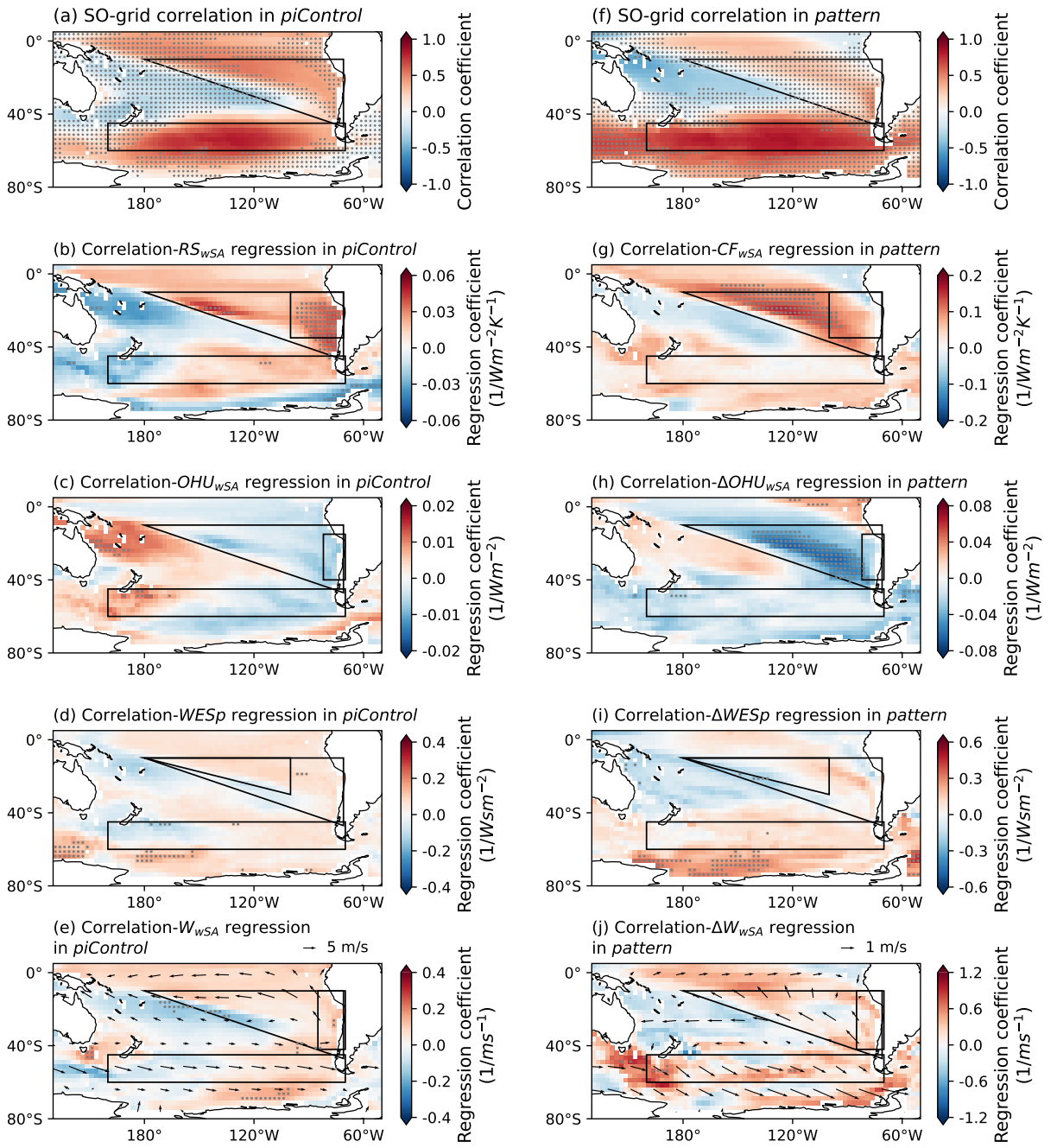

Figure 2.7: Regressions between physical drivers and SST correlations. See the text for more explanations. (a) Multi-model mean correlations between unforced SST at each grid point and SO SST (same as Fig. 2.1c). Stippling indicates large model spread ($SD > 0.15$). The thresholds of standard deviations are subjectively selected to highlight regions with large model spread. (b) Inter-model relationships between SST correlations at each grid point in (a) against RS_{wSA}, stippled where $R^2 > 20\%$. (c-e) Same as (b), but regressed against OHU_{wSA}, $WESp$, and W_{wSA}. (f) As in (a), but for correlations in the pattern of the forced response, stippled where $SD > 0.3$. (g-j) Same as (b-e), but regressing SST correlations in the pattern of the forced response against CF_{wSA}, ΔOHU_{wSA}, $\Delta WESp$, and ΔW_{wSA}.

SO-SEP correlations in the unforced climate are negatively related to OHU_{wSA} (Fig. 2.7c). A similar horseshoe pattern of negative relationships is seen in the South Pacific, though with R^2 values less than 20%.

SO-SEP correlations in the unforced climate are positively related to $WESp$ (Fig. 2.7d). The horseshoe pattern of positive relationships indicates that models with stronger $WESp$ exhibit stronger correlations between unforced SO SST and SSTs in the SEP region ($R^2 < 20\%$ in most locations).

SO-SEP correlations in the unforced climate are positively related to W_{wSA} (Fig. 2.7e). The horseshoe pattern of positive relationships indicates that models with stronger W_{wSA} have stronger correlations between unforced SO SST and SSTs in the SEP region ($R^2 < 20\%$). While Dong et al. (2022) and Kim et al. (2022) suggested that wind advection plays a critical role in transporting the SO SST to SEP, it is unsuitable for my cross-model analyses, as discussed in the previous section, and is therefore not considered in this study.

In short, in an unforced climate, stronger shortwave cloud feedbacks are most robustly associated with a stronger relationship between the SO and SEP. Climatological ocean heat uptake, WES feedback, and along-shore wind speed also contribute but are less good predictors of spread across climate models.

2.4.6 The impacts of physical drivers in the pattern of the forced response

In a forced climate, models agree that the SST pattern (i.e., warming anomaly normalized with the global-mean temperature; see section 3c above) over the SEP is positively correlated with the SO (Fig. 2.7f). The large model spread in the SEP can be attributed to diverse model representations of the delayed warming pattern (see Section 3c(1)).

Similar to the unforced climate, SO-SEP correlations in the SST pattern are positively related to CF_{wSA} (Fig. 2.7g). CF_{wSA} amplifies SST anomalies transported from the SO to the SEP. The horseshoe-shaped positive relationships in the South Pacific indicate that models with higher CF_{wSA} tend to have stronger SO-SEP correlations. In the SEP regions, CF_{wSA} accounts for more

than 20% of the model spread in correlations with the SO SST, indicating a relationship between CF_{wSA} and SO-SEP correlations that is not confined to the CF_{wSA} box.

The remote effect of CF_{wSA} on SO-SEP correlations outside of the CF_{wSA} box might be associated with the WES feedback. Stippled locations in Fig. 2.7g overlap with the triangle region of the WES feedback (Fig. 2.6g-h and j-k). $\Delta WESp$ is positively related to CF_{wSA} (not shown), presumably owing to the poleward shift of the SPSH that strengthens southwesterly winds in the South Pacific subtropical region (Fig. 2.6m). This joint effect of the WES feedback and stratocumulus cloud feedback on subtropical South Pacific SSTs was detailed in Zhang et al. (2014).

SO-SEP correlations in the SST pattern are negatively related to ΔOHU_{wSA} (Fig. 2.7h). The horseshoe-shaped negative relationships in the South Pacific indicate that models with a more negative ΔOHU_{wSA}—more reductions in OHU_{wSA}—tend to have stronger SO-SEP correlations outside the ΔOHU_{wSA} box ($R^2 > 20\%$). Similar to CF_{wSA}, the non-local effect of ΔOHU_{wSA} on SO-SEP correlations is associated with the strengthened southwesterly winds and stronger WES feedback, as $\Delta WESp$ is negatively correlated with ΔOHU_{wSA} (not shown).

SO-SEP correlations in the SST pattern are positively related to $\Delta WESp$ (Fig. 2.7i). A larger $\Delta WESp$ indicates a more amplified warming effect on SEP SST. The positive relationship between SO-SEP correlations and $\Delta WESp$ indicates that models with stronger $\Delta WESp$ tend to have stronger SO-SEP correlations, though R^2 values are less than 20% in the SEP region. My finding indicates that $\Delta WESp$ alone does not explain the model spread of SO-SEP correlations, and I hypothesize an indirect effect of $\Delta WESp$ on SO-SEP correlations when combined with CF_{wSA} and ΔOHU_{wSA}. I acknowledge that my cross-model analysis might not be the ideal approach to identify the physical mechanisms behind the SO-SEP relationship, since they might be highly, but differently linked within each model on different timescales and I analyze long-term time averages across models.

SO-SEP correlations in the SST pattern are positively related to ΔW_{wSA} (Fig. 2.7j). A larger ΔW_{wSA} means more SO SST signals being transported equatorward by anomalous wind. The

positive relationship between SO-SEP correlations and ΔW_{wSA} indicates that models with stronger ΔW_{wSA} tend to have stronger SO-SEP correlations ($R^2 < 20\%$ in the SEP region).

In short, in a forced climate, stronger shortwave cloud feedbacks and larger reductions in ocean heat uptake are most robustly associated with a stronger relationship between the SO and SEP. Changes in WES feedback and along-shore wind speed also contribute but are less good predictors of spread across climate models.

2.5 Summary and discussion

I analyze the relationship between the Southern Ocean and the southeastern subtropical Pacific using 53 CMIP6 models. Building on the mechanism proposed by Kim et al. (2022), I investigate the impacts of stratocumulus cloud feedback, ocean heat uptake, WES feedback, and total wind speed on the correlations between the two regions. I find that:

1. In an unforced climate, the SO and SEP SSTs are positively related both in single models across time (by internal variability; Fig. 2.1b and c) and across models averaged over time (by their mean-state biases; Fig. 2.1e). The model spread of the SO-SEP correlations is partially explained by the radiative restoration strength of shortwave clouds off the west coast of South America (Fig. 2.7c), while the impacts of ocean heat uptake, WES feedback, and total wind speed on SO-SEP correlation are weak (Fig. 2.7e, g, and i). A model with a strong SO-SEP correlation tends to have a strong shortwave restoration strength off the west coast of South America in the unforced climate.

2. In a forced climate, the SO and SEP SST anomalies are positively and highly correlated. Both correlations in models through time (Fig. 2.2b) and across models (Fig. 2.2d) show a strong relationship between the two regions in response to the abrupt-4xCO2 forcing. However, such relationships can be dominated by models' global-mean response: a very warm model will show strong warming in both places. This motivates subsequent analyses of the SST pattern.

3. A delayed warming pattern over the SO and SEP is robustly connected after removing the global-mean warming with different methods (Fig. 2.3c and Fig. 2.5). The correlations between the SST pattern timeseries averaged over the SO and SEP are highly model-dependent and vary differently in time (Fig. 2.3b) due to distinct temporal variations of SST pattern timeseries (Fig. 2.4), while the relationship across models is significantly positive between the two regions (Fig. 2.3e). The large spread in the SO-SEP correlations can be attributed to the shortwave cloud feedback and the anomalous ocean heat uptake off the west coast of South America (Fig. 2.7g-h), while changes in WES feedback and anomalous total wind speed have little impacts (Fig. 2.7i-j). A model with a strong SO-SEP correlation in the SST pattern tends to have a strong shortwave cloud feedback and a greater reduction in ocean heat uptake in response to abrupt-4xCO2 forcing.

Other factors like Rossby-wave dynamics over the South Pacific (Dong et al., 2022) and wind anomalies over the southern high latitude (Wang et al., 2022) also connect the two regions. I conducted a preliminary analysis to investigate whether the SO-SEP correlation is predominantly driven by ENSO as well as tropical Pacific decadal variability. My results suggest that the SO-SEP relationship is dominantly influenced by extratropical climate effects on the SEP (see Section 3). The direction of the SO-SEP relationship remains a subject of ongoing research, with a causality analysis between the SSTs over the two regions currently being prepared by the authors.

In Section 4f, I show that a stronger CF_{wSA} is associated with a stronger SO-SEP correlation. Given that the majority of climate models underestimate the observed shortwave cloud feedback over the subtropical regions (e.g., Myers et al., 2021), they may underestimate the SO-SEP teleconnection (Kim et al., 2022; Kang et al., 2023a). However, I also show that a larger ΔOHU_{wSA} is associated with a stronger SO-SEP correlation. Since climate models tend to underestimate the climatological oceanic upwelling along the coast of Peru (e.g., Fox-Kemper et al., 2021; Richter, 2015; Ma et al., 2019), I would expect this relationship to contribute to an overestimation of the SO-SEP teleconnection in climate models. If I compare the simulated SO-SEP teleconnections in climate models to observations, the opposing effects of underestimated RS_{wSA} and OHU_{wSA}

on the SO-SEP correlation may lead us to different conclusions. As RS_{wSA} and OHU_{wSA} are negatively correlated across models (not shown; $R^2 = 23\%$), i.e., models with stronger RS_{wSA} have smaller OHU_{wSA}, I hypothesize that the two effects are linked in complex ways that play out differently across climate models. I suggest that SO-SEP teleconnections be studied across a diverse set of models until both effects and their interactions are understood.

An underestimated SO-SEP teleconnection in climate models may point to an underestimated equilibrium climate sensitivity. My findings connect the delayed *warming* over the SO and the SEP, showing that a warmer SO links to a warmer SEP. As global warming progresses, the SO is expected to show reductions in sea ice extent and warming over the deep ocean, eventually resulting in Antarctic polar warming amplification (as reviewed in Cai et al., 2023). When Antarctic polar amplification takes effect, given the SO-SEP teleconnection, a warmer SO implies a warmer SEP which, according to the pattern effect theory, is a hot spot in determining the radiative feedback of the Earth system. Warming over the eastern tropical Pacific reduces the lower tropospheric stability and low cloud cover, resulting in a weak negative lapse rate feedback and a strong positive cloud feedback. Consequently, the radiative feedback of the Earth system becomes less negative, indicating a higher equilibrium climate sensitivity or greater warming rate (e.g., Andrews and Webb, 2018; Dong et al., 2019, 2020; Alessi and Rugenstein, 2023). Hence, if the SO-SEP teleconnection is underestimated in climate models, the projected SEP warming following the projected SO warming might also be underestimated, implying an underestimation of equilibrium climate sensitivity. Conversely, if the SO-SEP teleconnection is overestimated in climate models, the projected SEP warming could be attributed to factors other than the SO climate. Therefore, the role of the SO teleconnection to the tropics needs to be considered when projecting future climate.

CHAPTER 3 CONSTRAINING THE RELATIONSHIP BETWEEN SEA SURFACE TEMPERATURE TRENDS IN THE SOUTHERN OCEAN AND SOUTHEASTERN TROPICAL PACIFIC OVER 1985–2014

3.1 Introduction

Since the 1970s, observed sea surface temperatures (SSTs) over the Southern Ocean and southeastern tropical Pacific have exhibited a cooling trend, whereas state-of-the-art coupled climate models generally simulate a warming trend in both regions. The warming trend in the southeastern tropical Pacific stems from errors in simulating internal variability, teleconnections, or responses to anthropogenic forcing (e.g., Watanabe et al., 2021a; Olonscheck et al., 2020; Seager et al., 2022; Wills et al., 2022). The warming trend in the Southern Ocean can be attributed to internal variability or linked to biases in Antarctic meltwater and misrepresentations of key atmospheric processes, such as the Southern Annular Mode and cloud-related shortwave radiation (e.g., Zhang et al., 2019a; Rye et al., 2020; Purich et al., 2016; Kostov et al., 2018). Additionally, the low resolution of climate models may hinder accurate simulations of SST trends in both regions, as the warm bias of SST trends is reduced in high-resolution, eddy-resolving hindcasts using the Community Earth System Model (CESM; Yeager et al. (2023)).

Growing evidence suggests that the SST trend over the southeastern tropical Pacific is affected by the SST trend in the Southern Ocean. Studies have tested the robustness of this teleconnection by conducting perturbation experiments in coupled climate models—either under pre-industrial control conditions or in the presence of external CO_2 forcing. The imposed cooling or warming in the Southern Ocean leads to a decrease or increase in SSTs over the southeastern tropical Pacific, respectively (e.g., Mechoso et al., 2016; Kang et al., 2020; Zhang et al., 2021; Kim et al., 2022; Dong et al., 2022; Yu and Pritchard, 2019; Xiang et al., 2018). This teleconnection has been invoked to relate the observed cooling trend in the southeastern tropical Pacific to that in the Southern Ocean. For example, Hartmann (2022) linked the Antarctic ozone hole to SST cooling trends in both regions based on observational analyses; Kang et al. (2023b) attributed at least part of the

observed southeastern tropical Pacific cooling trend to the Southern Ocean SST trend by restoring simulated Southern Ocean SST anomalies in CESM historical simulations to the observed evolution from 1970 to 2014, following the Southern Ocean "Pacemaker" simulation protocol. This Southern Ocean–southeastern tropical Pacific relationship is likely underestimated in most climate models, and improving its representation could impact equilibrium climate sensitivity and future climate projections (Kang et al., 2023a).

The subtropical stratocumulus cloud feedback and ocean heat uptake are key factors influencing the strength of the relationship between the Southern Ocean and the southeastern tropical Pacific. Kim et al. (2022) proposed a physical pathway for the Southern Ocean teleconnection to the tropical Pacific when the Southern Ocean is perturbed to cool. This pathway involves subtropical stratocumulus cloud feedback, climatological winds, and ocean heat uptake along the west coast of South America, and the wind-evaporation-SST (WES) feedback in the tropics. Among these factors, positive stratocumulus cloud feedback is the primary driver of relationship strength, with models exhibiting stronger cloud feedback showing a greater cooling response in the southeastern tropical Pacific under the same Southern Ocean perturbation. Zheng et al. (Accepted) examined this relationship and the effects of physical drivers involved in the pathway proposed above on interannual timescales, using model outputs from pre-industrial control simulations and forced simulations with an abrupt quadrupling of CO_2 across Coupled Model Intercomparison Project Phase 6 (CMIP6) models. Their findings confirmed the key role of subtropical stratocumulus cloud feedback while also revealing the important role of ocean heat uptake in the upwelling region, showing that models with stronger stratocumulus cloud feedback and weaker ocean heat uptake have stronger interannual SST correlations between the Southern Ocean and the southeastern tropical Pacific.

Building on the robust relationship between SST trends in the southeastern tropical Pacific and the Southern Ocean identified in perturbation experiments and observations, I pose three key questions:

1. Are the erroneously positive SST trends in both regions related?

2. Are the SST trends in both regions more strongly related in models with large equilibrium climate sensitivity?

3. Can I use the observed subtropical stratocumulus cloud feedback and ocean heat uptake to constrain the simulated relationship between SST trends in the Southern Ocean and the southeastern tropical Pacific?

To answer these questions, I analyze the SST trends in the Southern Ocean and the southeastern tropical Pacific, the subtropical stratocumulus cloud feedback, and the ocean heat uptake off the west coast of South America from 1985 to 2014 using historical simulations from all available CMIP6 models, and I compare them with the observations. Instead of conducting perturbation experiments on climate models, I assess the Southern Ocean–southeastern tropical Pacific relationship in widely used coupled model outputs to avoid potential side effects introduced by imposed perturbations.

3.2 Data and Methods

3.2.1 CMIP6 Climate Models, Reanalyses, and Observations

I analyze observed SST trends from the fifth generation ECMWF atmospheric reanalysis of the global climate (ERA5) (Hersbach et al., 2023), the Extended Reconstructed SST dataset v5 (ERSSTv5) (Huang et al., 2017), the Hadley Centre Sea Ice and Sea Surface Temperature dataset (HadISST 1.1) (Rayner et al., 2003), and the Optimum Interpolation Sea Surface Temperature dataset (OISST v2.1) (Huang et al., 2021). To calculate stratocumulus cloud feedback, I use the SST products listed above alongside shortwave radiation fluxes at top-of-atmosphere from the International Satellite Cloud Climatology Project radiative flux profile product (ISCCP-FH) (Zhang and Rossow, 2023). Ocean heat uptake is analyzed using surface radiation fluxes from the ERA5 (Hersbach et al., 2023), the Diagnosing Earth's Energy Pathways in the Climate system dataset (DEEP-C) (Liu and Allan, 2022), and the NOAA-CIRES-DOE Twentieth Century Reanalysis Project version 3 (20CR) (Slivinski et al., 2019). These observational and reanalysis datasets cover 1985–2014, while there are other products that do not span the exact time period but are included

for additional information (A.1). I use annual data for all observations and reanalyses to remove monthly variabilities, which are likely associated with El Niño–Southern Oscillation (ENSO) and its strong teleconnection to the Southern Ocean (e.g., Yuan, 2004; Li et al., 2021). All datasets are linearly interpolated to a 2.5°× 2.5° spatial resolution.

I analyze simulated SST, shortwave radiation fluxes at top-of-atmosphere, and surface radiation fluxes from historical simulations across 42 CMIP6 models (Table A.1). Similar to the observational data, I use annual means and re-grid all model outputs to a 2.5°x 2.5° resolution. My analysis focuses on the 1985–2014 period, a 30-year period different from those used in previous studies on historical SST trends but sharing key spatial features (Wills et al., 2022; Dong et al., 2021). Given the relatively short period, it is hard to distinguish the forced trend from internal variability, particularly in regions with small trends (e.g., the Southern Ocean and the southeastern tropical Pacific; Figure 3.1b). The effect of internal variability can be reduced by ensemble averaging in models with multiple ensemble members (Table S1). However, averaging ensembles makes it incomparable with the observations and reduces the number of models available for cross-model analyses. In this study, I show results primarily based on the first ensemble member from each CMIP6 model, while also estimating the impact of internal variability through bootstrapping analysis (see section 2.3).

I analyze the Southern Ocean–southeastern tropical Pacific relationship with implications for the hot model problem, using ECS data from (Zelinka et al., 2020). ECS is the warming in response to external forcing when the climate system is equilibrated, and it has shown a large inter-model spread for decades (e.g., Knutti et al., 2017; Forster et al., 2023). The "hot model" problem refers to the significantly higher ECS values simulated in CMIP6 than earlier phases, which can be attributed to a stronger shortwave cloud feedback in the extratropics and SST trend pattern in the tropical Pacific (Hausfather et al., 2022; Zelinka et al., 2020; Rugenstein et al., 2023).

3.2.2 *Quantification of the Southern Ocean-southeastern tropical Pacific Relationship, Shortwave Cloud Feedback, and Ocean Heat Uptake*

I quantify the relationship between SST trends in the Southern Ocean and the southeastern tropical Pacific using regression coefficients and coefficients of determination (R^2) from linear regression analyses across CMIP6 models. This approach assesses the strength of the cross-model relationship rather than the strength of the ones within individual models. In other words, I do not assess whether a particular model exhibits a stronger relationship than others. Additionally, this approach is not applicable to observed SST trends, as the size of observational products is insufficient for obtaining a cross-observation relationship.

I calculate shortwave cloud feedback by regressing local shortwave cloud radiation flux against local SST over 1985-2014 in observations and CMIP6 models. Shortwave cloud radiation fluxes are computed by subtracting the clear-sky outgoing shortwave radiation flux at the top-of-atmosphere from the total outgoing shortwave radiation flux at the top-of-atmosphere (downward positive). Trends are included in both shortwave cloud radiation flux and SST timeseries for regression to enable a physically interpretable assessment of the role of shortwave cloud feedback in affecting the relationship between SST trends. I note that detrending these timeseries does not affect my results, as the 30-year trends of both variables within the subtropical stratocumulus region are small relative to their internal variability. My quantification of shortwave cloud feedback is different from Zelinka et al. (2020), which regressed local shortwave cloud radiation flux against global-mean SST. Nevertheless, my results are highly correlated with theirs in the subtropical stratocumulus cloud region ($r = 0.55$; 95% confidence interval from boostrapping ensemble members is $[0.47, 0.85]$), with a stronger focus on the local coupling between shortwave cloud radiation and SST. My shortwave cloud feedback also differs from the low-cloud sensitivity to SST calculated by cloud controlling factor analysis (e.g., Kang et al., 2023b). The cloud controlling factor analysis accounts for covariations between SST and other factors, isolating their effects on shortwave cloud radiation. My study focuses on the overall variation between shortwave cloud radiation and the underlying SST, while leaving the decomposition of other contributing factors for future work.

I calculate the net surface heat flux (positive downward) to quantify the ocean heat uptake in observations and CMIP6 models. I investigate the role of ocean heat uptake in the Southern Ocean-southeastern tropical Pacific relationship by analyzing ocean heat uptake variability, which I define as the standard deviation of ocean heat uptake over time. The 30-year trend of the ocean heat uptake is included in this calculation for a physically interpretable assessment of its role in affecting the Southern Ocean-southeastern tropical Pacific relationship based on SST trends. In the upwelling region of interest, the 30-year trend in ocean heat uptake is smaller than its internal variability in 38 out of 42 models (not shown). Therefore, whether or not the trend is removed before calculating the standard deviation does not affect my results.

3.2.3 Bootstrapping analysis on estimating the internal variability uncertainty

I analyze the effect of internal variability using bootstrapping analysis, in which ensemble members are resampled over 5000 iterations. Resampling applies only to models with more than one ensemble member. For models with only one ensemble member, the same member is retained across iterations, whereas for models with multiple ensemble members, the selected member varies in each iteration.

The resampled ensemble members are then used for different analyses throughout the manuscript. In Section 2, they are first used to compute the multi-model mean SST trends at each grid point, after which a subjectively chosen threshold is applied to estimate the spread in the bootstrapped SST trend, highlighting regions where the effect of internal variability on local SST trends is large. The second use of resampled ensemble members in Section 2 involves conducting cross-model regression analyses, where the effect of internal variability on the Southern Ocean–southeastern tropical Pacific relationship is assessed by presenting the 95% confidence intervals of the bootstrapped results. In Section 3, the analysis mirrors that of Section 2, where thresholds of model-mean cloud feedback and ocean heat uptake are selected to highlight regions largely affected by internal variability. In Section 4, the resampled ensemble members are used in cross-model regression analyses with a sliding-window approach. The results from all bootstrapping iterations are included when determining constraints, accounting for the effects of internal variability on the role of shortwave

cloud feedback and ocean heat uptake variability. Overall, this study does not remove the effect of internal variability (e.g., due to ENSO and other climatic variabilities) but rather provides an estimate of the uncertainty it introduces to my results.

3.3 Global-mean SST Trend Dominating the Southern Ocean-southeastern tropical Pacific Relationship

The observed SST over the Southern Ocean and the southeastern tropical Pacific shows a cooling trend from 1985 to 2014, while the simulated SST shows a delayed warming in these regions, consistent with Wills et al. (2022) (Figure 3.1a-b). The discrepancies between simulated and observed SST trends have been discussed in previous papers (e.g., Watanabe et al., 2021a; Olonscheck et al., 2020; Seager et al., 2022; Wills et al., 2022). I describe the small, positive SST trends over the southeastern tropical Pacific and the Southern Ocean as "delayed warming". Note that this term does not refer to a temporal lag in warming between an earlier and later period (e.g., Andrews et al., 2015). Rather, it characterizes the spatial pattern of SST warming, where the Southern Ocean and southeastern tropical Pacific warm less than the global-mean SST over this 30-year period. The delayed warming trends in the southeastern tropical Pacific and parts of the Southern Ocean are robust across different ensemble members, as indicated by the absence of stippling in these regions. I analyze SST trends within a triangular region over the southeastern tropical Pacific (hereinafter referred to as SEP) and a rectangular region over the Pacific sector of the Southern Ocean (hereinafter SO). The SEP region is defined based on the delayed warming area in Figure 3.1b that overlaps with the cooling area in Figure 3.1a. Expanding or shrinking the triangle by 5° in each direction does not affect my results. The SO region is selected based on the cooling area in Figure 3.1a that overlaps with the robust delayed warming area in Figure 3.1b, which also matches the Southern Ocean region analyzed in Dong et al. (2022). Expanding the SO box across the longitudinal band weakens its relationship with SEP but does not qualitatively change my results.

The delayed warming trends over the SO and SEP are related across models and are largely attributed to the global-mean SST trend (Figure 3.1c). The positive cross-model relationship between SO and SEP SST trends remains robust when accounting for the confidence interval of

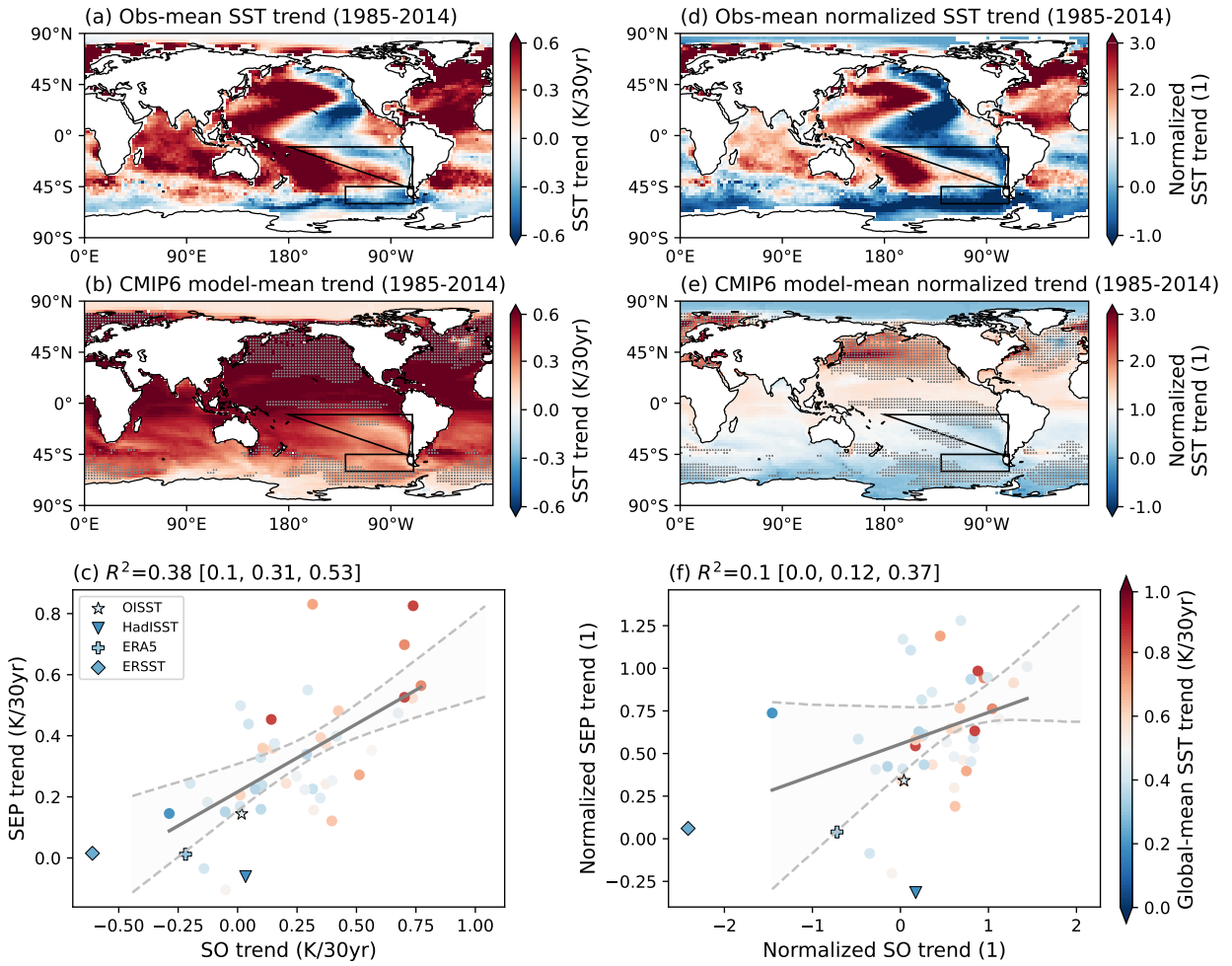

Figure 3.1: Overview of annual-mean SST trends and SO-SEP relationships over 1985-2014. (a) Observed trend map, averaged over four products (see Section 2.1 and A.1). (b) Simulated trend map, averaged over 42 CMIP6 model simulations using the first ensemble member for each model (see Table A.1). Stippling indicates regions where the standard deviation (sdv.) from bootstrapping different ensemble members exceeds 0.05 K/30yr, highlighting areas of large internal variability in model-mean SST trends. (c) Relationship between SO and SEP SST trends across models, colored by global-mean SST trends. The solid line represents the least-squares fit. Dashed lines and the shaded area denote 95% confidence intervals from bootstrapping different ensemble members. The coefficient of determination (R^2) of this relationship is displayed in the title. Values in brackets represent the 2.5th percentile, mean, and 97.5th percentile of R^2 from bootstrapping different ensemble members. (d-f) As in (a-c), but SST trends are normalized by global-mean SST trends. Stippling in (e) indicates sdv. from bootstrapping exceeds 0.1. The thresholds of sdv. are subjectively selected for illustrative purposes.

the internal variability uncertainty. This indicates that models with a larger warming trend over the SEP also show a larger warming trend over SO. Coloring the scatter points by global-mean SST trends shows that models with larger SST trends over both SO and SEP regions also tend to have larger global-mean warming. Moreover, models overestimate the global-mean SST trend compared to observations (Figure 3.1c). These findings suggest that SO and SEP SST trends are closely related to global-mean SST trends, raising the question of whether the SO-SEP relationship arises because both regions are driven by the same factor—the global-mean warming. If this is the case, the model spread of global-mean warming would be embedded in the SO-SEP cross-model relationship, strengthening the relationship. Therefore, I analyze SST trends in the SO and SEP and their relationship with the effect of global-mean SST trends removed, normalizing local SST trends by dividing them by the global-mean SST trend in every model.

Normalizing local SST trends by the global-mean trend highlights regions of cooling and delayed warming (Figure 3.1d-e). The normalized delayed warming trends in the SEP and SO remain robust when accounting for the confidence interval of the internal variability uncertainty. Removing the global-mean trend has a stronger impact on the SEP SST trend than on the SO. Comparing normalized SST trends in the SO and SEP with their absolute SST trends (A.3), the inter-model variance of the normalized SO SST trend explained by the absolute SO SST trend is larger than that for SEP.

The normalized SST trends over the SO and SEP are positively related across models (Figure 3.1f): models with stronger delayed warming relative to the global-mean SST trend in the SO also simulate stronger delayed warming in the SEP. This positive relationship remains robust when accounting for internal variability. The reduced R^2 value of this relationship relative to the relationship between absolute SST trends (Figure 3.1c) indicates a strengthening effect of the global-mean SST trend on the SO-SEP relationship. Additionally, R^2 of the relationship between normalized SST trends is strongly affected by internal variability, ranging from no relationship to a relatively strong relationship comparable to those with global-mean warming (Figure 3.1c). This positive SO-SEP relationship is robust across five ensemble members within 26 models (A.2a), showing

that ensemble members with stronger SO SST trend due to changes in internal variability also have stronger SEP SST trend with the same internal variability. This internal variability-dominated positive relationship is consistent with the relationship between running 40-year SST trends in the Southern Ocean and eastern tropical Pacific identified in the Last Millennium Reanalysis (Dong et al., 2022). However, global-mean SST trends still play a role in such a relationship, as removing them reduces the robustness of its sign (A.2b).

ECS affects the relationship between absolute SST trends in the SO and SEP through its positive relationship with the global-mean SST trends across models (A.4a). Models with high ECS—the hot models—tend to simulate larger global-mean SST warming trends during the historical period (1985–2014) and show correspondingly larger SST trends over the SO and SEP. Are hot models also the ones with less delayed warming relative to global-mean warming in the SO and SEP? No. After normalizing local SST trends by global-mean trends, ECS has no relationship with the magnitude of normalized SST trends (not shown).

In this study, I do not disentangle the causal relationship between SST trends in the SO and SEP, and I acknowledge the effects of ENSO and tropical decadal variabilities that could induce a strong relationship from the tropics to the Southern Ocean (as reviewed in Li et al. (2021)). On the one hand, ENSO and its related teleconnections mainly occur on interannual timescales, making them part of the internal variability. I use bootstrapping analysis to assess the effect of internal variability on the SO-SEP relationship, which inherently captures the impact of ENSO and its related teleconnections on SST trends in both the SO and SEP. On the other hand, tropical decadal variabilities affect the SO on longer timescales (e.g., Meehl et al., 2016). These effects are removed along with global-mean SST trends, as the global-mean SST trend is largely driven by tropical SST trends (Jiang et al., 2025). In short, the effect of tropical interannual variability is included in the effect of internal variability assessed by bootstrapping analysis, and the effect of tropical decadal variability is removed through global-mean SST trend normalization. As a result, I attribute the remaining SO-SEP relationship in normalized SST trends primarily to the teleconnection from the SO to SEP.

3.4 Comparisons of Observed Shortwave Cloud Feedback and Ocean Heat Uptake with CMIP6 Model Simulations

The spatial pattern of the multi-model-mean shortwave cloud feedback in CMIP6 models generally matches the observations, while the strength of the shortwave cloud feedback along the west coast of South America is underestimated in models (Figure 3.2a-b). The model-mean shortwave cloud feedback in this region remains robustly positive when accounting for the effect of internal variability due to changes in models' initial condition. Positive shortwave cloud feedback indicates an amplifying effect on the local SST warming: as SST increases, stratocumulus cloud cover decreases, allowing more shortwave radiation to reach the surface and further enhancing SST warming. Averaging the shortwave cloud feedback over the west coast of South America (CF_{wSA}), the majority of ensembles members and models simulate a too weak CF_{wSA} compared to the range of observations calculated from different SST and radiation products (Figure 3.2c). In each model, the CF_{wSA} is less robust across different ensemble members, as the range of internal variability is model-dependent. Some models, such as MPI-ESM1-2-LR, can simulate a negative CF_{wSA} in some members. Other models, like CESM2-WACCM, show a robust, strong positive CF_{wSA} with a small uncertainty range. Expanding or shrinking the CF_{wSA} box by 5° in each direction does not affect my results.

Models simulate low ocean heat uptake variability off the west coast of South America, significantly lower than observed (Figure 3.2d–e). High ocean heat uptake variability in this upwelling region adds noise to SSTs, reducing the signal (in this case, trend)-to-noise ratio of local SST time-series and increasing the uncertainty of SST trends. Conversely, low ocean heat uptake variability in this region has less impact on the variability of local SST signals. Averaging the ocean heat uptake variability over the west coast of South America ($OHU_{wSA}\ sdv.$), the majority of models simulate a too weak $OHU_{wSA}\ sdv.$ as compared to the range of observational products (Figure 3.2f). Expanding or shrinking the $OHU_{wSA}\ sdv.$ box by 5° in each direction does not affect my results.

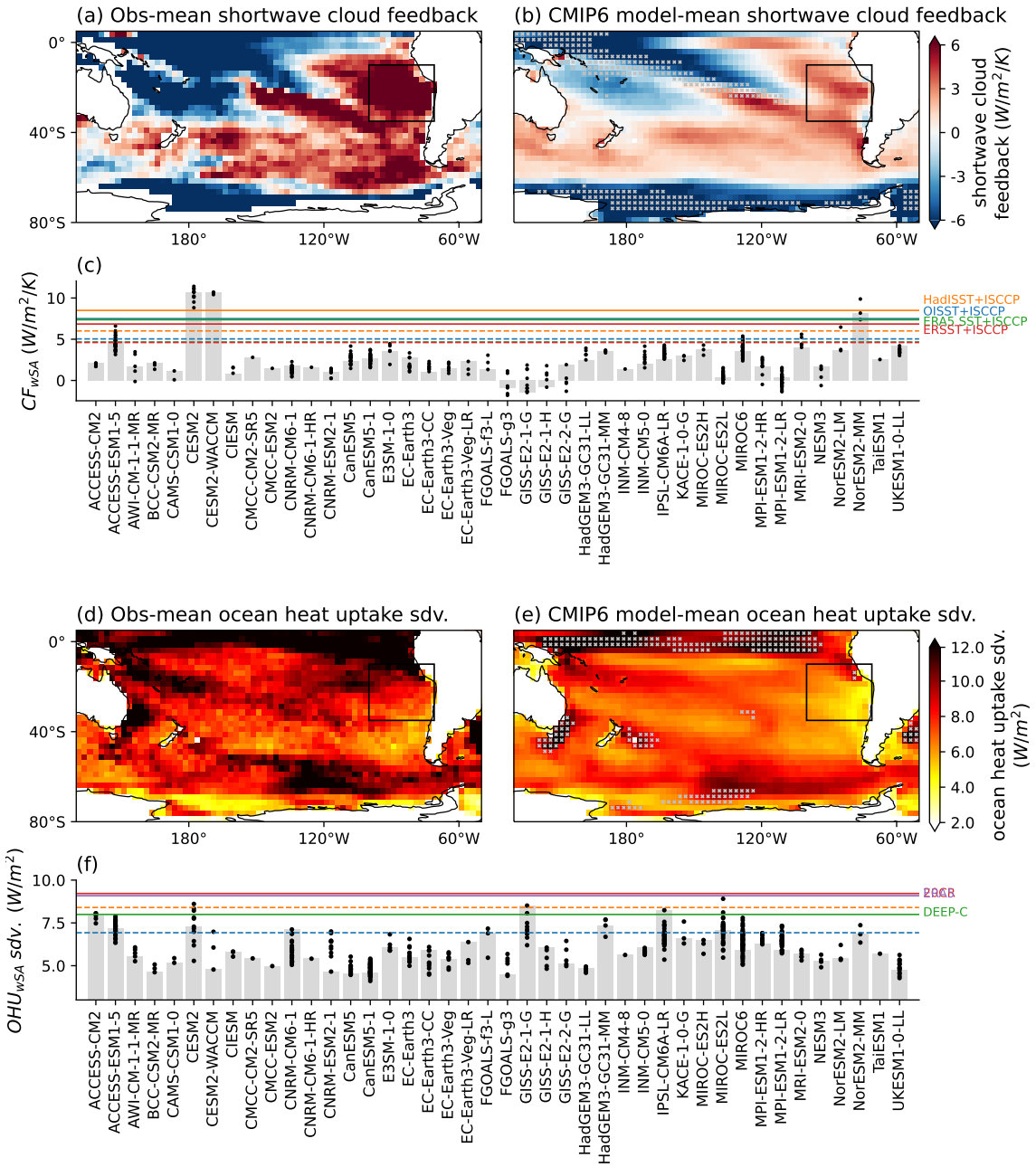

Figure 3.2: Overview of shortwave cloud feedback and ocean heat uptake variability in South Pacific. (a) Observed shortwave cloud feedback map. (b) Simulated shortwave cloud feedback map. Stippling indicates sdv. from bootstrapping exceeds 0.4 $W/m^2/K$. Averaging the shortwave cloud feedback over the west coast of South America (the black box in a and b), (c) shows the comparison of observed CF_{wSA} (solid colored lines) with those in the first ensemble member from models (grey bars). Black dots on each bar represent CF_{wSA} from each ensemble. Dashed colored lines represent CF_{wSA} calculated using the same SST observational products as the solid lines, but combined with CERES radiation data. Due to the differing temporal coverage of CERES (A.1), these dashed lines are included for informational purposes only. (d-f) As in (a-c), but shows ocean heat uptake variability over 1985-2014. The dashed orange and blue lines represent observed ocean heat uptake variability in the analyzed box from OAFlux and ECCO, respectively, with different temporal coverage (A.1). Stippling in (e) indicates sdv. from bootstrapping exceeds 0.2 W/m^2. The thresholds of sdv. are subjectively selected for illustrative purposes.

In addition to ocean heat uptake variability, I also tested other ocean heat uptake–related metrics that might have physical impacts on SST trends. Focusing on the same upwelling region off the west coast of South America, I first examined climatological ocean heat uptake, which acts as a thermal buffer: higher climatological ocean heat uptake suppresses local positive SST trends. However, its effect is associated with global-mean warming, complicating the physical interpretation of its role in the SO–SEP relationship. Furthermore, the observational range of this metric is too broad to provide a useful constraint in the next section; therefore, it is not shown in the main text. I also analyzed ocean heat uptake trends over 1985–2014. A positive trend has a stronger cooling effect on local SST trends over time. However, the sign of this trend varies widely across models and across observations, making it unsuitable for use as a constraint and therefore excluded from the main text. Both metrics are discussed in detail in Text A.1.

3.5 Opposing constraints of observed CF_{wSA} and OHU_{wSA} sdv. on SO-SEP relationship strength

In section 2, I show a robust positive cross-model relationship between SO and SEP SST trends. In section 3, I show that most models underestimated CF_{wSA} and OHU_{wSA} $sdv.$ relative to observations. Here, I further show the effects of CF_{wSA} and OHU_{wSA} $sdv.$ on the R^2 value of the cross-model relationship using different subsets of models, which leads to constraints on the strength of the cross-model SO-SEP relationship using observed CF_{wSA} and OHU_{wSA} $sdv.$.

The strength of the SO-SEP relationship is positively related to CF_{wSA}. Positive shortwave cloud feedback amplifies local SST variability and, since trends are included in the feedback calculation (Section 2.2), enhances SST trends. Models with larger CF_{wSA} values better preserve and amplify SST trends as they are advected from the SO to the SEP by the climatological wind, resulting in a stronger SO–SEP relationship across these high-CF_{wSA} models.

Grouping models by CF_{wSA}, I show that subsets of models with higher model mean CF_{wSA} values show stronger SO-SEP relationships, as indicated by larger R^2 values across models within these subsets (Figure 3.3a). The model mean CF_{wSA} values are not directly comparable to the

observations (represented by the thin vertical lines in Figure 3.3a), as the model-means smooth out internal variability and provide a cleaner estimate of the CF_{wSA} than individual observations.

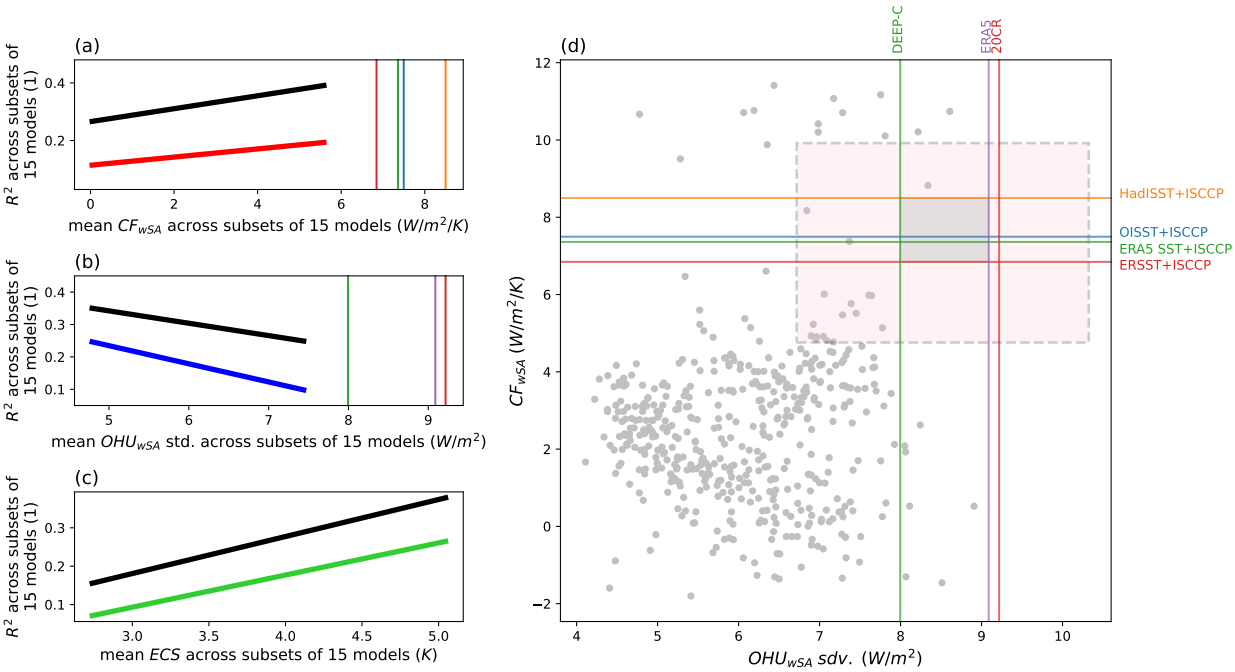

Figure 3.3: Constraints of SO-SEP relationship strength using (a) CF_{wSA}, (b) OHU_{wSA} sdv., and (c) ECS. The black lines represent the linear relationship between R^2 values between SO and SEP SST trend (as in Figure 3.1c) and CF_{wSA}, OHU_{wSA} sdv., and ECS. The red, blue, and green lines represent the linear relationship between R^2 values between normalized SO and SEP SST trend (as in Figure 3.1c) and CF_{wSA}, OHU_{wSA} sdv., and ECS, respectively. A detailed example of obtaining the black line in (a) is shown in A.5. The vertical lines in (a-b) represent observations, same as the solid lines in Figure 3.2c,f. (d) OHU_{wSA} sdv. versus CF_{wSA} for all ensemble members from 42 models (dots) and observations (lines). The grey-shaded area indicates the overlap between the observed ranges of OHU_{wSA} standard deviation and CF_{wSA}, while the pink-shaded area represents the overlap between their 95% confidence intervals. The confidence intervals were obtained from 5,000 bootstrap iterations by first resampling the temporal dimension—with replacement—at each grid point for SST, shortwave cloud radiative flux, and net surface heat flux, and then recalculating the shortwave cloud feedback and ocean heat uptake variability.

This positive dependence of the R^2 in the SO-SEP relationship on CF_{wSA} remains robust when addressing three concerns: sensitivity to subset size, the effect of internal variability, and the inclusion of global-mean SST trends in SO and SEP trends. First, a subset size of 15 models is chosen as a balance between smoother results (reducing the impact of internal variability, particularly from CF_{wSA}) and comparability with observations (as the model-mean of larger groups becomes less

comparable to individual observations). Changing the subset size between 5 and 35 models does not affect the positive dependence of R^2 on CF_{wSA}. Second, this positive dependence is based on not only the first ensemble member from each model, but is the linear fit of the R^2-CF_{wSA} relationship across all model subsets using different ensemble members in 5000 bootstrapping iterations (see illustrative example in A.5). As a result, the effect of internal variability is taken into account in such a positive dependence. Third, while the SO-SEP relationship using absolute SST trends generally has a higher R^2 (thick black line in Figure 3.3a) than using normalized SST trends (thick red line), the positive effect of CF_{wSA} on the SO-SEP relationship strength is independent of global-mean SST trends. The higher R^2 in SO-SEP relationship using absolute SST trends than using normalized SST trends is consistent with the findings discussed in Chapter 3, where the global-mean SST trend was shown to strengthen the SO-SEP relationship, as both regional SST trends are partially driven by the same factor—the global warming.

The strength of the SO–SEP relationship is negatively related to $OHU_{wSA}\ sdv.$. A larger $OHU_{wSA}\ sdv.$ increases local SST variability and adds noise to SST trends. Models with higher $OHU_{wSA}\ sdv.$ dilute more of the forced SST signal (i.e., the trend) with noise as the SST trend is advected from the SO to the SEP by the climatological wind, resulting in a weaker SO–SEP relationship across these high-$OHU_{wSA}\ sdv.$ models.

Grouping models by $OHU_{wSA}\ sdv.$, I find that subsets of models with larger $OHU_{wSA}\ sdv.$ values show weaker SO-SEP relationships (smaller R^2) (Figure 3.3b). This negative dependence remains robust when accounting for the effect of internal variability due to changes in models' initial condition, when changing the subset size between 5 and 35 models, and when including or excluding global-mean SST trends. Comparing the black and blue lines in Figure 3.3b, the differences in R^2 values between using absolute and normalized SST trends increase as $OHU_{wSA}\ sdv.$ values increase. In subsets of models with larger $OHU_{wSA}\ sdv.$, the global-mean SST trend plays a more important role in strengthening the SO–SEP relationship. Normalization of SST trends removes a major component of the forced signal—the global-mean trend—thereby reducing their signal-to-noise ratio. As a result, normalized SST trends are more vulnerable to the noise intro-

duced by $OHU_{wSA}\ sdv.$ than absolute trends, with the difference becoming more pronounced as $OHU_{wSA}\ sdv.$ increases.

The opposing effects of CF_{wSA} and $OHU_{wSA}\ sdv.$ on the SO-SEP relationship lead to conflicting constraints of observed CF_{wSA} and $OHU_{wSA}\ sdv.$ on the simulated strength of the SO-SEP relationship. If models simulated stronger CF_{wSA} as observed, the SO–SEP relationship would be stronger; if they simulated stronger $OHU_{wSA}\ sdv.$, the relationship would be weaker. This raises a natural question: which effect dominates?

Before addressing this question, I first examine whether there is a cross-model relationship between CF_{wSA} and $OHU_{wSA}\ sdv.$. By showing all the ensemble members and models in Figure 3.3d, no apparent relationship between these two variables is detected, suggesting that their effects on the cross-model SO-SEP relationship can be considered independently.

Then, to determine which process dominates the SO–SEP relationship (CF_{wSA} or $OHU_{wSA}\ sdv.$), I assess whether any models fall within the observational ranges for both variables, with implications for a more realistic SO-SEP relationship than other models. Most models and ensembles cluster in the lower-left corner of the plot, where the constraint effects of CF_{wSA} and $OHU_{wSA}\ sdv.$ oppose each other. Comparing these two variables to their observations, I show that no ensemble member or model simulates both CF_{wSA} and $OHU_{wSA}\ sdv.$ within the observational range (i.e., the grey-shaded area; Figure 3.3d). However, several ensemble members from ACCESS-ESM1-5, CESM2, and NorESM2-MM fall within the 95% confidence interval of the observations (i.e., the pink-shaded area), indicating a more realistic SO-SEP relationship across these models. According to Figure 3.2c, these three models are among the top five in simulating high CF_{wSA}, but they do not consistently rank among the top five for $OHU_{wSA}\ sdv.$ (Figure 3.2). Therefore, CF_{wSA} dominates the SO–SEP relationship, with accurate simulation of CF_{wSA}—closer to observations—contributing more than that of $OHU_{wSA}\ sdv.$.

The SO-SEP relationship constraints for individual models can be inferred from Figure 3.3d. For example, CESM2 overestimates CF_{wSA} while simulating $OHU_{wSA}\ sdv.$ within the observational range. Based on Figure 3.3a-b, CESM2 likely overestimates the strength of SO-SEP rela-

tionship due to its excessively strong CF_{wSA}. Another example is HadGEM3-GC31-LL, which simulates CF_{wSA} close to observations but underestimates OHU_{wSA} $sdv.$. According to the effects of CF_{wSA} and OHU_{wSA} $sdv.$, HadGEM3-GC31-LL might also overestimate the strength of SO-SEP relationship but due to its erroneously weak OHU_{wSA} $sdv.$.

The strength of the SO–SEP relationship is positively related to ECS, driven in part by a positive relationship between ECS and shortwave cloud feedback (Zelinka et al., 2020). Models with higher CF_{wSA} tend to also simulate higher ECS (A.4b), resulting in a larger amplifying effect of the positive CF_{wSA} on local SST trends and leading to a stronger relationship between SST trends in the SO and SEP. Grouping models by ECS, I find that subsets with larger ECS have a stronger SO-SEP relationship (larger R^2) (Figure 3.3c). This positive dependence of R^2 in cross-model SO-SEP relationship on ECS aligns with the speculations of Kang et al. (2023a), suggesting a larger ECS when the simulated SO-SEP relationships in climate models are strengthened. This positive dependence remains robust when accounting for the effect of internal variability due to changes in models' initial condition, when changing the subset size between 5 and 30 models, and when including or excluding global-mean SST trends.

3.6 Summary and Discussion

I analyze the SST trends in the Southern Ocean and southeastern tropical Pacific and their cross-model relationship using CMIP6 historical simulations over 1985-2014. Most models fail to capture the observed cooling trends in both regions, instead showing delayed warming trends. By using historical simulations rather than conducting perturbation experiments, I avoid applying unrealistically large forcing to the climate system and focus on the "real world" regime.

The delayed warming trends in the Southern Ocean and southeastern tropical Pacific are related across models, largely attributed to global-mean SST trends. Removing global-mean SST trends weakens the relationship, suggesting that global-mean warming needs to be taken into account when analyzing teleconnections in a forced climate—particularly in perturbation experiments where global-mean temperature can be affected.

I evaluate two key physical drivers in the relationship between the Southern Ocean and the southeastern tropical Pacific: shortwave cloud feedback and ocean heat uptake variability off the west coast of South America. Shortwave cloud feedback poses a positive influence on the relationship: models with stronger cloud feedback amplify local SST signals, helping to preserve SST trends advected from the Southern Ocean to the southeastern tropical Pacific, thereby strengthening the relationship between these two regions. In contrast, ocean heat uptake variability has a negative effect: models with larger variability introduce more noise into local SST variability, adding noise to the advected SST trends and weakening the relationship between the two regions. Most models underestimate both factors, leading to opposing observational constraints: strengthening the simulated cloud feedback enhances the Southern Ocean-southeastern tropical Pacific relationship, whereas increasing the simulated ocean heat uptake variability weakens it. Based on the models that simulate cloud feedback and ocean heat uptake variability closest to observations, strengthening cloud feedback contributes more to a realistic Southern Ocean–southeastern tropical Pacific relationship than strengthening ocean heat uptake variability.

I also link the Southern Ocean-southeastern tropical Pacific relationship to ECS, with implications for the hot model problem. ECS is positively related to shortwave cloud feedback off the west coast of South America. Given the strengthening effect of cloud feedback on the Southern Ocean-southeastern tropical Pacific relationship, models with higher ECS tend to simulate a stronger cross-model relationship between SST trends in these two regions.

My findings come with caveats. First, while the cross-model relationship supports the role of shortwave cloud feedback in the Southern Ocean-southeastern tropical Pacific relationship, as tested in perturbation experiments (e.g., Kim et al., 2022), it may not fully explain the effect of ocean heat uptake variability. Targeted perturbation experiments in individual models remain necessary to clarify the role of ocean heat uptake in this relationship. Second, I have not analyzed the role of trend magnitude in the relationship between the Southern Ocean and the southeastern tropical Pacific. Do models with larger SST trends in both regions have stronger cross-model relationship? I speculate an affirmative answer based on the relationship between the local SST

trend, the global-mean SST trends, and ECS. However, whether trend magnitude is linked to shortwave cloud feedback and ocean heat uptake off the west coast of South America remains an open question for future research. Finally, observations are problematic, particularly for ocean heat uptake off the west coast of South America. To provide more reliable constraints and to better understand the joint effects of shortwave cloud feedback and ocean heat uptake on the Southern Ocean-southeastern tropical Pacific relationship, longer and more reliable observational products are needed.

CHAPTER 4 CONSTRAINING THE RELATIONSHIPS BETWEEN SEA SURFACE TEMPERATURE IN THE SOUTHERN OCEAN AND SOUTHEASTERN TROPICAL PACIFIC ON INTERANNUAL TIMESCALE

4.1 Introduction

The impacts of tropical teleconnections on the Antarctic climate are well studied. Li et al. (2021) reviewed the mechanisms of teleconnections of tropical climate variabilities to Antarctic climates. On interannual timescales, variations in surface warming and sea ice extent in Antarctica are influenced to the first order by the El Niño-Southern Oscillation (ENSO) via stationary Rossby waves and Hadley cell variations. On decadal timescale, variations in the Amundsen Sea Low and sea ice extent near Antarctica are affected by the Interdecadal Pacific Oscillation (Meehl et al., 2016).

The Southern Ocean climate also affects the tropical climate. Hwang and Frierson (2013) first identified a teleconnection from the Southern Ocean to the tropics in the Coupled Model Intercomparison Project phase 5 (CMIP), showing that models with larger shortwave cloud radiative forcing biases over the Southern Ocean have stronger double-Intertropical Convergence Zone (ITCZ) biases. Subsequent studies have tested how thermal changes in the Southern Ocean sea surface temperature (SST) influence SST in the southeastern tropical Pacific by perturbing models of varying complexity. In atmospheric models coupled to a slab ocean, cooling of the Southern Ocean induced by various perturbations leads to decreased SST over the southeastern tropical Pacific (e.g., Hwang et al., 2017; Kang et al., 2018a,b; Dong et al., 2022), while warming of the Southern Ocean, imposed through weakened ocean heat uptake, results in increased SST over the southeastern tropical Pacific (Lin et al., 2021). In fully coupled climate models, southeastern tropical Pacific cooling has similarly been attributed to Southern Ocean cooling (Kim et al., 2022; Mechoso et al., 2016; Kang et al., 2020; Zhang et al., 2021; Kang et al., 2023a), and warming over the southeastern tropical Pacific is seen in response to increased shortwave radiation over the Southern Ocean (Yu and Pritchard, 2019). Extending beyond idealized perturbation experiments,

this teleconnection from the Southern Ocean to the southeastern tropical Pacific is evident in both forced and unforced coupled climate model outputs (Chapter 2), and has been invoked to explain the observed cooling trends in both regions (Hartmann, 2022; Kang et al., 2023b).

The subtropical stratocumulus cloud feedback and ocean heat uptake are key factors influencing the strength of the relationship between the Southern Ocean and the southeastern tropical Pacific. Kim et al. (2022) proposed a pathway for the Southern Ocean teleconnection to the tropical Pacific after cooling the Southern Ocean in eight fully coupled models. As the Southern Ocean cools, cold SST anomalies are advected equatorward by climatological southeasterlies. On the way to the tropics, the cold anomalies are amplified by three processes: enhanced oceanic upwelling and a positive stratocumulus-SST feedback off the west coast of South America, and a strengthened wind-evaporation-SST (WES) feedback over the southeastern tropical Pacific. Among these factors, positive stratocumulus cloud feedback was identified as the primary driver of relationship strength, with models having stronger cloud feedback showing a greater cooling response in the southeastern tropical Pacific under the same Southern Ocean perturbation. Chapter 2 of this dissertation examined the effects of these physical factors on interannual timescales, using model outputs from pre-industrial control simulations and forced simulations with an abrupt quadrupling of CO_2 across Coupled Model Intercomparison Project Phase 6 (CMIP6) models. My findings confirmed the key role of subtropical stratocumulus cloud feedback while also revealing the equally important role of ocean heat uptake in the upwelling region, showing that models with stronger stratocumulus cloud feedback and weaker ocean heat uptake have stronger interannual SST correlations between the Southern Ocean and the southeastern tropical Pacific.

Given the effect of the shortwave cloud feedback and ocean heat uptake on the Southern Ocean-southeastern tropical Pacific relationship, I attempted to constrain the simulated cross-model relationship strength between SST trends in the two regions using observed cloud feedback and observed ocean heat uptake variability (Chapter 3). These two physical factors show opposing constraint effects on the Southern Ocean-southeastern tropical Pacific relationship, suggesting that strengthening the shortwave cloud feedback in climate models tends to enhance the relation-

ship, while strengthening the ocean heat uptake variability off the west coast of South America tends to weaken it. I assess the relationship between 30-year SST trend—i.e., a decadal-scale relationship—across CMIP6 models, rather than within individual models. As such a relationship cannot be measured from individual observations, the strength of this cross-model relationship cannot be directly comparable to observations. Therefore, although I can use observed shortwave cloud feedback and ocean heat uptake to constrain the strength of the Southern Ocean-southeastern tropical Pacific relationship, I cannot determine which factor plays the dominant role, nor can I conclusively identify how the relationship should be improved in climate model simulations.

In this chapter, I measure the relationship between the Southern Ocean and the southeastern tropical Pacific on the interannual timescale within each model, using lag-0 correlations, and I constrain the simulated correlation strength by observed cloud feedback and ocean heat uptake. The correlation measures the instantaneous relationship between the two regions, and I acknowledge the effect of tropical variability—such as ENSO and tropical decadal variability—that may link these two regions through tropical teleconnections to the Southern Ocean. To account for this, I also test the robustness of the Southern Ocean-southeastern tropical Pacific relationship and the constraint effects of cloud feedback and ocean heat uptake after removing ENSO and decadal variability. I introduce the analyzed models and variables in Section 4.2. I analyze the strength of the Southern Ocean-southeastern tropical Pacific relationship and examine the constraining effects of observed shortwave cloud feedback and ocean heat uptake variability in Section 4.3. I discuss the implications of my findings and summarize the results in Section 4.4.

4.2 Data and Methods

4.2.1 Reanalyses, observations, and climate models

I analyze observed SST trends from the fifth generation ECMWF atmospheric reanalysis of the global climate (ERA5) (Hersbach et al., 2023), the Extended Reconstructed SST dataset v5 (ERSSTv5) (Huang et al., 2017), the Hadley Centre Sea Ice and Sea Surface Temperature dataset (HadISST 1.1) (Rayner et al., 2003), and the Optimum Interpolation Sea Surface Temperature dataset (OISST v2.1) (Huang et al., 2021). To calculate stratocumulus cloud feedback, I use

the SST products listed above alongside shortwave radiation fluxes at top-of-atmosphere from the International Satellite Cloud Climatology Project radiative flux profile product (ISCCP-FH) (Zhang and Rossow, 2023). Ocean heat uptake is analyzed using surface radiation fluxes from the ERA5 (Hersbach et al., 2023), the Diagnosing Earth's Energy Pathways in the Climate system dataset (DEEP-C) (Liu and Allan, 2022), and the NOAA-CIRES-DOE Twentieth Century Reanalysis Project version 3 (20CR) (Slivinski et al., 2019). I use annual data from 1985 to 2014 for all observations and reanalyses to remove monthly variabilities, which are likely associated with El Niño–Southern Oscillation (ENSO) and its strong teleconnection to the Southern Ocean (e.g., Yuan, 2004; Li et al., 2021). All datasets are linearly interpolated to a $2.5°\times 2.5°$ spatial resolution.

Table 4.1: CMIP6 historical simulations covering the period 1985-2014, with at least 5 ensemble members available.

Model	Reference	Model	Reference
ACCESS-CM2	Dix et al. (2019)	GISS-E2-1-G	NASA/GISS (2018a)
ACCESS-ESM1-5	Dix et al. (2019)	GISS-E2-1-H	NASA/GISS (2018b)
AWI-CM-1-1-MR	Semmler et al. (2018)	GISS-E2-2-G	NASA/GISS (2019a)
CESM2	Danabasoglu (2019b)	HadGEM3-GC31-LL	Ridley et al. (2018)
CNRM-CM6-1	Voldoire (2018)	INM-CM5-0	Volodin et al. (2019b)
CNRM-ESM2-1	Seferian (2018)	IPSL-CM6A-LR	Boucher et al. (2018)
CanESM5	Swart et al. (2019a)	MIROC-ES2L	Hajima et al. (2019b)
CanESM5-1	Swart et al. (2019b)	MIROC6	Tatebe and Watanabe (2018)
E3SM-1-0	Bader et al. (2019)	MPI-ESM1-2-HR	Jungclaus et al. (2019)
EC-Earth3	EC-Earth (2019a)	MPI-ESM1-2-LR	Wieners et al. (2019)
EC-Earth3-CC	EC-Earth (2020a)	MRI-ESM2-0	Yukimoto et al. (2019)
EC-Earth3-Veg	EC-Earth (2019b)	NESM3	Cao and Wang (2019)
FGOALS-g3	Li (2019)	UKESM1-0-LL	Tang et al. (2019)

I analyze simulated SST, top-of-atmosphere shortwave radiation fluxes, and surface radiation fluxes from historical simulations over the same 30-year period across 26 CMIP6 models, each with at least five available ensemble members (Table 4.1). I use five ensemble members per model to assess the roles of the forced response and internal variability in shaping the relationship between the Southern Ocean and the southeastern tropical Pacific (see details in the next subsection). This number of ensemble members is chosen to balance a relatively clean estimate of the forced

response with a sufficiently large model size for comparison. Similar to the observational data, I use annual means and re-grid all model outputs to a 2.5°x 2.5° resolution.

4.2.2 Methods

I measure the relationship between the Southern Ocean and the southeastern tropical Pacific on interannual timescales by calculating correlations between their SST timeseries over 1985-2014. The interannual correlations are first calculated for each ensemble member in every model, including the influence of both the forced response and internal variability. To isolate the effect of internal variability, I then subtract the ensemble mean from each ensemble member, eliminating the forced response from the SST timeseries, and recalculate the interannual correlations using ensemble anomalies in every model. In this study, I show results primarily based on the first of the selected five ensemble members from each CMIP6 model, while also estimating the uncertainty range of the internal variability due to changes in models' initial condition through bootstrapping analysis.

I apply bootstrapping analysis to the fixed set of five ensemble members from each model, resampling ensemble members over 5000 iterations. The bootstrapping analysis is used in the constraint-focused part of this study (Figure 4.3), which involves cross-model regression analyses. In this context, the impact of internal variability on the constraining effects of observed shortwave cloud feedback and ocean heat uptake variability on the simulated Southern Ocean–southeastern tropical Pacific correlations is assessed by the 95% confidence intervals of the bootstrapped results. For interannual correlations with ENSO-related variability and tropical decadal variability removed, the bootstrapping is applied after the removal step.

I calculate shortwave cloud feedback by regressing local shortwave cloud radiation flux against local SST over the 30-year period from 1985 to 2014 in observations and 26 CMIP6 models. Shortwave cloud radiation flux is computed by subtracting the clear-sky outgoing shortwave radiation flux at the top-of-atmosphere from the total outgoing shortwave radiation flux at the top-of-atmosphere (downward positive). Both the shortwave cloud radiation flux and SST timeseries are detrended before linear regression. The spatial patterns of the shortwave cloud feedback in obser-

vations and CMIP6 models are shown in Figure 3.2 and discussed in Chapter 3. As in Chapters 2 and 3, I calculate the regional average of shortwave cloud feedback off the west coast of South America (CF_{wSA}) for each ensemble member in every model, using the same regional box. When assessing the uncertainty of internal variability in the constraining effect of observed CF_{wSA} on correlations between the Southern Ocean and the southeastern tropical Pacific, CF_{wSA} values from different ensemble members are resampled along with the corresponding interannual correlations.

I calculate the net surface heat flux to quantify the ocean heat uptake (downward positive) in observations and CMIP6 models. I investigate the role of ocean heat uptake in the interannual correlation between the Southern Ocean and the southeastern tropical Pacific by analyzing ocean heat uptake variability, which is defined as the standard deviation of ocean heat uptake over time. The 30-year trend of the ocean heat uptake is removed from the timeseries prior to the calculation of variability. In the upwelling region of interest, the forced trend in ocean heat uptake is smaller than its interannual variability in 23 out of 26 models (not shown). As a result, whether or not the trend is removed before calculating the standard deviation does not affect my results. Similar to CF_{wSA}, I calculate the regional average of ocean heat uptake variability over the west coast of South America ($OHU_{wSA}\ sdv.$) for each ensemble member in every model as in Chapter 3. I assess the uncertainty due to internal variability in its constraining effect on the Southern Ocean-southeastern tropical Pacific correlations through the same bootstrapping procedure as in CF_{wSA}.

To assess the effect of ENSO-related variability on the interannual correlation between the Southern Ocean and the southeastern tropical Pacific, I regress the SSTs averaged over the Niño 3.4 region (5°S-5°N, 170°W-120°W) out of the SSTs in both the Southern Ocean and the southeastern tropical Pacific before calculating the correlations. To examine the effect of tropical decadal variability on this interannual correlation, I apply a 10-year high-pass filter to the SSTs at every grid point before calculating correlations.

4.3 Results

4.3.1 Interannual relationship between the Southern Ocean and the southeastern tropical Pacific

In observations, the Southern Ocean and the southeastern tropical regions are positively correlated. Correlating all grid points in the South Pacific to the SST averaged over the southeastern tropical Pacific triangle (hereinafter SEP; Fig. 4.1a) and the Southern Ocean box (hereinafter SO; Fig. 4.1b) reveals a clear horseshoe pattern of statistically significant positive correlations connecting the two regions, consistent with the correlation map shown in Dong et al. (2022). The Southern Ocean box is chosen for its strongest correlation with the SEP region, for comparability with the results in Chapter 3 and with Dong et al. (2022). Expanding the Southern Ocean box to the entire Pacific sector does not quantitatively affect the results. The southeastern tropical Pacific triangle is chosen based on its strong covariation with the SO SST. Although this covariation extends toward the equator, I focus on the southeastern tropical Pacific because the SST trend (see Chapter 3) and SST response to external forcing (see Chapter 2) are most pronounced in this region. Extending the triangle into the equatorial region or expanding or shrinking it by 5° in each direction does not quantitatively change my results.

In historical simulations, SO and SEP are positively correlated. The horseshoe pattern of positive correlation remains evident and is consistent with observations (Fig. 4.1c-d). This correlation is first calculated for each ensemble member, then averaged across fixed sets of five ensemble members in each model, and finally averaged across models. As a result, this correlation accounts for both the forces response—represented by the ensemble mean of each model—and internal variability in SST timeseries at each grid point. One might ask, is the positive correlation between SO and SEP SST mainly attributed to their forced response?

The answer is no. Removing the ensemble mean prior to calculating the correlations does not significantly reduce the correlations between SO and SEP (Fig. 4.1e-f). This indicates that the interannual correlation between these two regions is mainly attributed to their interannual variability. This result is expected, as Chapter 3 shows that these regions have relatively weak SST trends (i.e.,

a weak forced response) compared to other regions, removing which would not significantly affect the interannual correlations.

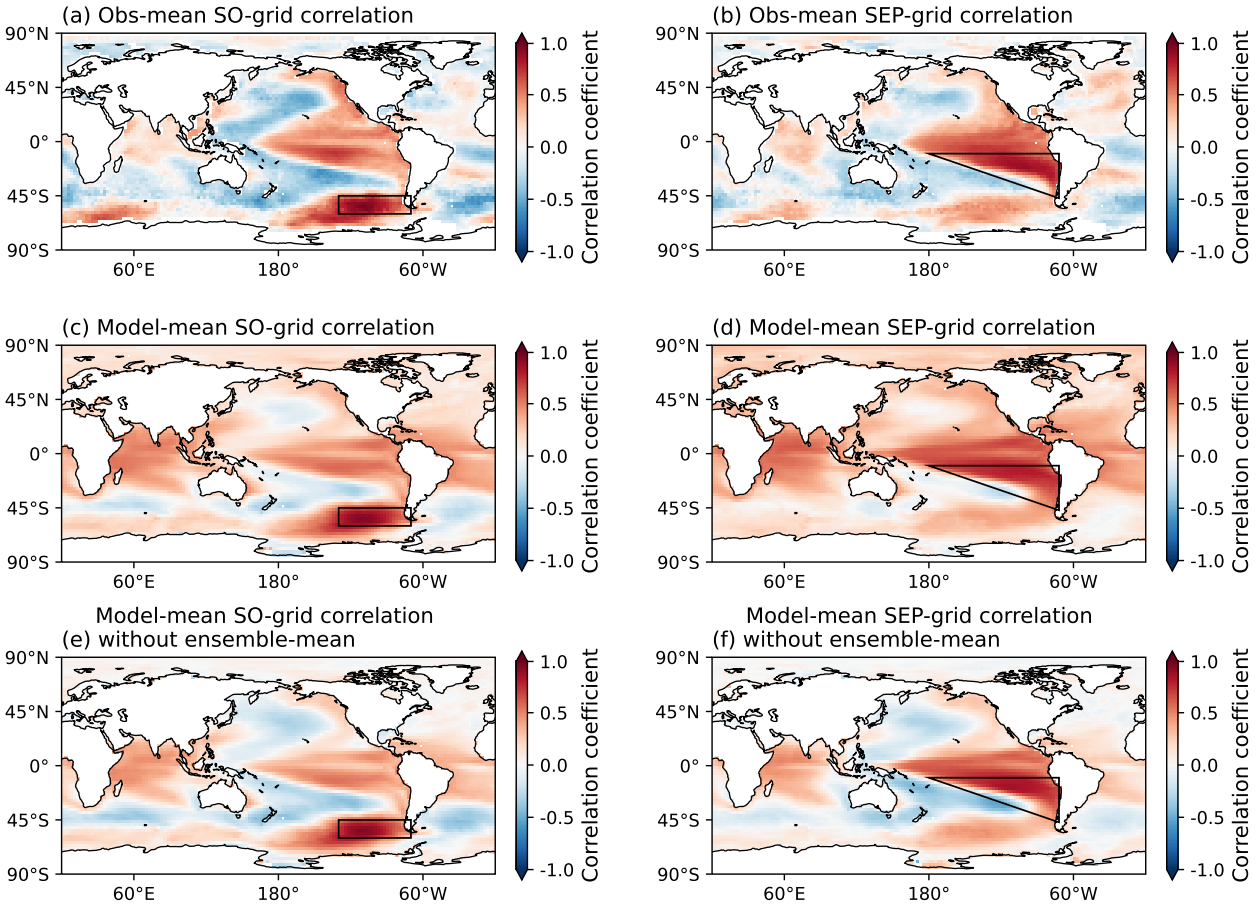

Figure 4.1: Correlation maps from observations and historical climate model simulations. (a) Observed correlations between annual SST at each grid point and the area-weighted average of the SO SST, averaged across four observational products. The black box represents the Pacific sector of the Southern Ocean analyzed in this study. (b) As in (a), but for correlations with the area-weighted average of the SEP SST. The black triangle marks the southeastern tropical Pacific area analyzed in this study. (c–d) Same as (a–b), but showing simulated correlations averaged across 26 CMIP6 models, including the forced response (i.e., the ensemble mean) in the SST timeseries for correlations. (e–f) As in (c–d), but with the forced response removed from each ensemble prior to calculating correlations.

In addition to the contribution from the forced response, the interannual correlation between SO and SEP SSTs may also be influenced by tropical variabilities such as ENSO-related teleconnections and tropical decadal variability (e.g., Yuan, 2004; Schneider and Deser, 2018; Meehl et al., 2016). I begin by focusing on the multi-model mean correlations. On the one hand, remov-

ing ENSO-related variability from SO and SEP SSTs leads to a decrease in the multi-model mean SO–SEP correlation (Fig. 4.2). This reduction reflects not only the removal of ENSO-related internal variability but also the removal of the tropical forced response, since the ensemble mean is included at every grid point during the regressions. The impact of the tropical forced response on SO–SEP correlations appears weaker than that of the local forced response in SO and SEP. This is evident from the larger reduction seen in the fifth correlation (from left to right in Fig. 4.2), where both local forced response and ENSO-related variability are removed, compared to the second correlation, which only removes the tropical forced response and ENSO-related variability. Comparing the fourth and fifth correlations also shows that the ENSO-related variability has a stronger effect on SO–SEP correlations than the local forced response.

On the other hand, applying a 10-year high-pass filter to the SO and SEP SSTs also reduces the multi-model mean SO–SEP correlation, although to a small extent. This change is comparable to the effect of removing the local forced response, as shown by the similarity between the third and fourth correlations in Fig. 4.2. This result is expected, since the forced response—calculated by averaging ensemble members that smooth out parts of internal variability of the climate system—primarily reflects variability on longer timescales (e.g., decadal variability), which overlaps with the low-frequency signals removed by the high-pass filter. Nevertheless, the forced response and low-frequency internal variability are not the same. This is shown by the slightly larger reduction in the last correlation (Fig. 4.2), where both the forced response and low-frequency variability are removed, compared to removing either one individually.

In summary, among the three components—local forced response, ENSO-related variability, and tropical decadal variability—ENSO-related variability has the strongest impact on the SO–SEP correlation, while the other two have comparable but smaller effects. But overall, changes in the multi-model mean correlation are small, indicating that the positive correlation between SO and SEP SSTs is robust and not solely driven by tropical variability or its related teleconnections.

However, the spread across models is large and spans zero. In Fig. 4.2, the second correlation (from left to right) shows that when the local forced response is included, the model spread in-

creases after removing ENSO, suggesting that in some models, the positive SO–SEP correlation is largely driven by ENSO-related variability. Removing this part of internal variability—along with the associated tropical forced response—reduced the SO–SEP correlation. A similar result is seen when the local forced response is excluded, as shown by the fifth correlation in Fig. 4.2. The third correlation shows that applying a 10-year high-pass filter reduces the model spread, indicating that strong positive SO–SEP correlations in most models are primarily driven by internal variability on interannual timescales. The fourth correlation, which removes the forced response (i.e., the ensemble mean), results in a similarly reduced spread. However, the combined removal of both the forced response and low-frequency variability leads to an increased model spread, suggesting that in some models, the positive correlation is driven by both low-frequency variability and the forced response.

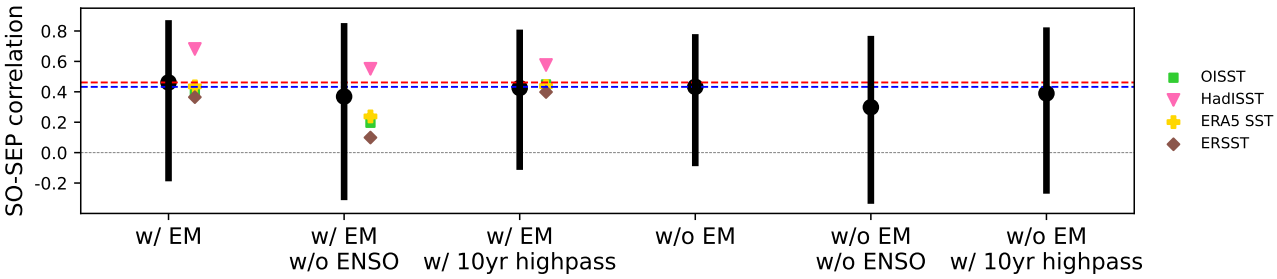

Figure 4.2: Correlation coefficients between annual SST timeseries in SO and SEP. From left to right, the first correlation is calculated between 30-year annual SSTs over the SO and SEP in the first ensemble member (including the ensemble mean) in each model. The second and third correlations are calculated in the same way as the first, but with the second excluding ENSO variability and the third applying a 10-year high-pass filter to the SST time series, respectively. The fourth through the last correlations mirror the first three but exclude the ensemble mean (EM) from each ensemble prior to calculating the correlations. Black circles represent the multi-model mean of the correlations, and black lines represent the model spreads. The red dashed line marks the model-mean SO-SEP correlation including the ensemble mean (equal to the first black circle), and the blue dashed line marks the model-mean correlation excluding the ensemble mean (equal to the fourth black circle). Correlations from four observational products are included for comparison with the simulated correlations that include the ensemble mean. The grey dashed line marks where the correlation coefficient equals zero.

Observations fall within the range of simulated SO–SEP correlations but also show a relatively large spread. HadISST stands out as an outlier, consistently showing the highest correlation among

all observational products and lying near the upper edge of the simulated range, while the other three observational products cluster below the CMIP6 multi-model mean. Based on the changes in observed SO–SEP correlations after removing ENSO-related variability and tropical decadal variability, the SO–SEP correlation in HadISST appears to be less influenced by both variabilities than other observational products. Given the spread across observational datasets and how they respond to the removal of ENSO and decadal variability, it remains uncertain whether the SO–SEP relationships in climate models are underestimated or overestimated. To provide further insight, I examine the role of two physical factors—shortwave cloud feedback and ocean heat uptake variability—in constraining the SO–SEP relationship.

4.3.2 Constraining interannual correlations between the Southern Ocean and the southeastern tropical Pacific in CMIP6 models

Models with larger SO–SEP correlations that include the forced response simulate higher CF_{wSA} values (Fig. 4.3a). Positive shortwave cloud feedback poses an amplifying effect on the local SST variability: as SST increases, stratocumulus cloud cover decreases, allowing more shortwave radiation to reach the surface and further enhancing SST warming. Models with larger CF_{wSA} values better preserve and amplify SST variability as they are advected from the SO to the SEP by the climatological wind, resulting in a larger SO–SEP correlation. The coefficient of determination (R^2) for this cross-model relationship is small, with large uncertainty due to internal variability arising from changes in models' initial condition, as indicated by the confidence intervals from bootstrapping. When including the observed CF_{wSA}, it is shown that most models tend to underestimate CF_{wSA}. The positive relationship between SO–SEP correlations and CF_{wSA} suggests that most models also tend to underestimate the SO–SEP correlation strength, which is consistent with the comparison between observed and simulated SO–SEP correlations (Fig. 4.3a).

Models with larger SO–SEP correlations that include the forced response tend to have smaller OHU_{wSA} $sdv.$ values (Fig. 4.3b). A large OHU_{wSA} $sdv.$ adds noises to local SST variability. Models with smaller OHU_{wSA} $sdv.$ better preserve SST variability advected from the SO to the SEP by the climatological wind, resulting in a stronger SO–SEP correlation. The R^2 of

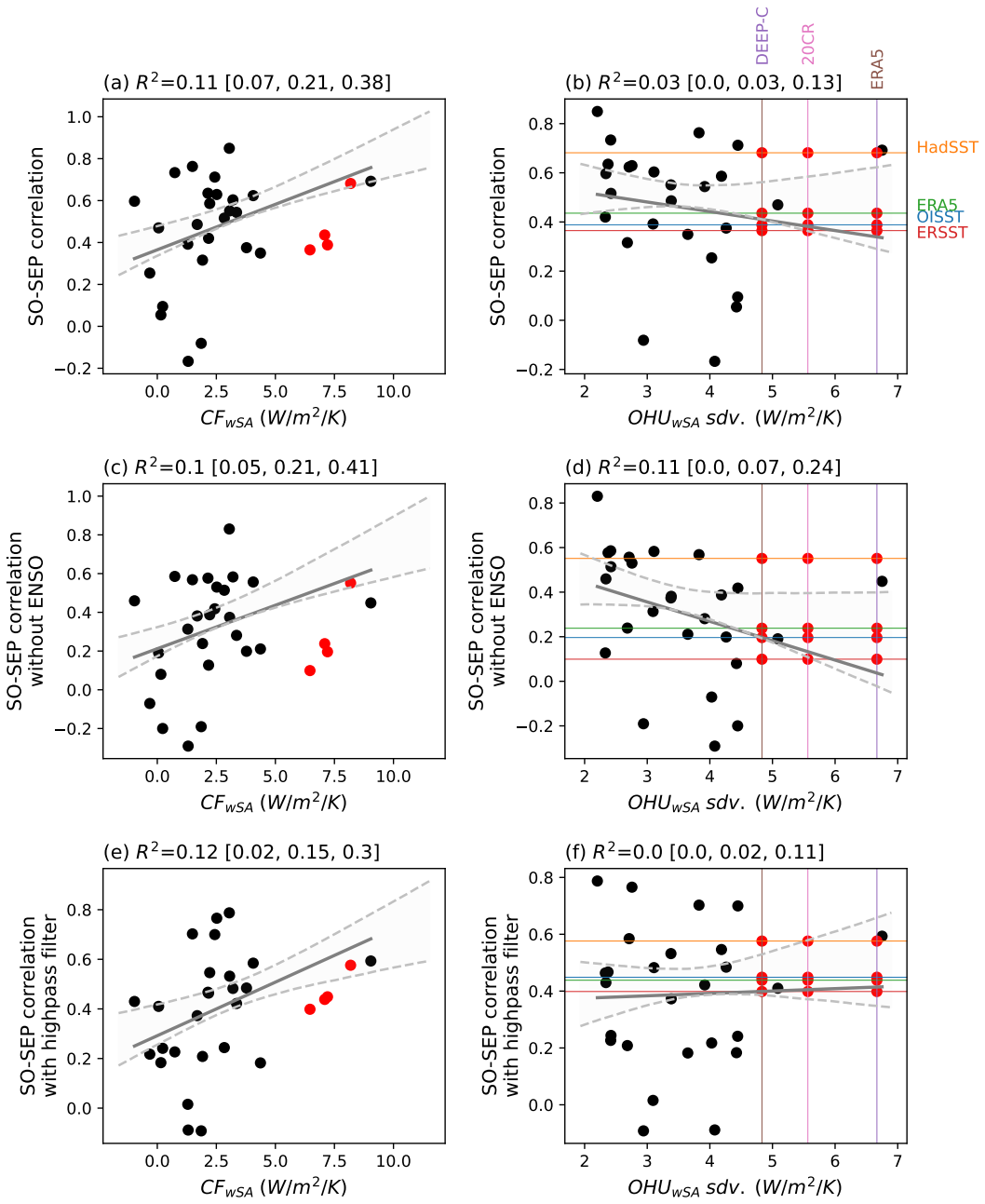

Figure 4.3: Constraints from observed CF_{wSA} and OHU_{wSA} $sdv.$ on simulated SO-SEP correlations with forced response included. (a) Relationship between CF_{wSA} and SO-SEP correlation across CMIP6 models. Black circles represent the first ensemble member from individual models, and red circles represent observations. The grey line shows the least-squares fit to black circles. Dashed lines and the shaded area denote 5%-95% confidence intervals from bootstrapping different ensemble members. The coefficient of determination (R^2) of this relationship is displayed in the title. Values in brackets represent the 5th percentile, mean, and 95th percentile of R^2 from bootstrapping different ensemble members. (b) Same as (a), but showing the cross-model relationship between OHU_{wSA} $sdv.$ and SO-SEP correlation. Vertical lines represent OHU_{wSA} reanalyses, and horizontal lines are reanalysis-based SO-SEP correlations. Red circles represent different combinations of SST and OHU_{wSA} reanalyses products. (c-d) Same as (a-b), but using SO-SEP correlations with ENSO variability removed. (e-f) As in (a-b), but using SO-SEP correlations with a 10-year highpass filter applied.

this relationship is generally lower than that between CF_{wSA} and SO–SEP correlation, revealing a secondary role of OHU_{wSA} $sdv.$ in influencing SO–SEP correlations. Despite this negative relationship, both OHU_{wSA} $sdv.$ and SO–SEP correlations are underestimated in climate models relative to observations.

This raises two hypotheses: First, if the negative relationship also holds in observations, then the key issue would be to correct the underestimation of both OHU_{wSA} $sdv.$ and SO–SEP correlations in models. However, this hypothesis is difficult to test due to the limited availability of observational ocean heat uptake products, which often lack corresponding SST data, making regression analysis infeasible. Second, the negative relationship across models may be questionable given the low R^2 value, with the mechanisms by which OHU_{wSA} $sdv.$ affects SO–SEP correlations likely vary across models and warrant further investigation. Notably, when replacing OHU_{wSA} $sdv.$ with other ocean heat uptake–related metrics—such as the climatological OHU_{wSA} or the OHU_{wSA} trend—a similar negative relationship with SO–SEP correlations is found. In fact, the correlation with the OHU_{wSA} trend yields an R^2 comparable to that of CF_{wSA} (not shown). This indicates that the negative relationship between SO–SEP correlations and OHU_{wSA} is robust. However, due to the large uncertainty in observed climatological OHU_{wSA} and OHU_{wSA} trend, these metrics cannot be used for constraint and are therefore not shown.

The positive cross-model relationship between CF_{wSA} and SO–SEP correlations remains robust after removing ENSO-related variability (Fig. 4.3c) and tropical decadal variability (Fig. 4.3e). The relationship between CF_{wSA} and SO–SEP correlation is not primarily driven by ENSO-related variability. Removing ENSO-related variability does not significantly change the R^2 of this relationship nor its confidence interval of internal variability. This result is expected, as CF_{wSA} is more likely to influence SST signals transporting from the Southern Ocean to the tropics, rather than the reverse. Similarly, removing tropical decadal variability from SO and SEP SSTs does not significantly change the R^2, but slightly reduces the confidence interval, indicating that a small portion of the relationship may be linked to low-frequency variability, likely the related forced

signals (e.g., decadal SST trends) between the two regions that are mediated by cloud feedbacks (Chapter 3; Kang et al., 2023b).

The negative cross-model relationship between $OHU_{wSA}\ sdv.$ and SO–SEP correlations remains robust after removing ENSO-related variability (Fig. 4.3d), but is not robust after removing tropical decadal variability (Fig. 4.3f). Removing ENSO-related variability increases the R^2 value, indicating that ENSO-related variability adds noise to the SO-SEP relationship. This suggests that this relationship can be attributed to low-frequency variability, which is verified by applying a 10-year high-pass filter to SO and SEP SSTs. As a result, the sign of the relationship between $OHU_{wSA}\ sdv.$ and SO–SEP correlations becomes highly uncertain, and the overall R^2 value decreases.

I have shown the relationships between the two physical drivers and SO–SEP correlations that include the forced response. The relationships based on SO–SEP correlations with the forced response removed (i.e., after subtracting the ensemble means) are not directly comparable to observations and therefore cannot be used for observational constraints. As such, they are not shown or discussed here.

4.4 Conclusion and discussion

I analyze the relationship between the Southern Ocean and the southeastern subtropical Pacific across 26 CMIP6 models. I find that during the historical period from 1985 to 2014, the spatial pattern of simulated correlations between SSTs at each grid point and the regional averages over the SO and SEP regions is broadly consistent with observations. Both reveal a robust positive relationship between SO and SEP SSTs on interannual timescales.

The strength of this positive SO–SEP relationship is model-dependent, as is the dominant factor contributing to it. I examine the roles of ENSO-related variability, tropical decadal variability, and the forced response in changing the interannual correlations between SO and SEP SSTs. In some models, the positive correlation arises because SO and SEP SSTs are both influenced by ENSO-related variability, while in others, it is mainly attributed to the covarying low-frequency variability between the two regions (likely related to the relationship between SST trends discussed in Chap-

ter 3). The contribution of the forced response is small and has minimal influence on SO–SEP correlations in most models. Overall, the multi-model mean SO–SEP correlation remains robust even after removing ENSO-related variability, tropical decadal variability, and the forced response. Similarly, the observed SO–SEP relationship—and the dominant variabilities contributing to it—varies across observational products.

The removal of ENSO-related variability—achieved by regressing out SSTs from the Niño3.4 region—and the removal of tropical decadal variability—using a 10-year high-pass filter applied to SO and SEP SSTs—are admittedly crude and simplistic approaches. I acknowledge that applying a 10-year high-pass filter may also unintentionally eliminate decadal-scale teleconnections from the Southern Ocean to the tropics, such as those mediated by ocean circulation systems like the subtropical gyre. This highlights the need for more carefully designed methodologies to isolate and remove potential confounding signals in the SO–SEP correlations.

Global-mean SST plays an important role in strengthening the relationship between SO and SEP SSTs, as shown in Chapters 2 and 3. However, in this chapter, I focus on the SO–SEP relationship driven by interannual internal variability, in contrast to the relationship between forced SST trends examined in Chapters 3. By removing each model's ensemble mean, I effectively remove the forced response from SST timeseries, including much of the global-mean SST signal. This approach provides a cleaner estimate of interannual internal variability than removing the global-mean SST alone.

Based on the mechanism proposed by Kim et al. (2022) and examined in Chapter 2 using coupled model outputs, I investigate the constraining effect of observed stratocumulus cloud feedback and ocean heat uptake variability on the simulated Southern Ocean-southeastern tropical Pacific relationship. I find that models that underestimate stratocumulus cloud feedback also tend to underestimate SO–SEP correlations. This relationship remains robust after removing ENSO-related variability and tropical decadal variability from SO and SEP SSTs. Conversely, models that underestimate ocean heat uptake variability tend to overestimate SO–SEP correlations. This negative

relationship primarily occurs on decadal timescales, as applying a 10-year high-pass filter significantly weakens the relationship.

Given that simulated SO–SEP correlations are generally underestimated relative to observations, the constraining effect of stratocumulus cloud feedback appears to be more influential. I suggest that models should strengthen the SO–SEP relationship, most likely by improving the representation of shortwave cloud feedback, given its demonstrated positive effect on the correlation. This is consistent with the argument put forward by Kim et al. (2022) and Kang et al. (2023a). In contrast, the physical mechanism by which ocean heat uptake influences the SO–SEP relationship remains less clear and should be investigated in detail through targeted perturbation experiments. Furthermore, additional observational datasets of ocean heat uptake are needed to better assess its role in shaping the SO–SEP relationship.

CHAPTER 5 CONCLUSION

5.1 Summary

In this dissertation, I investigate the relationship between sea surface temperatures (SSTs) in the Southern Ocean (SO) and the southeastern tropical Pacific (SEP). In Chapter 2, I analyze the relationship using 53 CMIP6 models in unforced pre-industrial control simulations and compare it to the relationship in forced simulations with an abrupt quadrupling of CO_2. In the pre-industrial control simulations, SO and SEP SSTs are positively correlated, both within individual models over time and across models averaged over time. This inter-model spread in SO–SEP correlations is partially explained by the radiative restoration strength of shortwave clouds off the west coast of South America, suggesting that models with stronger correlations tend to have stronger shortwave cloud feedback in that region. In the forced climate simulations, SO and SEP SST anomalies also show a strong positive correlation; however, this relationship is heavily influenced by global-mean warming, as warmer models tend to show stronger warming in both regions. This motivates analyses of the SST pattern, revealing a robust relationship between delayed warming in the SO and the SEP after removing the global-mean warming through various methods. The model spread in SO–SEP correlations is largely attributable to the spread in shortwave cloud feedback and anomalous ocean heat uptake off the west coast of South America. Models with stronger SO–SEP correlations in SST pattern tend to have both stronger shortwave cloud feedback and greater reductions in ocean heat uptake off the west coast of South America. This chapter extends the study of the SO–SEP relationship beyond perturbation experiments—commonly used in prior studies—to coupled model outputs, thereby avoiding artificial effects of unrealistically large forcing. These findings point to the potential for constraining the SO–SEP relationship using observational data, motivating the analysis of historical simulations presented in Chapter 3.

In Chapter 3, I examine the relationship between 30-year SST trends over the historical period from 1985 to 2014 in the SO and the SEP using 42 CMIP6 models. Most models fail to reproduce the observed cooling trends in both regions, instead simulating delayed warming trends

compared to the global-mean. The erroneous positive SST trends in these regions are positively related. Although this relationship is largely attributable to global-mean SST trends, the relationship remains robustly positive after removing the global-mean warming. Building on the roles of shortwave cloud feedback and ocean heat uptake identified in Chapter 2, I then assess the observational constraint of stratocumulus cloud feedback and ocean heat uptake variability on the simulated SO–SEP relationship. I find that most models underestimate both factors, leading to opposing constraint effects: strengthening the cloud feedback strengthens the SO–SEP relationship, while strengthening the ocean heat uptake variability weakens it. Furthermore, I link the SO–SEP relationship to equilibrium climate sensitivity (ECS), with implications for the "hot model" problem. Models with higher ECS tend to show stronger cross-model SO–SEP relationships. This chapter links the erroneous warming in the SEP to that in the SO under historical forcing in climate models, demonstrating the robustness of the SO–SEP relationship in the "real-world" regime. It highlights the importance of both shortwave cloud feedback and ocean heat uptake off the west coast of South America in improving the relationship between SST trends in these two regions in climate models. However, due to the focus on cross-model analysis on SST trends, this chapter does not quantify the SO–SEP relationship in observations, leaving the simulated SO-SEP relationship incomparable to that in observations. This limitation motivates Chapter 4, where I investigate the SO–SEP relationship on interannual timescales using correlations that can be measured within each model and observations.

In Chapter 4, I analyze the SO–SEP relationship on interannual timescales during the historical period from 1985 to 2014 using 26 CMIP6 models. I find that the spatial pattern of simulated correlations between SSTs at each grid point and regional averages over the SO and SEP regions is broadly consistent with observations, with both showing a robust positive relationship between SO and SEP SSTs. However, the magnitude of correlation is model-dependent, as is the dominant contributing factor. In some models, the positive correlation is primarily driven by ENSO-related variability influencing both regions, while in others, it reflects covarying low-frequency variability between the SO and SEP. Despite these differences, the multi-model mean SO–SEP

correlation remains robust after removing ENSO-related variability, tropical decadal variability, and the forced response. Similarly, the observed SO–SEP relationship and the dominant source of variability vary across different observational products. Building on the roles of shortwave cloud feedback and ocean heat uptake identified in Chapter 2, I examine the constraining effects of observed stratocumulus cloud feedback and ocean heat uptake variability on the interannual SO–SEP correlation. I find that models that underestimate stratocumulus cloud feedback also tend to underestimate SO–SEP correlations—a relationship that remains robust even after removing ENSO-related and decadal variability from the SSTs. Conversely, models that underestimate ocean heat uptake variability tend to overestimate SO–SEP correlations. This negative relationship primarily reflects decadal-scale processes, as it becomes significantly weaker when a 10-year high-pass filter is applied. Given that simulated SO–SEP correlations are generally underestimated relative to observations, the constraining effect of stratocumulus cloud feedback appears more influential, while the role of ocean heat uptake is non-negligible. Improving the SO–SEP relationship solely by strengthening cloud feedback may ultimately lead to an overestimated relationship. Therefore, both cloud feedback and ocean heat uptake should be considered when improving the SO–SEP relationship in climate models.

5.2 Outlook

The results presented in this dissertation raise several interesting questions. First, what is the causal relationship between SSTs in the SO and the SEP, and do climate models agree on the timescale of this relationship? Unlike perturbation experiments, where causality is more easily identified by applying a known forcing and observing the response, disentangling causal links in data-driven analyses is inherently challenging due to the tight coupling of physical processes operating on similar timescales. My preliminary causality-oriented analysis suggests a lagged relationship between SO and SEP SSTs on the monthly timescale. To avoid complications associated with causality, this dissertation focuses on annual data, where monthly lags are aggregated into a lag-0 annual relationship. Additionally, while my analysis emphasizes the teleconnection from the SO to the SEP, I acknowledge the influence of other contributing factors, such as ENSO-related

teleconnections, South Pacific Rossby wave dynamics, and wind anomalies over the southern high latitudes (Schneider and Deser, 2018; Dong et al., 2022; Wang et al., 2022). I preliminarily remove ENSO-related and tropical decadal variability from the SSTs, showing that the annual lag-0 SO–SEP relationship is not primarily driven by either. However, a more detailed investigation is needed to clarify the directionality of the teleconnection, for which a causality analysis will be essential. Determining the direction of this teleconnection is critical for diagnosing the relative influence of tropical versus extratropical variability in driving SST biases in the SEP in climate models. Such understanding is key to improving climate projections and identifying models that more realistically simulate relevant teleconnection processes on timescales consistent with observations.

Building on the SO–SEP causality, it is also important to explore ENSO's potential interaction with SEP. The causal relationship between the eastern tropical Pacific (EP) and SEP SSTs remains a topic of ongoing debate in the ENSO research community, particularly concerning whether the South Pacific Meridional Mode acts as a precursor to ENSO events or merely reflects ENSO's influence (e.g., Zhang et al., 2014; Jin and Kirtman, 2009; Amaya, 2019). It is possible that the SO–SEP teleconnection originates from ENSO—ENSO-related teleconnections influence SO SSTs, which are subsequently advected equatorward toward the SEP. However, this hypothesis remains speculative and warrants future investigation. Disentangling the relationship between EP and SEP could also help reconcile the discrepancy between results from perturbed experiments and coupled model outputs: the former often show SO-induced SST signals reaching into the tropics, while the latter show the delayed warming confined to the subtropics. Moreover, it remains unclear why delayed warming appears only in the SEP, even though SSTs across the broader EP exhibit covariability with the Southern Ocean. This may suggest that climatological SSTs in the EP are more strongly influenced by other processes, while the remote influence of the Southern Ocean only acts on its internal variability.

Second, what is the role of the dynamic ocean in the teleconnection from the SO to the SEP? This question arises from an inconsistency: my results suggest that the SO plays an important role

in influencing future warming projections through its teleconnection to the SEP, consistent with Kang et al. (2023a,b), whereas Green's function studies suggest that the SO has little influence on the Earth's radiative feedback and climate sensitivity (e.g., Dong et al., 2021; Bloch-Johnson et al., 2024). As noted by Bloch-Johnson et al. (2024), Green's function methods primarily capture atmospheric processes, while extratropical influences on global climate are often mediated by the ocean. This implies that ocean circulation is a key factor in the SO–SEP connection. In addition, some perturbation experiments have shown that the tropical Pacific response is muted when a dynamic ocean is included (e.g., Kay et al., 2016; Hawcroft et al., 2017; Green and Marshall, 2017; Kang et al., 2018b), while other studies showed evident tropical responses following a perturbed Southern Ocean climate in fully coupled climate models (e.g., Mechoso et al., 2016; Kim et al., 2022; Dong et al., 2022), leaving the role of the dynamic ocean in mediating the SO–SEP teleconnection an open question. In this dissertation, I identify ocean heat uptake in the coastal upwelling region off the west coast of South America as a key factor. While my analysis offers only an initial exploration of the effect of ocean circulation on SO-SEP teleconnection, my results already reveal some issues regarding its representation in models and observations, underscoring the need for further investigation. Targeted perturbation experiments, such as model intercomparisons of SEP responses to SO forcing in models with and without dynamic oceans, or idealized ocean-only experiments would be essential next steps in advancing my understanding of the ocean's role in this teleconnection.

Finally, what is the contribution of SO SST to warm SST biases in the SEP, relative to other local physical processes? The SEP region exhibits a long-standing warm SST bias in climate models, along with eastern boundary regions in other ocean basins. This bias has been attributed to underestimated stratocumulus cloud decks, weak alongshore winds and upwelling, and insufficient model resolution to capture mesoscale eddies and the thermocline structure (Richter, 2015). Notably, some of these local bias mechanisms overlap with the physical pathway of the teleconnection from the SO to the SEP, raising questions about the relative contributions of remote versus local processes. Based on my analysis of the SO–SEP relationship across different forcing scenarios and

models, I can confidently say that part of SEP SST is affected by SO SST. However, quantifying its contribution relative to local processes remains challenging due to overlapping mechanisms. One possible approach would be to compare SEP responses to perturbations in the subtropical region and in the Southern Ocean, following a framework similar to that used in Yu and Pritchard (2019).

After decades of climate model development, it may seem discouraging that both models and observations still face challenges in representing key physical processes, and that many aspects of the climate system remain not fully understood. However, from perturbation experiments to coupled model simulations, and from idealized frameworks to model simulations that more closely reflect the real-world climate system, each step brings us closer to more accurate climate simulations and more reliable projections. Progress may be small, but we are closer than we were yesterday.

REFERENCES

Alessi, M. J., and M. A. Rugenstein, 2023: Surface temperature pattern scenarios suggest higher warming rates than current projections. *Geophysical Research Letters*, **50 (23)**, e2023GL105 795.

Amaya, D. J., 2019: The pacific meridional mode and enso: A review. *Current Climate Change Reports*, **5 (4)**, 296–307.

Andrews, T., J. M. Gregory, and M. J. Webb, 2015: The dependence of radiative forcing and feedback on evolving patterns of surface temperature change in climate models. *Journal of Climate*, **28 (4)**, 1630–1648.

Andrews, T., and M. J. Webb, 2018: The dependence of global cloud and lapse rate feedbacks on the spatial structure of tropical pacific warming. *Journal of Climate*, **31 (2)**, 641–654.

Armour, K. C., C. M. Bitz, and G. H. Roe, 2013: Time-varying climate sensitivity from regional feedbacks. *Journal of Climate*, **26 (13)**, 4518–4534.

Armour, K. C., J. Marshall, J. R. Scott, A. Donohoe, and E. R. Newsom, 2016: Southern ocean warming delayed by circumpolar upwelling and equatorward transport. *Nature Geoscience*, **9 (7)**, 549–554.

Bader, D. C., R. Leung, M. Taylor, and R. B. McCoy, 2019: E3sm-project e3sm1.0 model output prepared for cmip6 cmip. Earth System Grid Federation, URL https://doi.org/10.22033/ESGF/CMIP6.2294, https://doi.org/10.22033/ESGF/CMIP6.2294.

Bader, D. C., R. Leung, M. Taylor, and R. B. McCoy, 2022: E3sm-project e3sm2.0 model output prepared for cmip6 cmip. Earth System Grid Federation, URL https://doi.org/10.22033/ESGF/CMIP6.16941, https://doi.org/10.22033/ESGF/CMIP6.16941.

Bader, D. C., R. Leung, M. Taylor, and R. B. McCoy, 2023: E3sm-project e3sm2.0narrm model output prepared for cmip6 cmip. Earth System Grid Federation, URL https://doi.org/10.22033/ESGF/CMIP6.17481, https://doi.org/10.22033/ESGF/CMIP6.17481.

Bentsen, M., and Coauthors, 2019: Ncc noresm2-mm model output prepared for cmip6 cmip. Earth System Grid Federation, URL https://doi.org/10.22033/ESGF/CMIP6.506, https://doi.org/10.22033/ESGF/CMIP6.506.

Bloch-Johnson, J., and Coauthors, 2024: The green's function model intercomparison project (gfmip) protocol. *Journal of Advances in Modeling Earth Systems*, **16 (2)**, e2023MS003 700.

Bograd, S. J., and Coauthors, 2023: Climate change impacts on eastern boundary upwelling systems. *Annual Review of Marine Science*, **15 (1)**, 303–328.

Boucher, O., and Coauthors, 2018: Ipsl ipsl-cm6a-lr model output prepared for cmip6 cmip. Earth System Grid Federation, URL https://doi.org/10.22033/ESGF/CMIP6.1534, https://doi.org/10.22033/ESGF/CMIP6.1534.

Byun, Y.-H., Y.-J. Lim, H. M. Sung, J. Kim, M. Sun, and B.-H. Kim, 2019: Nims-kma kace1.0-g model output prepared for cmip6 cmip historical. Earth System Grid Federation, URL https://doi.org/10.22033/ESGF/CMIP6.8378, https://doi.org/10.22033/ESGF/CMIP6.8378.

Cai, W., and Coauthors, 2023: Southern ocean warming and its climatic impacts. *Science Bulletin*.

Cao, J., and B. Wang, 2019: Nuist nesmv3 model output prepared for cmip6 cmip. Earth System Grid Federation, URL https://doi.org/10.22033/ESGF/CMIP6.2021, https://doi.org/10.22033/ESGF/CMIP6.2021.

Ceppi, P., and J. M. Gregory, 2017: Relationship of tropospheric stability to climate sensitivity and earth's observed radiation budget. *Proceedings of the National Academy of Sciences*, **114 (50)**, 13 126–13 131.

Ceppi, P., and P. Nowack, 2021: Observational evidence that cloud feedback amplifies global warming. *Proceedings of the National Academy of Sciences*, **118 (30)**, e2026290 118.

Clement, A. C., R. Seager, M. A. Cane, and S. E. Zebiak, 1996: An ocean dynamical thermostat. *Journal of Climate*, **9 (9)**, 2190–2196.

Czaja, A., P. Van der Vaart, and J. Marshall, 2002: A diagnostic study of the role of remote forcing in tropical atlantic variability. *Journal of Climate*, **15 (22)**, 3280–3290.

Danabasoglu, G., 2019a: Ncar cesm2-fv2 model output prepared for cmip6 cmip. Earth System Grid Federation, URL https://doi.org/10.22033/ESGF/CMIP6.11281, https://doi.org/10.22033/ESGF/CMIP6.11281.

Danabasoglu, G., 2019b: Ncar cesm2 model output prepared for cmip6 cmip. Earth System Grid Federation, URL https://doi.org/10.22033/ESGF/CMIP6.2185, https://doi.org/10.22033/ESGF/CMIP6.2185.

Danabasoglu, G., 2019c: Ncar cesm2-waccm-fv2 model output prepared for cmip6 cmip. Earth System Grid Federation, URL https://doi.org/10.22033/ESGF/CMIP6.11282, https://doi.org/10.22033/ESGF/CMIP6.11282.

Danabasoglu, G., 2019d: Ncar cesm2-waccm model output prepared for cmip6 cmip. Earth System Grid Federation, URL https://doi.org/10.22033/ESGF/CMIP6.10024, https://doi.org/10.22033/ESGF/CMIP6.10024.

Deser, C., R. Guo, and F. Lehner, 2017: The relative contributions of tropical pacific sea surface temperatures and atmospheric internal variability to the recent global warming hiatus. *Geophysical Research Letters*, **44 (15)**, 7945–7954.

Deser, C., and Coauthors, 2020: Isolating the evolving contributions of anthropogenic aerosols and greenhouse gases: A new cesm1 large ensemble community resource. *Journal of climate*, **33 (18)**, 7835–7858.

Dettinger, M. D., D. R. Cayan, H. F. Diaz, and D. M. Meko, 1998: North–south precipitation patterns in western north america on interannual-to-decadal timescales. *Journal of Climate*, **11 (12)**, 3095–3111.

Dix, M., and Coauthors, 2019: Csiro-arccss access-cm2 model output prepared for cmip6 cmip. Earth System Grid Federation, URL https://doi.org/10.22033/ESGF/CMIP6.2281, https://doi.org/10.22033/ESGF/CMIP6.2281.

Dong, Y., K. C. Armour, D. S. Battisti, and E. Blanchard-Wrigglesworth, 2022: Two-way teleconnections between the southern ocean and the tropical pacific via a dynamic feedback. *Journal of Climate*, **35 (19)**, 6267–6282.

Dong, Y., K. C. Armour, M. D. Zelinka, C. Proistosescu, D. S. Battisti, C. Zhou, and T. Andrews, 2020: Intermodel spread in the pattern effect and its contribution to climate sensitivity in cmip5 and cmip6 models. *Journal of Climate*, **33 (18)**, 7755–7775.

Dong, Y., C. Proistosescu, K. C. Armour, and D. S. Battisti, 2019: Attributing historical and future evolution of radiative feedbacks to regional warming patterns using a green's function approach: The preeminence of the western pacific. *Journal of Climate*, **32 (17)**, 5471–5491.

Dong, Y., and Coauthors, 2021: Biased estimates of equilibrium climate sensitivity and transient climate response derived from historical cmip6 simulations. *Geophysical Research Letters*, **48 (24)**, e2021GL095 778.

EC-Earth, 2019a: Ec-earth-consortium ec-earth3 model output prepared for cmip6 cmip. Earth System Grid Federation, URL https://doi.org/10.22033/ESGF/CMIP6.181, https://doi.org/10.22033/ESGF/CMIP6.181.

EC-Earth, 2019b: Ec-earth-consortium ec-earth3-veg model output prepared for cmip6 cmip. Earth System Grid Federation, URL https://doi.org/10.22033/ESGF/CMIP6.642, https://doi.org/10.22033/ESGF/CMIP6.642.

EC-Earth, 2020a: Ec-earth-consortium ec-earth-3-cc model output prepared for cmip6 cmip. Earth System Grid Federation, URL https://doi.org/10.22033/ESGF/CMIP6.640, https://doi.org/10.22033/ESGF/CMIP6.640.

EC-Earth, 2020b: Ec-earth-consortium ec-earth3-aerchem model output prepared for cmip6 cmip. Earth System Grid Federation, URL https://doi.org/10.22033/ESGF/CMIP6.639, https://doi.org/10.22033/ESGF/CMIP6.639.

EC-Earth, 2020c: Ec-earth-consortium ec-earth3-veg-lr model output prepared for cmip6 cmip. Earth System Grid Federation, URL https://doi.org/10.22033/ESGF/CMIP6.643, https://doi.org/10.22033/ESGF/CMIP6.643.

England, M. H., and Coauthors, 2014: Recent intensification of wind-driven circulation in the pacific and the ongoing warming hiatus. *Nature climate change*, **4 (3)**, 222–227.

Flores-Aqueveque, V., M. Rojas, C. Aguirre, P. A. Arias, and C. González, 2020: South pacific subtropical high from the late holocene to the end of the 21st century: insights from climate proxies and general circulation models. *Climate of the Past*, **16 (1)**, 79–99.

Forster, P., and Coauthors, 2023: *The Earth's Energy Budget, Climate Feedbacks and Climate Sensitivity*, 923–1054. Cambridge University Press, https://doi.org/10.1017/9781009157896.009.

Fox-Kemper, B., and Coauthors, 2021: *Ocean, Cryosphere and Sea Level Change*, 1211–1362. Cambridge University Press, Cambridge, United Kingdom and New York, NY, USA, https://doi.org/10.1017/9781009157896.011.

Green, B., and J. Marshall, 2017: Coupling of trade winds with ocean circulation damps itcz shifts. *Journal of Climate*, **30 (12)**, 4395–4411.

Guo, H., and Coauthors, 2018: Noaa-gfdl gfdl-cm4 model output. Earth System Grid Federation, URL https://doi.org/10.22033/ESGF/CMIP6.1402, https://doi.org/10.22033/ESGF/CMIP6.1402.

Hajima, T., and Coauthors, 2019a: Miroc miroc-es2l model output prepared for cmip6 cmip. Earth System Grid Federation, URL https://doi.org/10.22033/ESGF/CMIP6.902, https://doi.org/10.22033/ESGF/CMIP6.902.

Hajima, T., and Coauthors, 2019b: Miroc miroc-es2l model output prepared for cmip6 cmip. Earth System Grid Federation, URL https://doi.org/10.22033/ESGF/CMIP6.902, https://doi.org/10.22033/ESGF/CMIP6.902.

Hall, A., P. Cox, C. Huntingford, and S. Klein, 2019: Progressing emergent constraints on future climate change. *Nature Climate Change*, **9 (4)**, 269–278.

Hartmann, D. L., 2022: The antarctic ozone hole and the pattern effect on climate sensitivity. *Proceedings of the National Academy of Sciences*, **119 (35)**, e2207889 119.

Hausfather, Z., K. Marvel, G. A. Schmidt, J. W. Nielsen-Gammon, and M. Zelinka, 2022: Climate simulations: recognize the 'hot model'problem. *Nature*, **605 (7908)**, 26–29.

Hawcroft, M., J. M. Haywood, M. Collins, A. Jones, A. C. Jones, and G. Stephens, 2017: Southern ocean albedo, inter-hemispheric energy transports and the double itcz: Global impacts of biases in a coupled model. *Climate Dynamics*, **48**, 2279–2295.

Haywood, J. M., and Coauthors, 2016: The impact of equilibrating hemispheric albedos on tropical performance in the hadgem2-es coupled climate model. *Geophysical Research Letters*, **43 (1)**, 395–403.

Hedemann, C., T. Mauritsen, J. Jungclaus, and J. Marotzke, 2022: Reconciling conflicting accounts of local radiative feedbacks in climate models. *Journal of Climate*, **35 (10)**, 3131–3146.

Heede, U. K., and A. V. Fedorov, 2021: Eastern equatorial pacific warming delayed by aerosols and thermostat response to co2 increase. *Nature Climate Change*, **11 (8)**, 696–703.

Heede, U. K., A. V. Fedorov, and N. J. Burls, 2020: Time scales and mechanisms for the tropical pacific response to global warming: A tug of war between the ocean thermostat and weaker walker. *Journal of Climate*, **33 (14)**, 6101–6118.

Heede, U. K., A. V. Fedorov, and N. J. Burls, 2021: A stronger versus weaker walker: understanding model differences in fast and slow tropical pacific responses to global warming. *Climate Dynamics*, **57 (9)**, 2505–2522.

Held, I. M., M. Winton, K. Takahashi, T. Delworth, F. Zeng, and G. K. Vallis, 2010: Probing the fast and slow components of global warming by returning abruptly to preindustrial forcing. *Journal of Climate*, **23 (9)**, 2418–2427.

Hersbach, H., and Coauthors, 2023: Era5 hourly data on single levels from 1940 to present, copernicus climate change service (c3s) climate data store (cds)[data set].

Huang, B., C. Liu, V. Banzon, E. Freeman, G. Graham, B. Hankins, T. Smith, and H.-M. Zhang, 2021: Improvements of the daily optimum interpolation sea surface temperature (doisst) version 2.1. *Journal of Climate*, **34 (8)**, 2923–2939.

Huang, B., and Coauthors, 2017: Noaa extended reconstructed sea surface temperature (ersst), version 5, noaa national centers for environmental information [data set]. *(Accessed Jan 2025)*.

Huang, W., 2019: Thu ciesm model output prepared for cmip6 cmip. Earth System Grid Federation, URL https://doi.org/10.22033/ESGF/CMIP6.1352, https://doi.org/10.22033/ESGF/CMIP6.1352.

Hwang, Y.-T., and D. M. Frierson, 2013: Link between the double-intertropical convergence zone problem and cloud biases over the southern ocean. *Proceedings of the National Academy of Sciences*, **110 (13)**, 4935–4940.

Hwang, Y.-T., S.-P. Xie, P.-J. Chen, H.-Y. Tseng, and C. Deser, 2024: Contribution of anthropogenic aerosols to persistent la niña-like conditions in the early 21st century. *Proceedings of the National Academy of Sciences*, **121 (5)**, e2315124 121.

Hwang, Y.-T., S.-P. Xie, C. Deser, and S. M. Kang, 2017: Connecting tropical climate change with southern ocean heat uptake. *Geophysical Research Letters*, **44 (18)**, 9449–9457.

Jiang, N., C. Zhu, Z.-Z. Hu, M. J. McPhaden, T. Lian, C. Zhou, W. Qian, and D. Chen, 2025: El niño and sea surface temperature pattern effects lead to historically high global mean surface temperatures in 2023. *Geophysical Research Letters*, **52 (2)**, e2024GL113 733.

Jin, D., and B. P. Kirtman, 2009: Why the southern hemisphere enso responses lead enso. *Journal of Geophysical Research: Atmospheres*, **114 (D23)**.

Jungclaus, J., and Coauthors, 2019: Mpi-m mpiesm1.2-hr model output prepared for cmip6 cmip. Earth System Grid Federation, URL https://doi.org/10.22033/ESGF/CMIP6.741, https://doi.org/10.22033/ESGF/CMIP6.741.

Kajtar, J. B., A. Santoso, M. Collins, A. S. Taschetto, M. H. England, and L. M. Frankcombe, 2021: Cmip5 intermodel relationships in the baseline southern ocean climate system and with future projections. *Earth's Future*, **9 (6)**, e2020EF001 873.

Kajtar, J. B., A. Santoso, S. McGregor, M. H. England, and Z. Baillie, 2018: Model underrepresentation of decadal pacific trade wind trends and its link to tropical atlantic bias. *Climate dynamics*, **50 (3)**, 1471–1484.

Kämpf, J., and P. Chapman, 2016: *Upwelling systems of the world*. Springer.

Kang, S. M., P. Ceppi, Y. Yu, and I.-S. Kang, 2023a: Recent global climate feedback controlled by southern ocean cooling. *Nature Geoscience*, **16 (9)**, 775–780.

Kang, S. M., K. Park, Y.-T. Hwang, and W.-T. Hsiao, 2018a: Contrasting tropical climate response pattern to localized thermal forcing over different ocean basins. *Geophysical Research Letters*, **45 (22)**, 12–544.

Kang, S. M., Y. Shin, and S.-P. Xie, 2018b: Extratropical forcing and tropical rainfall distribution: energetics framework and ocean ekman advection. *npj Climate and Atmospheric Science*, **1 (1)**, 20 172.

Kang, S. M., S.-P. Xie, Y. Shin, H. Kim, Y.-T. Hwang, M. F. Stuecker, B. Xiang, and M. Hawcroft, 2020: Walker circulation response to extratropical radiative forcing. *Science advances*, **6 (47)**, eabd3021.

Kang, S. M., Y. Yu, C. Deser, X. Zhang, I.-S. Kang, S.-S. Lee, K. B. Rodgers, and P. Ceppi, 2023b: Global impacts of recent southern ocean cooling. *Proceedings of the National Academy of Sciences*, **120 (30)**, e2300881 120.

Kay, J. E., C. Wall, V. Yettella, B. Medeiros, C. Hannay, P. Caldwell, and C. Bitz, 2016: Global climate impacts of fixing the southern ocean shortwave radiation bias in the community earth system model (cesm). *Journal of Climate*, **29 (12)**, 4617–4636.

Kim, H., S. M. Kang, J. E. Kay, and S.-P. Xie, 2022: Subtropical clouds key to southern ocean teleconnections to the tropical pacific. *Proceedings of the National Academy of Sciences*, **119 (34)**, e2200514 119.

Kim, Y., Y. Noh, D. Kim, M.-I. Lee, H. J. Lee, S. Y. Kim, and D. Kim, 2019: Kiost kiost-esm model output prepared for cmip6 cmip. Earth System Grid Federation, URL https://doi.org/10.22033/ESGF/CMIP6.1922, https://doi.org/10.22033/ESGF/CMIP6.1922.

Knutti, R., M. A. Rugenstein, and G. C. Hegerl, 2017: Beyond equilibrium climate sensitivity. *Nature Geoscience*, **10 (10)**, 727–736.

Kosaka, Y., and S.-P. Xie, 2016: The tropical pacific as a key pacemaker of the variable rates of global warming. *Nature Geoscience*, **9 (9)**, 669–673.

Kostov, Y., K. C. Armour, and J. Marshall, 2014: Impact of the atlantic meridional overturning circulation on ocean heat storage and transient climate change. *Geophysical Research Letters*, **41 (6)**, 2108–2116.

Kostov, Y., D. Ferreira, K. C. Armour, and J. Marshall, 2018: Contributions of greenhouse gas forcing and the southern annular mode to historical southern ocean surface temperature trends. *Geophysical Research Letters*, **45 (2)**, 1086–1097.

Krasting, J. P., and Coauthors, 2018: Noaa-gfdl gfdl-esm4 model output prepared for cmip6 cmip. Earth System Grid Federation, URL https://doi.org/10.22033/ESGF/CMIP6.1407, https://doi.org/10.22033/ESGF/CMIP6.1407.

Lee, W.-L., and H.-C. Liang, 2020: As-rcec taiesm1.0 model output prepared for cmip6 cmip historical. Earth System Grid Federation, URL https://doi.org/10.22033/ESGF/CMIP6.9755, https://doi.org/10.22033/ESGF/CMIP6.9755.

Li, L., 2019: Cas fgoals-g3 model output prepared for cmip6 cmip historical. Earth System Grid Federation, URL https://doi.org/10.22033/ESGF/CMIP6.3356, https://doi.org/10.22033/ESGF/CMIP6.3356.

Li, X., and Coauthors, 2021: Tropical teleconnection impacts on antarctic climate changes. *Nature Reviews Earth & Environment*, **2 (10)**, 680–698.

Lin, Y.-J., Y.-T. Hwang, J. Lu, F. Liu, and B. E. Rose, 2021: The dominant contribution of southern ocean heat uptake to time-evolving radiative feedback in cesm. *Geophysical Research Letters*, **48 (9)**, e2021GL093 302.

Liu, C., and R. Allan, 2022: Reconstructions of the radiation fluxes at the top of atmosphere and net surface energy flux: Deep-c version 5.0.

Liu, F., J. Lu, Y. Huang, L. R. Leung, B. E. Harrop, and Y. Luo, 2020: Sensitivity of surface temperature to oceanic forcing via q-flux green's function experiments. part iii: asymmetric response to warming and cooling. *Journal of Climate*, **33 (4)**, 1283–1297.

Lorenz, S., and Coauthors, 2021: Mpi-m icon-esm model output prepared for cmip6 cmip. Earth System Grid Federation, URL https://doi.org/10.22033/ESGF/CMIP6.743, https://doi.org/10.22033/ESGF/CMIP6.743.

Lovato, T., and D. Peano, 2020: Cmcc cmcc-cm2-sr5 model output prepared for cmip6 cmip. Earth System Grid Federation, URL https://doi.org/10.22033/ESGF/CMIP6.1362, https://doi.org/10.22033/ESGF/CMIP6.1362.

Lovato, T., D. Peano, and M. Butenschön, 2021: Cmcc cmcc-esm2 model output prepared for cmip6 cmip. Earth System Grid Federation, URL https://doi.org/10.22033/ESGF/CMIP6.13164, https://doi.org/10.22033/ESGF/CMIP6.13164.

Luo, J.-J., G. Wang, and D. Dommenget, 2018: May common model biases reduce cmip5's ability to simulate the recent pacific la niña-like cooling? *Climate Dynamics*, **50**, 1335–1351.

Ma, J., S. Xu, and B. Wang, 2019: Warm bias of sea surface temperature in eastern boundary current regions—a study of effects of horizontal resolution in cesm. *Ocean Dynamics*, **69**, 939–954.

Manabe, S., and K. Bryan, 1969: Climate calculations with a combined ocean-atmosphere model. *Journal of Atmospheric Sciences*, **26 (4)**, 786–789.

Manabe, S., and R. T. Wetherald, 1975: The effects of doubling the co 2 concentration on the climate of a general circulation model. *Journal of Atmospheric Sciences*, **32 (1)**, 3–15.

Mechoso, C. R., and Coauthors, 2016: Can reducing the incoming energy flux over the southern ocean in a cgcm improve its simulation of tropical climate? *Geophysical Research Letters*, **43 (20)**, 11–057.

Meehl, G. A., J. M. Arblaster, C. M. Bitz, C. T. Chung, and H. Teng, 2016: Antarctic sea-ice expansion between 2000 and 2014 driven by tropical pacific decadal climate variability. *Nature Geoscience*, **9 (8)**, 590–595.

Meijers, A., 2014: The southern ocean in the coupled model intercomparison project phase 5. *Philosophical Transactions of the Royal Society A: Mathematical, Physical and Engineering Sciences*, **372 (2019)**, 20130 296.

Mulcahy, J., and Coauthors, 2022: Mohc ukesm1.1-ll model output prepared for cmip6 cmip. Earth System Grid Federation, URL https://doi.org/10.22033/ESGF/CMIP6.16781, https://doi.org/10.22033/ESGF/CMIP6.16781.

Myers, T. A., R. C. Scott, M. D. Zelinka, S. A. Klein, J. R. Norris, and P. M. Caldwell, 2021: Observational constraints on low cloud feedback reduce uncertainty of climate sensitivity. *Nature Climate Change*, **11 (6)**, 501–507.

NASA/GISS, 2018a: Nasa-giss giss-e2.1g model output prepared for cmip6 cmip. Earth System Grid Federation, URL https://doi.org/10.22033/ESGF/CMIP6.1400, https://doi.org/10.22033/ESGF/CMIP6.1400.

NASA/GISS, 2018b: Nasa-giss giss-e2.1h model output prepared for cmip6 cmip. Earth System Grid Federation, URL https://doi.org/10.22033/ESGF/CMIP6.1421, https://doi.org/10.22033/ESGF/CMIP6.1421.

NASA/GISS, 2019a: Nasa-giss giss-e2-2-g model output prepared for cmip6 cmip. Earth System Grid Federation, URL https://doi.org/10.22033/ESGF/CMIP6.2081, https://doi.org/10.22033/ESGF/CMIP6.2081.

NASA/GISS, 2019b: Nasa-giss giss-e2.2h model output prepared for cmip6 cmip. Earth System Grid Federation, URL https://doi.org/10.22033/ESGF/CMIP6.15861, https://doi.org/10.22033/ESGF/CMIP6.15861.

Neubauer, D., and Coauthors, 2019: Hammoz-consortium mpi-esm1.2-ham model output prepared for cmip6 cmip. Earth System Grid Federation, URL https://doi.org/10.22033/ESGF/CMIP6.1622, https://doi.org/10.22033/ESGF/CMIP6.1622.

Olonscheck, D., M. Rugenstein, and J. Marotzke, 2020: Broad consistency between observed and simulated trends in sea surface temperature patterns. *Geophysical Research Letters*, **47 (10)**, e2019GL086 773.

Park, S., and J. Shin, 2019: Snu sam0-unicon model output prepared for cmip6 cmip. Earth System Grid Federation, URL https://doi.org/10.22033/ESGF/CMIP6.1489, https://doi.org/10.22033/ESGF/CMIP6.1489.

Philander, S., D. Gu, G. Lambert, T. Li, D. Halpern, N. Lau, and R. C. Pacanowski, 1996: Why the itcz is mostly north of the equator. *Journal of climate*, **9 (12)**, 2958–2972.

Purich, A., W. Cai, M. H. England, and T. Cowan, 2016: Evidence for link between modelled trends in antarctic sea ice and underestimated westerly wind changes. *Nature communications*, **7 (1)**, 10 409.

Randall, D. A., and Coauthors, 2019: 100 years of earth system model development. *Meteorological Monographs*, **59**, 12–1.

Rayner, N. A., D. E. Parker, E. Horton, C. K. Folland, L. V. Alexander, D. Rowell, E. C. Kent, and A. Kaplan, 2003: Global analyses of sea surface temperature, sea ice, and night marine air temperature since the late nineteenth century. *Journal of Geophysical Research: Atmospheres*, **108 (D14)**.

Richter, I., 2015: Climate model biases in the eastern tropical oceans: Causes, impacts and ways forward. *Wiley Interdisciplinary Reviews: Climate Change*, **6 (3)**, 345–358.

Ridley, J., M. Menary, T. Kuhlbrodt, M. Andrews, and T. Andrews, 2018: Mohc hadgem3-gc31-ll model output prepared for cmip6 cmip. Earth System Grid Federation, URL https://doi.org/10.22033/ESGF/CMIP6.419, https://doi.org/10.22033/ESGF/CMIP6.419.

Ridley, J., M. Menary, T. Kuhlbrodt, M. Andrews, and T. Andrews, 2019: Mohc hadgem3-gc31-mm model output prepared for cmip6 cmip. Earth System Grid Federation, URL https://doi.org/10.22033/ESGF/CMIP6.420, https://doi.org/10.22033/ESGF/CMIP6.420.

Rong, X., 2019: Cams cams_csm1.0 model output prepared for cmip6 cmip. Earth System Grid Federation, URL https://doi.org/10.22033/ESGF/CMIP6.1399, https://doi.org/10.22033/ESGF/CMIP6.1399.

Rugenstein, M., S. Dhame, D. Olonscheck, R. J. Wills, M. Watanabe, and R. Seager, 2023: Connecting the sst pattern problem and the hot model problem. *Geophysical Research Letters*, **50 (22)**, e2023GL105 488.

Rugenstein, M. A., and K. C. Armour, 2021: Three flavors of radiative feedbacks and their implications for estimating equilibrium climate sensitivity. *Geophysical Research Letters*, **48 (15)**, e2021GL092 983.

Rye, C. D., J. Marshall, M. Kelley, G. Russell, L. S. Nazarenko, Y. Kostov, G. A. Schmidt, and J. Hansen, 2020: Antarctic glacial melt as a driver of recent southern ocean climate trends. *Geophysical Research Letters*, **47 (11)**, e2019GL086 892.

Rykaczewski, R. R., J. P. Dunne, W. J. Sydeman, M. García-Reyes, B. A. Black, and S. J. Bograd, 2015: Poleward displacement of coastal upwelling-favorable winds in the ocean's eastern boundary currents through the 21st century. *Geophysical Research Letters*, **42 (15)**, 6424–6431.

Schneider, D. P., and C. Deser, 2018: Tropically driven and externally forced patterns of antarctic sea ice change: Reconciling observed and modeled trends. *Climate Dynamics*, **50**, 4599–4618.

Seager, R., M. Cane, N. Henderson, D.-E. Lee, R. Abernathey, and H. Zhang, 2019: Strengthening tropical pacific zonal sea surface temperature gradient consistent with rising greenhouse gases. *Nature Climate Change*, **9 (7)**, 517–522.

Seager, R., N. Henderson, and M. Cane, 2022: Persistent discrepancies between observed and modeled trends in the tropical pacific ocean. *Journal of Climate*, **35 (14)**, 4571–4584.

Seferian, R., 2018: Cnrm-cerfacs cnrm-esm2-1 model output prepared for cmip6 cmip. Earth System Grid Federation, URL https://doi.org/10.22033/ESGF/CMIP6.1391, https://doi.org/10.22033/ESGF/CMIP6.1391.

Seland, y., and Coauthors, 2019: Ncc noresm2-lm model output prepared for cmip6 cmip. Earth System Grid Federation, URL https://doi.org/10.22033/ESGF/CMIP6.502, https://doi.org/10.22033/ESGF/CMIP6.502.

Semmler, T., and Coauthors, 2018: Awi awi-cm1.1mr model output prepared for cmip6 cmip. Earth System Grid Federation, URL https://doi.org/10.22033/ESGF/CMIP6.359, https://doi.org/10.22033/ESGF/CMIP6.359.

Senior, C. A., and J. F. Mitchell, 2000: The time-dependence of climate sensitivity. *Geophysical Research Letters*, **27 (17)**, 2685–2688.

Sherwood, S. C., and Coauthors, 2020: An assessment of earth's climate sensitivity using multiple lines of evidence. *Reviews of Geophysics*, **58 (4)**, e2019RG000 678.

Slivinski, L. C., and Coauthors, 2019: Towards a more reliable historical reanalysis: Improvements for version 3 of the twentieth century reanalysis system. *Quarterly Journal of the Royal Meteorological Society*, **145 (724)**, 2876–2908.

Song, Z., F. Qiao, Y. Bao, Q. Shu, Y. Song, and X. Yang, 2019: Fio-qlnm fio-esm2.0 model output prepared for cmip6 cmip. Earth System Grid Federation, URL https://doi.org/10.22033/ESGF/CMIP6.9047, https://doi.org/10.22033/ESGF/CMIP6.9047.

Stevens, B., S. C. Sherwood, S. Bony, and M. J. Webb, 2016: Prospects for narrowing bounds on earth's equilibrium climate sensitivity. *Earth's Future*, **4 (11)**, 512–522.

Stouffer, R., 2019: U of arizona mcm-ua-1-0 model output prepared for cmip6 cmip. Earth System Grid Federation, URL https://doi.org/10.22033/ESGF/CMIP6.2421, https://doi.org/10.22033/ESGF/CMIP6.2421.

Swart, N. C., and Coauthors, 2019a: Cccma canesm5 model output prepared for cmip6 cmip. Earth System Grid Federation, URL https://doi.org/10.22033/ESGF/CMIP6.1303, https://doi.org/10.22033/ESGF/CMIP6.1303.

Swart, N. C., and Coauthors, 2019b: Cccma canesm5.1 model output prepared for cmip6 cmip. Earth System Grid Federation, URL https://doi.org/10.22033/ESGF/CMIP6.17184, https://doi.org/10.22033/ESGF/CMIP6.17184.

Takahashi, K., and D. S. Battisti, 2007: Processes controlling the mean tropical pacific precipitation pattern. part i: The andes and the eastern pacific itcz. *Journal of Climate*, **20 (14)**, 3434–3451.

Tang, Y., S. Rumbold, R. Ellis, D. Kelley, J. Mulcahy, A. Sellar, J. Walton, and C. Jones, 2019: Mohc ukesm1.0-ll model output prepared for cmip6 cmip. Earth System Grid Federation, URL https://doi.org/10.22033/ESGF/CMIP6.1569, https://doi.org/10.22033/ESGF/CMIP6.1569.

Tatebe, H., and M. Watanabe, 2018: Miroc miroc6 model output prepared for cmip6 cmip. Earth System Grid Federation, URL https://doi.org/10.22033/ESGF/CMIP6.881, https://doi.org/10.22033/ESGF/CMIP6.881.

Tian, B., and X. Dong, 2020: The double-itcz bias in cmip3, cmip5, and cmip6 models based on annual mean precipitation. *Geophysical Research Letters*, **47 (8)**, e2020GL087 232.

Vimont, D. J., M. Alexander, and A. Fontaine, 2009: Midlatitude excitation of tropical variability in the pacific: The role of thermodynamic coupling and seasonality. *Journal of Climate*, **22 (3)**, 518–534.

Voldoire, A., 2018: Cnrm-cerfacs cnrm-cm6-1 model output prepared for cmip6 cmip. Earth System Grid Federation, URL https://doi.org/10.22033/ESGF/CMIP6.1375, https://doi.org/10.22033/ESGF/CMIP6.1375.

Voldoire, A., 2019: Cnrm-cerfacs cnrm-cm6-1-hr model output prepared for cmip6 cmip historical. Earth System Grid Federation, URL https://doi.org/10.22033/ESGF/CMIP6.4067, https://doi.org/10.22033/ESGF/CMIP6.4067.

Volodin, E., and Coauthors, 2019a: Inm inm-cm4-8 model output prepared for cmip6 cmip. Earth System Grid Federation, URL https://doi.org/10.22033/ESGF/CMIP6.1422, https://doi.org/10.22033/ESGF/CMIP6.1422.

Volodin, E., and Coauthors, 2019b: Inm inm-cm5-0 model output prepared for cmip6 cmip. Earth System Grid Federation, URL https://doi.org/10.22033/ESGF/CMIP6.1423, https://doi.org/10.22033/ESGF/CMIP6.1423.

Wang, G., and Coauthors, 2022: Future southern ocean warming linked to projected enso variability. *Nature Climate Change*, **12 (7)**, 649–654.

Watanabe, M., J.-L. Dufresne, Y. Kosaka, T. Mauritsen, and H. Tatebe, 2021a: Enhanced warming constrained by past trends in equatorial pacific sea surface temperature gradient. *Nature Climate Change*, **11 (1)**, 33–37.

Watanabe, M., S. M. Kang, M. Collins, Y.-T. Hwang, S. McGregor, and M. F. Stuecker, 2024: Possible shift in controls of the tropical pacific surface warming pattern. *Nature*, **630 (8016)**, 315–324.

Watanabe, S., and Coauthors, 2021b: Miroc miroc-es2h model output prepared for cmip6 cmip historical. Earth System Grid Federation, URL https://doi.org/10.22033/ESGF/CMIP6.5601, https://doi.org/10.22033/ESGF/CMIP6.5601.

Wieners, K.-H., and Coauthors, 2019: Mpi-m mpiesm1.2-lr model output prepared for cmip6 cmip. Earth System Grid Federation, URL https://doi.org/10.22033/ESGF/CMIP6.742, https://doi.org/10.22033/ESGF/CMIP6.742.

Wills, R. C., Y. Dong, C. Proistosecu, K. C. Armour, and D. S. Battisti, 2022: Systematic climate model biases in the large-scale patterns of recent sea-surface temperature and sea-level pressure change. *Geophysical Research Letters*, **49 (17)**, e2022GL100 011.

Xiang, B., M. Zhao, Y. Ming, W. Yu, and S. M. Kang, 2018: Contrasting impacts of radiative forcing in the southern ocean versus southern tropics on itcz position and energy transport in one gfdl climate model. *Journal of Climate*, **31 (14)**, 5609–5628.

Xie, S.-P., B. Lu, and B. Xiang, 2013: Similar spatial patterns of climate responses to aerosol and greenhouse gas changes. *Nature Geoscience*, **6 (10)**, 828–832.

Xie, S.-P., and S. G. H. Philander, 1994: A coupled ocean-atmosphere model of relevance to the itcz in the eastern pacific. *Tellus A*, **46 (4)**, 340–350.

Xin, X., and Coauthors, 2018: Bcc bcc-csm2mr model output prepared for cmip6 cmip. Earth System Grid Federation, URL https://doi.org/10.22033/ESGF/CMIP6.1725, https://doi.org/10.22033/ESGF/CMIP6.1725.

Yeager, S. G., and Coauthors, 2023: Reduced southern ocean warming enhances global skill and signal-to-noise in an eddy-resolving decadal prediction system. *npj Climate and Atmospheric Science*, **6 (1)**, 107.

Yu, S., and M. S. Pritchard, 2019: A strong role for the amoc in partitioning global energy transport and shifting itcz position in response to latitudinally discrete solar forcing in cesm1. 2. *Journal of Climate*, **32 (8)**, 2207–2226.

YU, Y., 2018: Cas fgoals-f3-l model output prepared for cmip6 cmip. Earth System Grid Federation, URL https://doi.org/10.22033/ESGF/CMIP6.1782, https://doi.org/10.22033/ESGF/CMIP6.1782.

Yuan, X., 2004: Enso-related impacts on antarctic sea ice: a synthesis of phenomenon and mechanisms. *Antarctic Science*, **16 (4)**, 415–425.

Yukimoto, S., and Coauthors, 2019: Mri mri-esm2.0 model output prepared for cmip6 cmip. Earth System Grid Federation, URL https://doi.org/10.22033/ESGF/CMIP6.621, https://doi.org/10.22033/ESGF/CMIP6.621.

Zelinka, M. D., T. A. Myers, D. T. McCoy, S. Po-Chedley, P. M. Caldwell, P. Ceppi, S. A. Klein, and K. E. Taylor, 2020: Causes of higher climate sensitivity in cmip6 models. *Geophysical Research Letters*, **47 (1)**, e2019GL085 782.

Zhang, H., A. Clement, and P. Di Nezio, 2014: The south pacific meridional mode: A mechanism for enso-like variability. *Journal of Climate*, **27 (2)**, 769–783.

Zhang, J., and Coauthors, 2018: Bcc bcc-esm1 model output prepared for cmip6 cmip. Earth System Grid Federation, URL https://doi.org/10.22033/ESGF/CMIP6.1734, https://doi.org/10.22033/ESGF/CMIP6.1734.

Zhang, L., T. L. Delworth, W. Cooke, and X. Yang, 2019a: Natural variability of southern ocean convection as a driver of observed climate trends. *Nature Climate Change*, **9 (1)**, 59–65.

Zhang, L., W. Han, K. B. Karnauskas, G. A. Meehl, A. Hu, N. Rosenbloom, and T. Shinoda, 2019b: Indian ocean warming trend reduces pacific warming response to anthropogenic greenhouse gases: An interbasin thermostat mechanism. *Geophysical Research Letters*, **46 (19)**, 10 882–10 890.

Zhang, X., C. Deser, and L. Sun, 2021: Is there a tropical response to recent observed southern ocean cooling? *Geophysical Research Letters*, **48 (5)**, e2020GL091 235.

Zhang, Y., and W. B. Rossow, 2023: Global radiative flux profile data set: Revised and extended. *Journal of Geophysical Research: Atmospheres*, **128 (5)**, e2022JD037 340.

Zheng, Y., M. Rugenstein, and J. M. Alessi, Accepted: The relationship between the Southern Ocean and the southeastern subtropical Pacific in unforced and forced climate model simulations. *Journal of Climate*.

Zhou, C., M. D. Zelinka, and S. A. Klein, 2016: Impact of decadal cloud variations on the earth's energy budget. *Nature Geoscience*, **9 (12)**, 871–874.

Ziehn, T., and Coauthors, 2019: Csiro access-esm1.5 model output prepared for cmip6 cmip. Earth System Grid Federation, URL https://doi.org/10.22033/ESGF/CMIP6.2288, https://doi.org/10.22033/ESGF/CMIP6.2288.

APPENDIX A SUPPORTING INFORMATION FOR CHAPTER 3

A.1 Text. Climatological ocean heat uptake and ocean heat uptake trend

Strong climatological oceanic upwelling occurs off the west coast of South America due to Ekman transport induced by the Humboldt Current System (e.g., Kämpf and Chapman, 2016). The spatial pattern of the multi-model mean climatological ocean heat uptake in CMIP6 models generally matches the observation mean (A.6a-b). Averaging the climatological ocean heat uptake over this region using the same box as in the main text (hereinafter referred to as climatological OHU_{wSA}), I find that models tend to underestimate the magnitude of climatological OHU_{wSA} (Figure A.6b-c).

Higher climatological ocean heat uptake suppresses positive SST trends advected from the Southern Ocean (SO) to the southeastern tropical Pacific (SEP) by climatological wind, resulting in weaker relationship between SST trends in these two regions. Grouping models by climatological OHU_{wSA}, the cross-model relationship between absolute SST trends in the SO and SEP shows that subsets with larger climatological OHU_{wSA} show a weaker SO-SEP relationship (lower R^2) (Figure A.6d), consistent with the negative dependence of R^2 on OHU_{wSA} $sdv.$ discussed in the main text. This negative dependence is not affected by internal variability and remains robust across different subset sizes.

However, when SST trends are normalized by global-mean warming, this negative dependence becomes positive: subsets with larger climatological OHU_{wSA} show stronger cross-model relationships between normalized SST trends in SO and SEP (higher R^2; Figure A.6b). Aside from the mechanism discussed in the previous paragraph, climatological OHU_{wSA} can also affect local SST signals through dynamical processes, e.g., associating with coastal winds and subtropical gyre. Models with larger climatological OHU_{wSA} may have stronger coastal winds and subtropical gyre, enabling more effective equatorward transport of SO SST signals, thus strengthening the SO-SEP relationship. This mechanism involves local dynamical processes that are less sensitive

to global-mean SST trends, explaining the positive dependence after normalization (blue line in Figure A.6b).

Overall, the constraining effect of climatological OHU_{wSA} on the SO-SEP relationship remains uncertain, due to its sensitivity to global-mean warming. Future studies are needed to further test these mechanisms.

The 30-year ocean heat uptake trend in the South Pacific is overall noisy, with large uncertainties coming from the large internal variability of ocean heat uptake. The heterogeneous spatial pattern of the ocean heat uptake trend makes the simulated and observed ocean heat uptake trend incomparable A.6e-f. A negative trend of ocean heat uptake off the west coast of South America is simulated in some historical simulations, though with large uncertainties due to internal variability (Figure A.6g). Grouping models by OHU_{wSA} trends, I find that subsets with more positive OHU_{wSA} trends show weaker SO-SEP relationships (smaller R^2) across models (Figure A.6h). This is consistent with the negative dependence of R^2 on OHU_{wSA} $sdv.$ discussed in the main text, as well as the negative dependence of the SO-SEP relationship R^2 using absolute SST trends on climatological OHU_{wSA} discussed above. This negative dependence is not affected by internal variability; it remains robust when changing the subset size and when including or excluding global-mean SST trends. However, the observational range of the OHU_{wSA} trend is too large to be capable of constraining the SO-SEP relationship strength.

A.2 Figures and Table

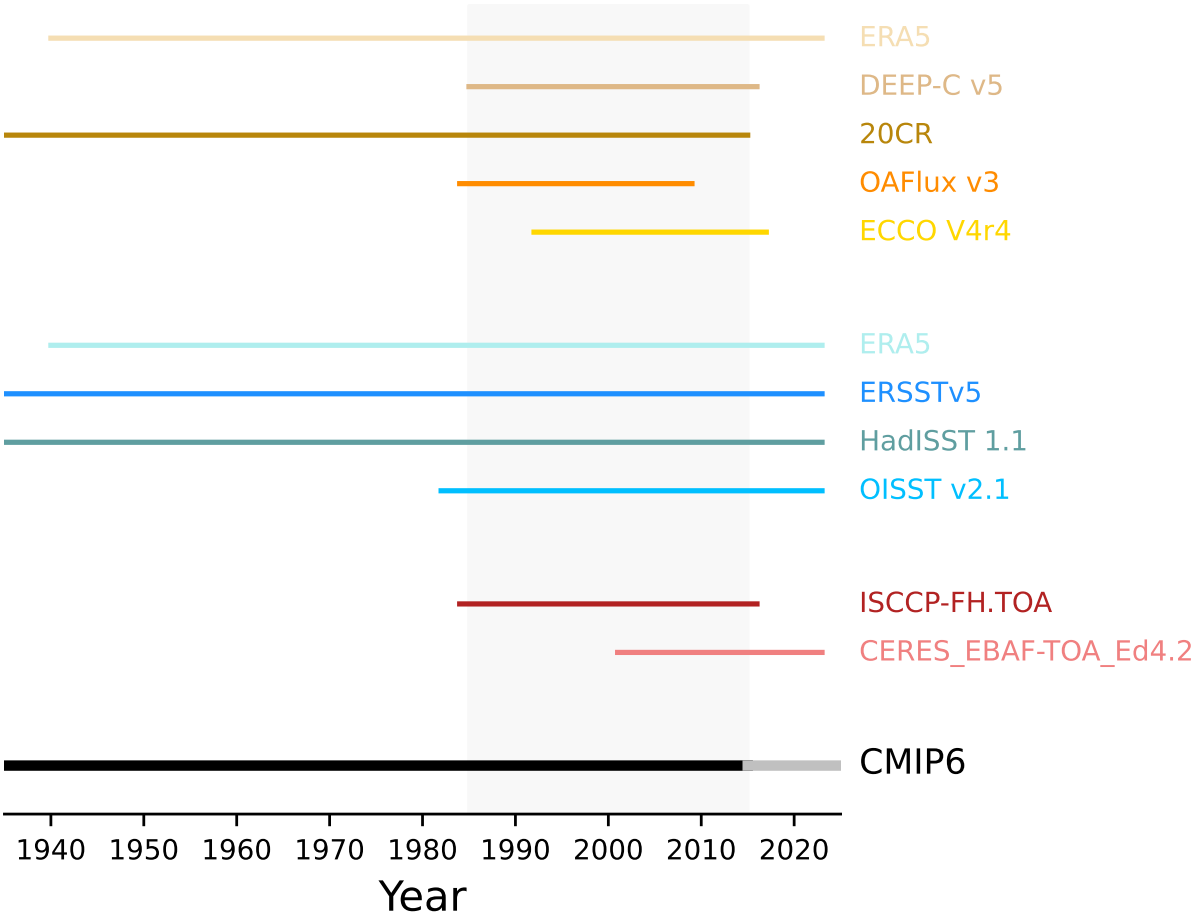

Figure A.1: Temporal coverage of different observational products used in this study. Yellow-toned lines represent ocean heat uptake reanalyses, blue-toned lines represent SST reanalyses, and red-toned lines represent top-of-atmosphere radiation observations. Thick black and grey lines represent historical simulations and SSP scenario simulations from CMIP6 models, respectively. The timeline focuses on the period 1940-2020 for illustrative purposes, while some observational products and all CMIP6 models extend beyond this time range.

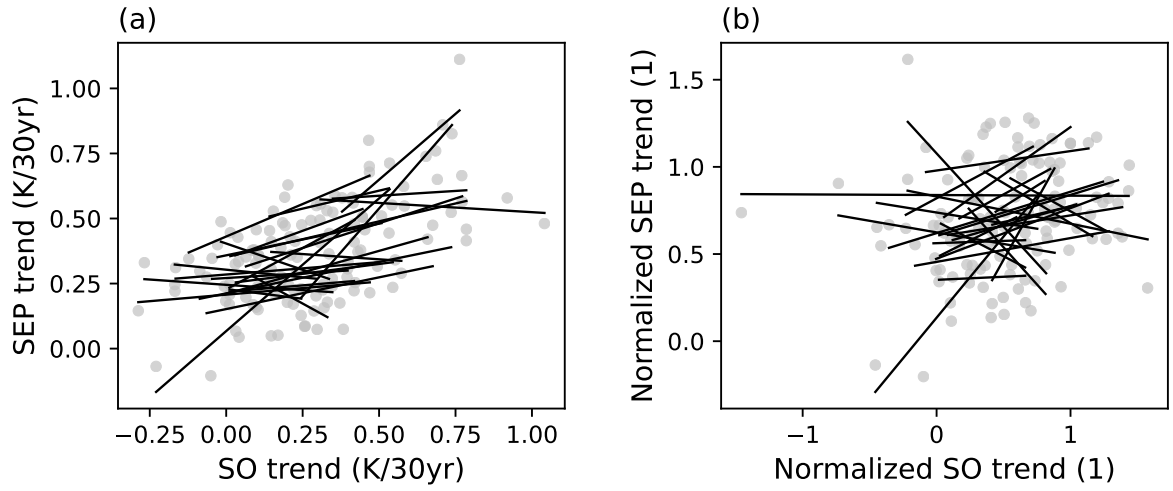

Figure A.2: (a) Relationship between SO and SEP SST trends across five ensemble members in 26 CMIP6 models. Grey dots are the five individual ensemble members; in total, there are 5x26 dots. Solid lines represent least-squares fits in each model across ensembles. (b) As in (a), but for the relationship between normalized SO and SEP SST trends.

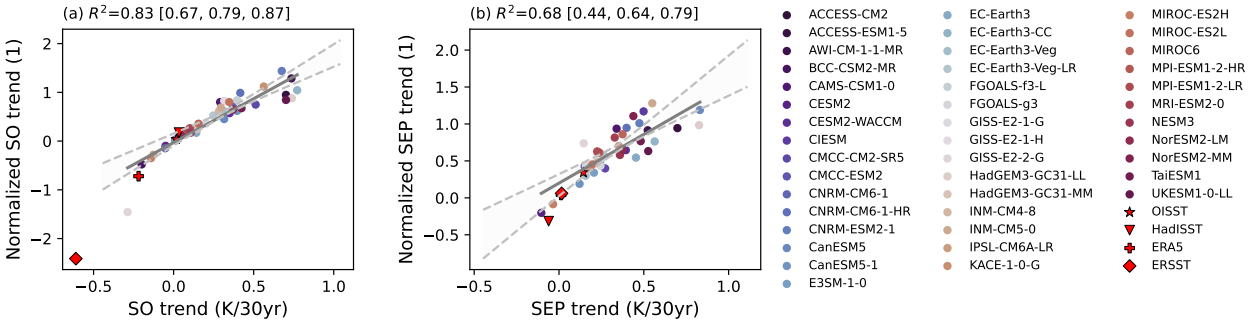

Figure A.3: Relationship between absolute SST trend and normalized SST trend across models in (a) SO and (b) SEP. The solid line represents the least-squares fit. Dashed lines and the shaded area denote 5%-95% confidence intervals from bootstrapping different ensemble members. The R^2 is displayed in the title. Values in brackets represent the 5th, 50th, and 95th percentiles of R^2 from bootstrapping.

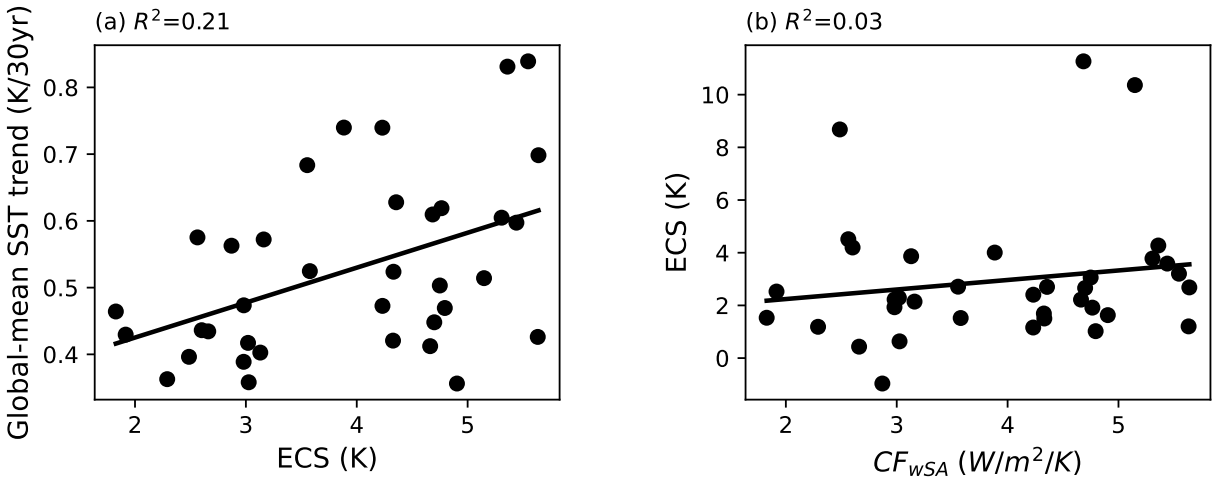

Figure A.4: Relationship between (a) ECS and global-mean SST trends and (b) ECS and CF_{wSA} across 42 CMIP6 models using the first ensemble member. The solid line represents the least-squares fit. The R^2 values are displayed in the title.

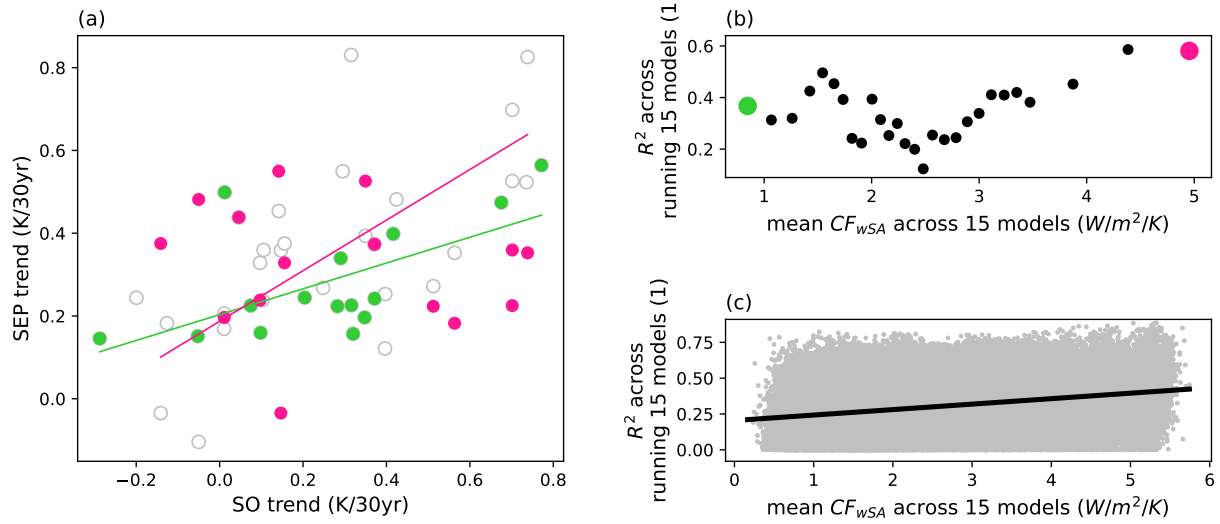

Figure A.5: Illustrative examples for deriving values in Figure 3 of the main text. (a) Same as Figure 1c, with green and pink dots representing subsets of 15 models with the lowest (0.85 $W/m^2/K$) and highest (4.96 $W/m^2/K$) model-mean CF_{wSA}, respectively. The green and pink lines are the least-squares fits to these two subsets of models. (b) Consecutive overlapping subsets of 15 models are selected from a total of 42 models ranked by their CF_{wSA} values. The first green dot represents the subset with the lowest model-mean CF_{wSA} (corresponding to green dots in (a)) and an R^2 value of 0.37 for the cross-model SO–SEP SST trend relationship. Black dots indicate model-mean CF_{wSA} and corresponding R^2 values across running subsets. And the pink dot marks the highest model-mean CF_{wSA} and its associated R^2 in the SO-SEP relationship. (c) Extends (b) to 5000 bootstrap iterations using different ensemble members. The black line represents the least-squares fit to all scatter points, matching the black line in Figure 3a of the main text.

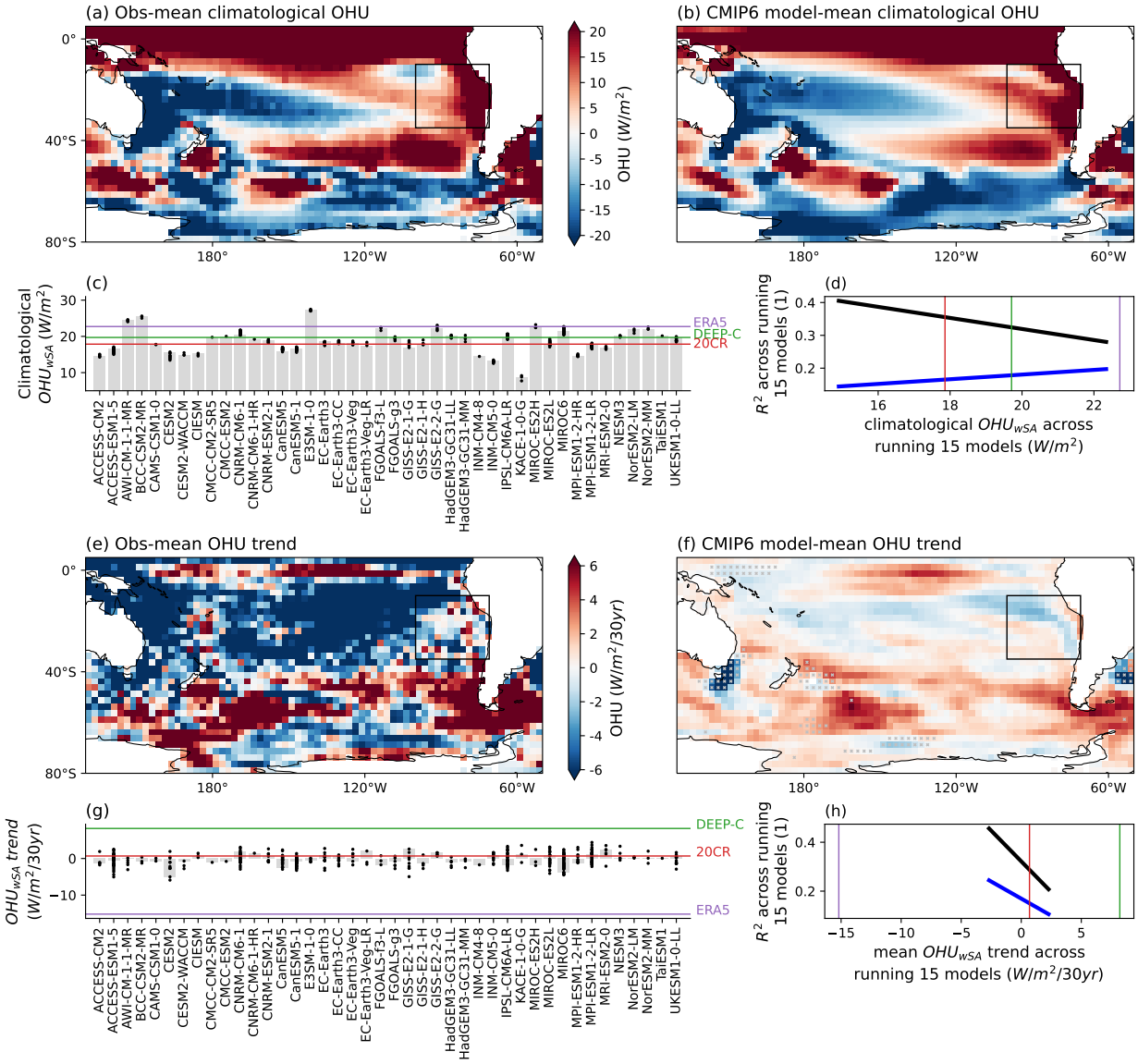

Figure A.6: Overview of climatological OHU and OHU trend in South Pacific. (a) Observed climatological OHU map over 1985-2014. (b) Simulated climatological OHU map. (c) Comparison of observed climatological OHU_{wSA} (solid colored lines) with those in the first ensemble member from CMIP6 models (grey bars). Black dots on each bar represent climatological OHU_{wSA} from each ensemble. (d) Constraints of SO-SEP relationship strength using climatological OHU_{wSA}. The black line represents the linear relationship between R^2 values of SO-SEP SST trend relationship (as in Figure 1c of the main text) and climatological OHU_{wSA}. The blue lines represent the linear relationship between R^2 values of normalized SO-SEP relationship (as in Figure 1c of the main text) and climatological OHU_{wSA}. The vertical lines represent observations the same as in (c). (e-h) Same as (a-d) but for OHU_{wSA} trends over 1985-2014.

Table A.1: CMIP6 historical simulations covering the period 1985-2014, and the number of ensemble members used in this study (N). Models with asterisks are the ones do not have ECS values from the exact ensemble members as in Zelinka et al. (2020)

Model	N	Reference
ACCESS-CM2	5	Dix et al. (2019)
ACCESS-ESM1-5	40	Dix et al. (2019)
AWI-CM-1-1-MR	5	Semmler et al. (2018)
BCC-CSM2-MR	3	Xin et al. (2018)
CAMS-CSM1-0	2	Rong (2019)
CESM2	11	Danabasoglu (2019b)
CESM2-WACCM	3	Danabasoglu (2019d)
CIESM	3	Huang (2019)
CMCC-CM2-SR5	1	Lovato and Peano (2020)
CMCC-ESM2	1	Lovato et al. (2021)
CNRM-CM6-1	28	Voldoire (2018)
CNRM-CM6-1-HR	1	Voldoire (2019)
CNRM-ESM2-1	10	Seferian (2018)
CanESM5	25	Swart et al. (2019a)
CanESM5-1*	47	Swart et al. (2019b)
E3SM-1-0	5	Bader et al. (2019)
EC-Earth3*	12	EC-Earth (2019a)
EC-Earth3-CC	10	EC-Earth (2020a)
EC-Earth3-Veg	7	EC-Earth (2019b)
EC-Earth3-Veg-LR	3	EC-Earth (2020c)
FGOALS-f3-L	3	YU (2018)
FGOALS-g3	6	Li (2019)
GISS-E2-1-G*	10	NASA/GISS (2018a)
GISS-E2-1-H*	5	NASA/GISS (2018b)
GISS-E2-2-G*	5	NASA/GISS (2019a)
HadGEM3-GC31-LL	5	Ridley et al. (2018)
HadGEM3-GC31-MM	4	Ridley et al. (2019)
INM-CM4-8	1	Volodin et al. (2019a)
INM-CM5-0	10	Volodin et al. (2019b)
IPSL-CM6A-LR	33	Boucher et al. (2018)
KACE-1-0-G	3	Byun et al. (2019)
MIROC-ES2H*	3	Watanabe et al. (2021b)
MIROC-ES2L	30	Hajima et al. (2019b)
MIROC6	50	Tatebe and Watanabe (2018)
MPI-ESM1-2-HR	10	Jungclaus et al. (2019)
MPI-ESM1-2-LR	37	Wieners et al. (2019)
MRI-ESM2-0	6	Yukimoto et al. (2019)
NESM3	5	Cao and Wang (2019)
NorESM2-LM	3	Seland et al. (2019)
NorESM2-MM	3	Bentsen et al. (2019)
TaiESM1	1	Lee and Liang (2020)
UKESM1-0-LL	14	Tang et al. (2019)